ISSN 2074-272X

науково-практичний журнал

2021/1

Електротехніка і Електромеханіка

Electrical Engineering & Electromechanics

Електричні машини та апарати
Електротехнічні комплекси та системи
Силова електроніка
Інженерна електрофізика.
Техніка сильних електричних та магнітних полів
Електроізоляційна та кабельна техніка
Електричні станції, мережі і системи

Журнал включено до найвищої категорії «А»
Переліку фахових видань України

З 2015 р. журнал індексується у міжнародній наукометричній базі Web of Science
Core Collection: Emerging Sources
Citation Index

«ELECTRICAL ENGINEERING & ELECTROMECHANICS»

Scientific Journal was founded in 2002

Founders are:

National Technical University «Kharkiv Polytechnic Institute» (Kharkiv, Ukraine)

State Institution «Institute of Technical Problems of Magnetism of the NAS of Ukraine» (Kharkiv, Ukraine)

Journal «Electrical Engineering & Electromechanics» from no. 1 2015 is indexing in Web of Science Core Collection : Emerging Sources Citation Index (ESCI).

Also included in DOAJ (Directory of Open Access Journals), in EBSCO's database, in ProQuest's databases – Advanced Technologies & Aerospace Database and Materials Science & Engineering Database, in Gale/Cengage Learning databases.

Editorial office address:

National Technical University «Kharkiv Polytechnic Institute», Kyrpychova Str., 2, Kharkiv, 61002, Ukraine

phones: +380 57 7076281, +380 67 3594696, **e-mail:** a.m.grechko@gmail.com (**Grechko O.M.)**

ISSN (print) 2074-272X

ISSN (online) 2309-3404

Printed 25 February 2021. Format 60 × 90 ⅛. Paper – offset. Laser printing. Edition 200 copies.

Printed by Printing house «Madrid Ltd» (18, Gudanova Str., Kharkiv, 61024, Ukraine)

ELECTRICAL ENGINEERING & ELECTROMECHANICS
Scientific journal

no. 1, 2021

TABLE OF CONTENTS

Electrical Machines and Apparatus

Electrotechnical Complexes and Systems

Power Electronics

Engineering Electrophysics. High Electric and Magnetic Fields Engineering

Electrical Insulation and Cable Engineering

Power Stations, Grids and Systems

UDC 621.313.282 **doi: 10.20998/2074-272X.2021.1.01**

V.F. Bolyukh, Yu.V. Kashansky, I.S. Schukin

FEATURES OF EXCITATION OF A LINEAR ELECTROMECHANICAL CONVERTER OF INDUCTION TYPE FROM AN AC SOURCE

Purpose. *The purpose of the article is to establish the basic laws of operation of induction-type linear electromechanical converter (LEMC) during operation in high-speed and shock-power modes and excitation from an AC source of increased frequency.* ***Methodology.*** *With the help of a mathematical model, the regularities of the course of processes in a LEMC, excited from an AC source, were established when working with shock-power and high-speed modes. The solutions of the equations of the mathematical model, which describe interrelated electrical, magnetic, mechanical and thermal processes, are presented in a recurrent form.* ***Results.*** *It was found that when the LEMC operates in the shock-power mode, the maximum value of the current in the inductor winding occurs in the first half-period, and in the inhibited armature winding in the second half-period. The electrodynamic force changes at twice the frequency, taking on both positive and negative values. Since the positive values exceed the negative ones, the magnitude of the impulse of the electrodynamic force increases with each period of the force. Depending on the initial voltage phase, the relative change in the magnitude of the force impulse is 1.5 %. It was found that when the LEMC operates in high-speed mode, the current in the inductor winding in the first half-period has the greatest value, but after several periods it takes on a steady state. The temperature rise of the inductor winding increases with the time of connection to the AC source, and the temperature rise of the armature winding has the nature of saturation. The electrodynamic force has an oscillatory character with strong damping and a significant predominance of the positive component. Depending on the initial phase of the voltage, the relative change in the maximum speed of the armature winding is 2.5 %.* ***Originality.*** *For the first time, a mathematical model of the LEMC, excited from an AC source, was developed, the solutions of the equations of which describe the interrelated electrical, magnetic, mechanical and thermal processes. For the first time, the regularities of the course of processes in LEMC were established when working with shock-power and high-speed modes.* ***Practical value.*** *The characteristics of LEMC are obtained, which determine the efficiency of work in shock-power and high-speed modes. It is shown that the initial voltage phase has no significant effect on the power, high-speed thermal performance of the converter excited from an alternating current source.* References 16, figures 5.

Key words: **linear electromechanical induction-type converter, mathematical model, high-speed and shock-power operation mode, alternating current source, maximum speed, electrodynamic force impulse.**

Розроблена ланцюгова математична модель лінійного електромеханічного перетворювача індукційного типу при збудженні від джерела змінного струму, в якій рішення рівнянь, що описують взаємопов'язані електричні, магнітні, механічні та теплові процеси, які представлені в рекурентному вигляді. Встановлено, що при роботі перетворювача в ударно-силовому режимі електродинамічна сила змінюється з подвійною частотою, приймаючи як позитивні, так і негативні значення. Позитивні значення сили перевищують негативні і величина імпульсу електродинамічної сили з кожним періодом підвищується. В залежності від початкової фази напруги відносна зміна величини імпульсу сили складає 1,5 %. При роботі перетворювача в швидкісному режимі максимальний струм в обмотці індуктора в перший півперіод має найбільше значення, але через декілька періодів приймає постійне значення. В залежності від початкової фази напруги відносна зміна максимальної швидкості обмотки якоря складає 2,5 %. Бібл. 16, рис. 5.

Ключові слова: **лінійний електромеханічний перетворювач індукційного типу, математична модель, швидкісний і ударно-силовий режим роботи, джерело змінного струму, максимальна швидкість, імпульс електродинамічної сили.**

Разработана цепная математическая модель линейного электромеханического преобразователя индукционного типа при возбуждении от источника переменного тока, в которой решения уравнений, описывающие взаимосвязанные электрические, магнитные, механические и тепловые процессы, представлены в рекуррентном виде. Установлено, что при работе преобразователя в ударно-силовом режиме электродинамическая сила изменяется с удвоенной частотой, принимая как положительные, так и отрицательные значения. Положительные значения силы превышают отрицательные и величина импульса электродинамической силы с каждым периодом увеличивается. В зависимости от начальной фазы напряжения относительное изменение величины импульса силы составляет 1,5 %. При работе преобразователя в скоростном режиме максимальный ток в обмотке индуктора в первый полупериод имеет наибольшее значение, но через несколько периодов принимает постоянное значение. В зависимости от начальной фазы напряжения относительное изменение максимальной скорости обмотки якоря составляет 2,5 %. Библ. 16, рис. 5.

Ключевые слова: **линейный электромеханический преобразователь индукционного типа, математическая модель, скоростной и ударно-силовой режим работы, источник переменного тока, максимальная скорость, импульс электродинамической силы.**

Introduction. Linear electromechanical converters (LEMCs) of induction type are used to accelerate the actuation element to high speed in a short active section and to create powerful force pulses on the object of influence with a slight movement of the specified element [1-4]. Such converters operate in high-speed (accelerating) and shock-power modes. They are used as actuating elements of electromechanical accelerators and shock-power devices [5-7].

In LEMC of induction type, a movable armature, made in the form of a single- or multi-turn short-circuited winding, inductively interacts with the stationary winding of the inductor. In a converter of coaxial configuration, the windings are made in the form of discs. The armature winding is installed and moves axially relative to the inductor winding. When the inductor winding is excited from the power source, the current flowing in it through

the magnetic field induces a current in the armature winding. The resulting electrodynamic forces between the windings are transmitted to the actuation by means of the movable armature winding.

The most common excitation of LEMC is from a high-voltage capacitive energy storage [2, 8]. However, this requires special high-voltage equipment and appropriate winding design. In addition, such excitation occurs over a relatively short period of time, which can limit a number of performance and technical applications of the converter.

At one time, other sources of excitation of LEMC of the induction type were considered, for example, inductive and of alternating current of increased frequency [9]. In [10], an AC source was investigated for an electromechanical accelerator of a cylindrical configuration, in which the armature winding moves coaxially inside the inductor winding. The following options were considered:

1) excitation from a source of increased frequency;

2) excitation from a source, the frequency of which increases as the armature winding accelerates;

3) winding of the inductor winding with an increasing step, which is excited from a source of constant frequency.

Option No. 2 requires a special generator. Option No. 3 is appropriate only for an accelerator, in which the armature winding moves inside the inductor winding. Option No. 1 was developed in [11], where an electromechanical accelerator was described, in which the armature winding was accelerated inside a row of axially installed sections of the inductor winding. The sections of the inductor winding, as the armature winding moved, were sequentially connected to the sections of the AC source, in each of which the frequency of the alternating current was constant, but increased in relation to the frequency of the previous section. Note that such an excitation system is complex and requires a complex switching system.

All studies of excitation sources concerned LEMC operating in high-speed mode, in which the time of effective interaction of the accelerated armature winding with the inductor winding is insignificant. But when operating in the shock-power mode, the indicated interaction time can be significant, being limited by other factors, for example, thermal one.

The goal of the paper is the establishment of the basic laws of operation of induction-type LEMC when operating in high-speed and shock-power modes and excitation from an AC source of increased frequency.

LEMC mathematical model. Consider a mathematical model of an induction-type LEMC in a high-speed mode, in which the magnetic coupling between the windings changes during the excitation of the inductor winding. In this model, we use the lumped parameters of the fixed inductor winding and the accelerated armature winding [12]. To take into account the interrelated electrical, magnetic, mechanical and thermal processes, as well as a number of nonlinear dependences, for example, resistance on temperature, the solution of equations describing these processes will be presented in a recurrent form [9, 13].

To calculate the indicators and time characteristics of LEMC, we use a cyclic algorithm. For this, the workflow is divided into a number of numerically small time intervals $\Delta t = t_{k+1} - t_k$, within which all quantities are considered unchanged. On the k-th cycle, using the parameters calculated at the time t_k as initial values, the parameters are calculated at the time t_{k+1}.

To determine the currents over the time interval Δt, we use linear equations with unchanged parameter values. We choose a small value of the calculated step Δt so that it does not have a significant effect on the calculation results on a computer, while ensuring the required accuracy.

Initial conditions of the mathematical model are: $T_n(0) = T_0$ is the temperature of the n-th winding; $i_n(0) = 0$ is the current of the n-th winding; $h_z(0) = h_{z0}$ is the distance between the windings; $u(0) = U_m \sin\psi_u$ is the voltage of the AC source; $v_z(0) = 0$ is the speed of the armature winding along the z axis.

Since the inductor and the armature are made in the form of multi-turn tightly wound windings, it is advisable for them to use the concepts of inductances and mutual inductance. The change in the spatial position of the armature winding is taken into account by the change in flux linkage Ψ between the windings [14]:

$$\frac{d\Psi_n}{dt} = M(z)\frac{di_n}{dt} + v_z(t)\cdot i_n \frac{dM}{dz}, \qquad (1)$$

where n = 1, 2 are the indices of the inductor and armature windings, respectively; $M(z)$ is the mutual inductance between the windings; v_z is the speed of movement of the armature winding along the z axis; i_n is the current of the n-th winding.

In this case, the electrical processes in the LEMC windings can be described by the system of equations:

$$R_1(T_1)i_1 + L_1\frac{di_1}{dt} + M_{12}(z)\frac{di_2}{dt} + i_2 v_z(t)\frac{dM_{12}}{dz} = u(t), \quad (2)$$

$$R_2(T_2)i_2 + L_2\frac{di_2}{dt} + M_{21}(z)\frac{di_1}{dt} + i_1 v_z(t)\frac{dM_{21}}{dz} = 0, \quad (3)$$

where $u(t) = U_m \sin(\omega t + \psi_u)$ is the power supply voltage; R_n, L_n, T_n are the active resistance, inductance, temperature and current of the n-th winding, respectively.

Let's introduce the notation:

$$R_1 = R_1(T_1);\ R_2 = R_2(T_2);$$

$$M = M_{12}(z) = M_{21}(z);\ v_z = v_z(t);\ u = u(t).$$

We will find solutions for currents in the form:

$$i_1 = \frac{u}{R_1} - \beta\frac{i_2}{R_1} + A_{11}\exp(\alpha_1 t) + A_{12}\exp(\alpha_2 t), \quad (4)$$

$$i_2 = -\beta\frac{i_1}{R_1} + A_{21}\exp(\alpha_1 t) + A_{22}\exp(\alpha_2 t), \qquad (5)$$

where $\alpha_{1,2} = -0.5\varsigma\chi^{-1} \pm \left\{0.25\varsigma^2\chi^{-2} - \left[R_1R_2 - \beta^2\right]\chi^{-1}\right\}$ are the roots of the characteristic equation for the free component described by the differential equation

$$\chi\frac{d^2 i_1}{dt^2} + \varsigma\frac{di_1}{dt} + \left(R_1R_2 - \beta^2\right)i_1 = 0, \qquad (6)$$

$$\beta = v_z\frac{dM}{dz};\ \varsigma = L_1R_2 + L_2R_1 - 2\beta M;\ \chi = L_1L_2\left(1 - K_M^2\right);$$

$K_M = M\left(L_1 L_2\right)^{-0.5}$ is the magnetic coupling coefficient between windings; $A_{11}, A_{12}, A_{21}, A_{22}$ are the arbitrary constants determined at time t_k for the free component of currents equal to

$$A_{1l} = \frac{\alpha_m\left[i_2(t_k)\beta R_1^{-1} - u(t_k)R_1^{-1} + i_1(t_k)\right] - \Xi}{(\alpha_m - \alpha_l)\exp(\alpha_l t_k)}; \quad (7)$$

$$A_{2l} = \frac{\alpha_m\left[i_2(t_k) + i_1(t_k)\beta R_2^{-1}\right] - \Omega}{(\alpha_m - \alpha_l)\exp(\alpha_l t_k)}, \quad (8)$$

where l = 1, 2; m = 3 – l;

$$\Xi = \frac{1}{L_1\left(1-K_M^2\right)}\left\{u(t_k) + i_1(t_k)\left(\beta\frac{M}{L_2} - R_1\right) + i_2(t_k)\left(\frac{MR_2}{L_2} - \beta\right)\right\};$$

$$\Omega = \frac{1}{L_2\left(1-K_M^2\right)}\left\{i_2(t_k)\left(\beta\frac{M}{L_1} - R_2\right) - u(t_k)\frac{M}{L_1} + i_1(t_k)\left(\frac{MR_1}{L_1} - \beta\right)\right\}.$$

In the final form, the currents in the LEMC windings are described by the expressions:

$$i_1(t_{k+1}) = -\frac{i_2(t_k)v_z(t_k)}{R_1}\frac{dM}{dz} + \left(u(t_k) - R_1 i_1(t_k) - i_2(t_k)v_z(t_k)\times\right.$$
$$\left.\times\frac{dM}{dz}\right)\frac{\alpha_1\exp(\alpha_2\Delta t) - \alpha_2\exp(\alpha_1\Delta t)}{R_1(\alpha_2 - \alpha_1)} + \frac{u(t_k)}{R_1} +$$
$$+\frac{\exp(\alpha_2\Delta t) - \exp(\alpha_1\Delta t)}{L_1 L_2(\alpha_2 - \alpha_1)\left(1-K_M^2\right)}\left\{u(t_k)L_2 + \left[v_z(t_k)M\frac{dM}{dz} - R_1 L_2\right]\times\right. \quad (9)$$
$$\left.\times i_1(t_k) + \left[R_2 M - v_z(t_k)L_2\frac{dM}{dz}\right]i_2(t_k)\right\};$$

$$i_2(t_{k+1}) = -\frac{i_1(t_k)v_z(t_k)}{R_2}\frac{dM}{dz} + \left[i_2(t_k) + \frac{i_1(t_k)v_z(t_k)}{R_2}\frac{dM}{dz}\right]\times$$
$$\times\frac{\alpha_2\exp(\alpha_1\Delta t) - \alpha_1\exp(\alpha_2\Delta t)}{\alpha_2 - \alpha_1} + \frac{\exp(\alpha_2\Delta t) - \exp(\alpha_1\Delta t)}{L_1 L_2(\alpha_2 - \alpha_1)\left(1-K_M^2\right)}\times \quad (10)$$
$$\times\left\{i_1(t_k)\left[R_1 M - v_z(t_k)L_1\frac{dM}{dz}\right] - u(t_k)M + i_2(t_k)\times\right.$$
$$\left.\times\left[v_z(t_k)M\frac{dM}{dz} - R_2 L_1\right]\right\},$$

where $u(t_k) = U_m\sin(\omega t_k + \psi_u)$; $\Delta t = t_{k+1} - t_k$.

The value of the displacement of the armature winding together with the actuation element relative to the stationary inductor winding can be represented as a recurrent relation [15]:

$$h_z(t_{k+1}) = h_z(t_k) + v_z(t_k)\Delta t + \vartheta\cdot\Delta t^2/\left(m_a + m_2\right), \quad (11)$$

where $v_z(t_{k+1}) = v_z(t_k) + \vartheta\cdot\Delta t/\left(m_a + m_2\right)$ is the speed of the armature winding together with the actuation element;

$$\vartheta = f_z(z,t) - K_T v_z(t_k) - 0{,}125\pi\gamma_a\beta_a D_{e2}^2 v_z^2(t_k);$$

$f_z(z,t) = i_1(t_k)i_2(t_k)\frac{dM}{dz}(z)$ is the instantaneous value of the axial electrodynamic force between the windings; m_2, m_a is the mass of the armature winding and the actuation element, respectively; h_z is the value of displacement of the armature winding; K_T is the coefficient of dynamic friction; γ_a is the density of the medium of moving; β_a is the coefficient of aerodynamic resistance; D_{e2} is the outer diameter of the actuation element.

When the LEMC operates in the shock-power mode, there is a thermal contact between the windings through an insulating pad. In this case, the temperature of the n-th winding can be described by the recurrence relation [16]:

$$T_n(t_{k+1}) = T_n(t_k)\xi + (1-\xi)\left[\pi^{-1}i^2(t_k)R_n(T_n)\left(D_{en}^2 - D_{in}^2\right)^{-1} + \right.$$
$$\left. + 0{,}25\pi T_0 D_{en}H_n\alpha_{Tn} + T_m(t_k)\lambda_a(T)d_a^{-1}\right]\times \quad (12)$$
$$\times\left\{0{,}25\pi\alpha_{Tn}D_{en}H_n + \lambda_a(T)d_a^{-1}\right\}^{-1},$$

where $\xi = \exp\left\{-\frac{\Delta t}{c_n(T_n)\gamma_n}\left(0{,}25D_{en}\alpha_{Tn} + \frac{\lambda_a(T)}{d_a H_n}\right)\right\}$;

$\lambda_a(T)$, d_a are the thermal conductivity and the thickness of the pad, respectively; D_{en}, D_{in} are the outer and inner diameters of the n-th winding, respectively; α_{Tn}, c_n are the heat transfer coefficient and heat capacity of the n-th winding, respectively.

When the LEMC operates in high-speed mode, the temperature of the n-th winding can be described by the recurrent relation:

$$T_n(t_{k+1}) = T_n(t_k)\chi + (1-\chi)\left[T_0 + 4\pi^{-2}i^2(t_k)\times\right.$$
$$\left.\times R_n(T_n)\alpha_{Tn}^{-1}D_{en}^{-1}H_n^{-1}\left(D_{en}^2 - D_{in}^2\right)^{-1}\right], \quad (13)$$

where $\chi = \exp\left\{-0{,}25\Delta t D_{en}\alpha_{Tn}c_n^{-1}(T_n)\gamma_n^{-1}\right\}$.

When implementing equations (9) – (13) on a computer, a cyclic algorithm is used, in which at each numerically small calculation step, the values of the currents i_n, temperatures T_n, resistances $R_n(T_n)$ of the windings, the thermal conductivity of the pad $\lambda_a(T)$, the values of axial electrodynamic force $f_z(z, t)$, speed v_z and displacement h_z of the armature winding, mutual inductance $M(z)$ between the windings are sequentially calculated.

The main parameters of the LEMC. Consider a LEMC of the induction type, in which the inductor winding (n = 1) and the armature winding (n = 2) are made in the form of disk coils. The windings are tightly wound with 0.9 mm copper wire. The number of turns of the inductor winding N_1 = 450 and the armature winding N_2 = 180. The outer diameter of the windings is D_{en} = 100 mm, their inner diameter is D_{in} = 10 mm. The axial height of the inductor winding is H_1 = 10 mm, of the armature winding is H_2 = 4 mm. The windings are made in the form of massive disks by impregnation and subsequent hardening of epoxy resin. The windings are installed coaxially so that the initial distance between them is h_{z0} = 0.5 mm. The power supply is characterized by frequency of 100 Hz and an amplitude of U_m = 300 V.

Consider the duration of the connection time of the inductor winding to the source t = 50 ms. Let us estimate the efficiency of the LEMC when operating in a high-speed mode (mass of the actuation element m_a = 0.25 kg) by the value of the maximum speed V_m, and when operating in the shock-power mode by the value of the impulse of the electrodynamic force $P_z = \int f_z(z,t)dt$

(we assume that there is no displacement of the armature winding) with minimal rise of the winding temperatures $\theta_n = T_n - T_0$.

Consider the electrical and thermal characteristics of the LEMC when the inductor winding is connected to an AC source and there is no armature winding, assuming $\psi_u = 0$ (Fig. 1).

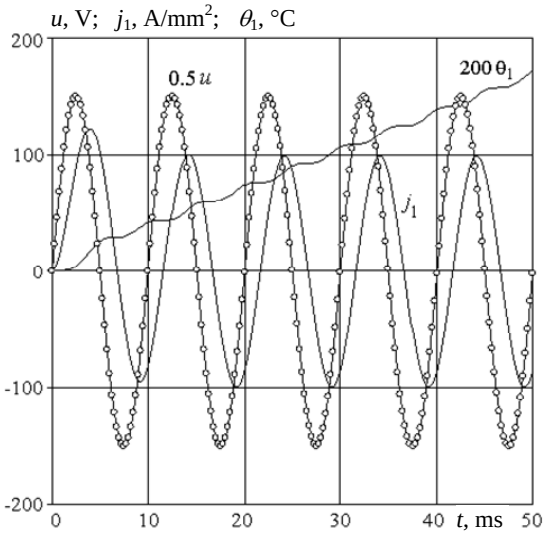

Fig. 1. Electrical and thermal characteristics of LEMC in the absence of the armature winding

The maximum current density in the inductor winding j_1 in the first half-period is 24 % higher than during subsequent steady-state oscillations. After each half-period of oscillations, an increase in the temperature rise θ_1 is observed. By the end of the considered time interval t = 50 ms, the temperature rise of the inductor winding is θ_1=0.86 °C.

Excitation of LEMC in shock-power mode. Let us consider the excitation of LEMC in the shock-power mode with the armature winding inhibited. Due to the induction effect of the inductor winding on the armature winding, current with density j_2 flows in the latter (Fig. 2,*a*).

The induced current in the armature winding has a phase shift with respect to the current in the inductor winding. Compared to operation in the absence of the armature winding, the maximum current density in the inductor winding j_1 increases by 6.7 %. In the first half-period, the current density in the armature winding takes the smallest negative value, but already in the second half-period, the largest positive value j_2 = 121.3 A/mm^2 appears. The rise of the temperature of the inductor winding θ_1 by the end of the considered time interval increases by 18.5 % compared to the operation of the LEMC in the absence of the armature winding. The temperature rise of the armature winding is practically the same as that of the inductor winding and is θ_2 = 1.03 °C.

Due to the phase shift between the winding currents, the electrodynamic force changes with a doubled frequency practically according to a sinusoidal law, taking both positive (repulsive) and negative (attractive) values (Fig. 2,*b*).

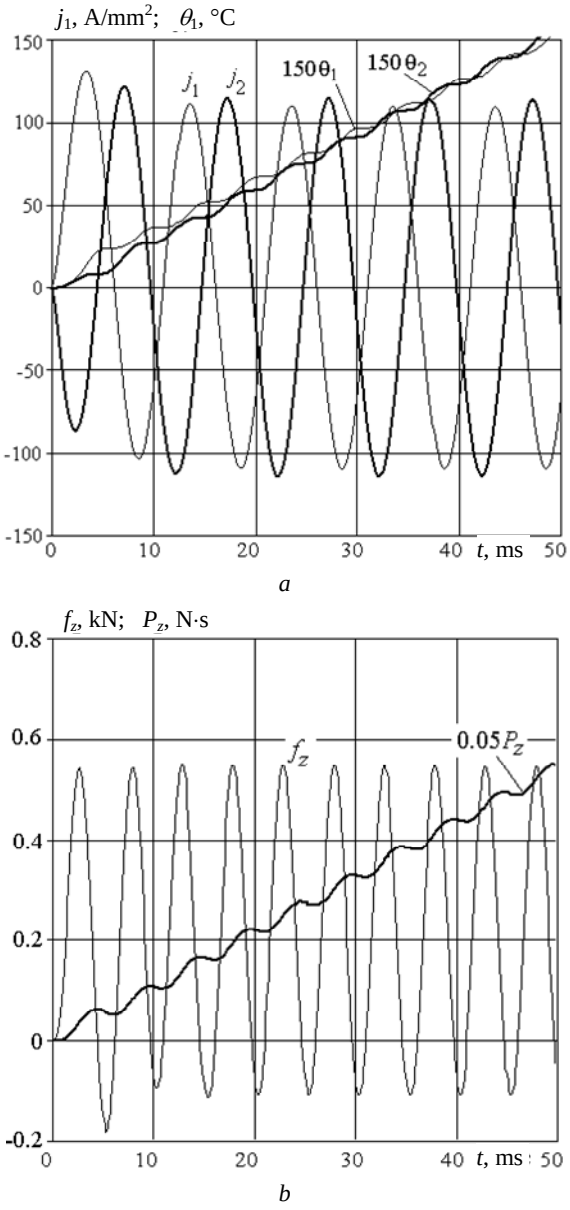

Fig. 2. Electrical, thermal (*a*) and power (*b*) characteristics of LEMC when excited in shock-force mode

Positive force values (currents in the windings have opposite directions) are several times higher than negative values (currents have the same directions). The maximum value of the force of the first positive oscillation is f_z = 0.542 kN, slightly increasing in subsequent half periods. The value of the first negative oscillation is maximum and is 0.182 kN, subsequently decreasing by 67 %. Since positive oscillations of the force prevail in magnitude over negative ones, the value of the impulse of the electrodynamic force P_z increases with each period of the force f_z, reaching the value P_z = 10.98 N·s by the end of the considered time interval. At positive values of the force f_z, the value of the impulse of the force P_z increases, and at negative values of the force, the value of P_z has characteristic decreases.

The initial phase of the voltage at the moment of connecting the LEMC to the AC source can be in the range $\psi_u \in (0; 180°)$. The influence of the initial phase of the voltage on the values of the temperature rises of the

windings and the impulse of the electrodynamic force for the considered time interval t = 50 ms is shown in Fig. 3.

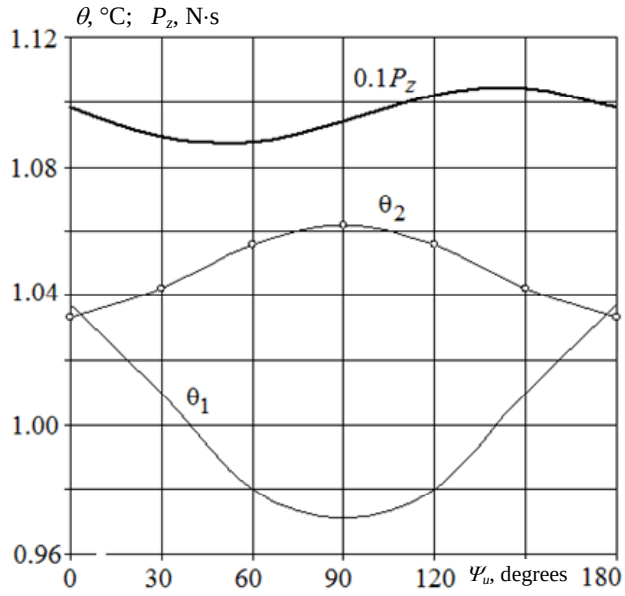

Fig. 3. Dependence of thermal and power indicators of LEMC in shock-power mode on the initial voltage phase of the AC source

To assess the influence of the initial phase of the source voltage, we use the relative change in the value of the indicator κ:

$$\Delta\kappa = 2\frac{\kappa_{\max} - \kappa_{\min}}{\kappa_{\max} + \kappa_{\min}},$$

where $\kappa_{\max}$, $\kappa_{\min}$ are the maximum and minimum values of the indicator κ, respectively.

The minimum value of the value of the impulse of the force P_z for the considered converter occurs approximately at ψ_u=50°, and the maximum value – after 90°. The relative change in the value of the force impulse is insignificant and amounts to ΔP_z = 1.5 %.

The temperature rise of the windings has an extremum at the center of the considered interval ψ_u. The temperature rise of the inductor winding at ψ_u=90° is minimal, and of the armature winding is maximal. The relative changes in thermal indicators are $\Delta\theta_1$=6.6 % and $\Delta\theta_2$=2.8 %.

Excitation of LEMC in high-speed mode. The high-speed mode of LEMC is characterized by the fact that, under the action of an electrodynamic force, the armature winding, together with the actuation element, moves relative to the inductor winding, causing a weakening of the magnetic coupling between the windings (Fig. 4). In this mode of LEMC operation, the current in the inductor winding has the following features (Fig. 4,*a*). In the first half-period, the maximum current density in the inductor winding has the highest value j_1 = 125.2 A/mm^2, but after several periods it reaches a steady-state value j_1 = 99 A/mm^2 (as when operating with the missing armature winding). The induced current in the armature winding has an oscillatory-damping character with the highest maximum value in the second positive half-cycle.

The indicated character of the flow of currents leads to a significant change in the temperature rise in relation to the shock-force mode of operation of the LEMC. The rise of the temperature of the inductor winding by the end of the considered time interval is θ_1=0.88 °C and increases from the moment of connection to the AC source. The rise of the temperature of the armature winding has the nature of saturation, reaching a significantly lower value θ_2=0.16 °C during the considered time.

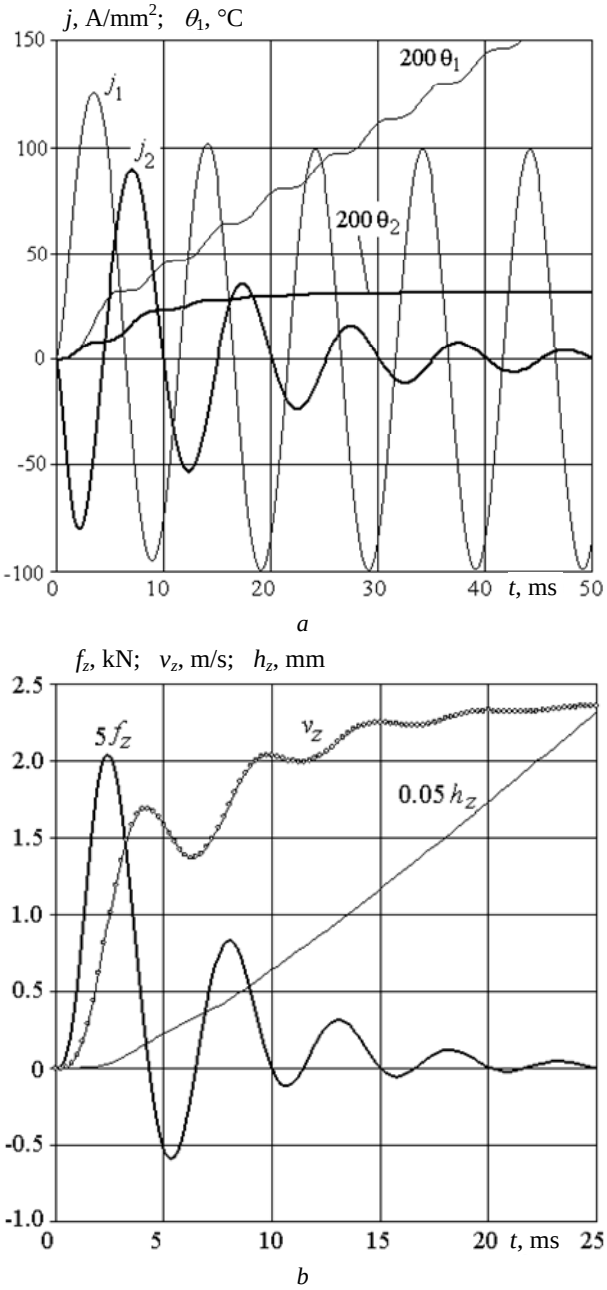

Fig. 4. Electrical, thermal (*a*) and mechanical (*b*) characteristics of LEMC when excited in high-speed mode

The mechanical characteristics of LEMC of induction type in high-speed operation mode have the following features (Fig. 4,*b*). The electrodynamic force f_z takes on an oscillatory character with fast decay and a significant predominance of the positive component. The largest value of the force f_z = 0.4 kN is less than when the LEMC operates in the shock-power mode. But the value of the force impulse is even more significantly less,

having P_z = 1.25 N·s by the end of the considered time interval.

The nature of the change in the speed of the armature winding is influenced by both positive (accelerating) and negative (braking) components of the electrodynamic force. By the end of the considered excitation interval, the speed reaches its maximum value V_m = 2.36 m/s.

The influence of the initial voltage phase on the LEMC indicators is shown in Fig. 5. Compared with the shock-power mode of operation of the LEMC in the range $\psi_u \in (0; 180°)$, there is no symmetry of the temperature rise of the windings. The relative changes in thermal indicators are $\Delta\theta_1$ = 8 %, $\Delta\theta_2$ = 1.9 %. The maximum armature winding speed takes place at approximately ψ_u = 90°. It slightly depends on the initial phase of the voltage (the relative change is ΔV_m = 2.5 %).

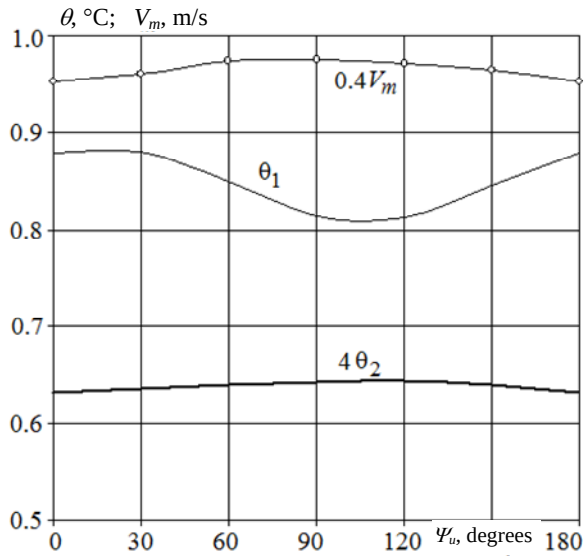

Fig. 5. Dependence of thermal and mechanical parameters of LEMC in high-speed mode on the initial voltage phase of the AC source

Based on the research carried out, the following conclusion can be drawn. Excitation of LEMC of induction type from an AC source makes it possible to implement new technical applications. For example, when the LEMC operates in the shock-power mode, it is possible to multiply the time of the force action on the actuating element in comparison with the excitation from the capacitive energy storage. Such a long-term force effect is necessary in presses with a large range of impact energies, in drives of cold rolling mills, in vibrating mixers, metering devices, pumps, in test complexes for checking critical equipment for power loads, in magnetic-pulse devices for pressing ceramic powders, in devices for electrodynamic treatment of welded joints, etc. [9].

Conclusions.

1. A chain mathematical model of the LEMC with excitation from an AC source has been developed, in which the solutions of equations describing interrelated electrical, magnetic, mechanical and thermal processes are presented in a recurrent form.

2. It is found that when the LEMC operates in the shock-power mode, the maximum value of the current in the inductor winding occurs in the first half-period, and in the inhibited armature winding in the second half-period. The electrodynamic force changes at twice the frequency, taking on both positive and negative values. Since the positive values exceed the negative ones, the value of the impulse of the electrodynamic force increases with each period of the force. Depending on the initial voltage phase, the relative change in the value of the force impulse is 1.5 %.

3. It is established that when the LEMC operates in high-speed mode, the current in the inductor winding in the first half-period has the greatest value, but after several periods it takes on a steady state. The temperature rise of the inductor winding increases with the time of connection to the AC source, and the temperature rise of the armature winding has the nature of saturation. The electrodynamic force has an oscillatory character with strong damping and a significant predominance of the positive component. Depending on the initial phase of the voltage, the relative change in the maximum speed of the armature winding is 2.5 %.

Conflict of interests. The authors declare no conflicts of interest.

REFERENCES

1. Guangcheng F., Wang Y., Xu Q., Xinyi N., Yan Z. Design and analysis of a novel three-coil reconnection electromagnetic launcher. *IEEE Transactions on Plasma Science*, 2019, vol. 47, no. 1, pp. 814-820. doi: https://doi.org/10.1109/tps.2018.2874287.

2. Go B.-S., Le D.-V., Song M.-G., Park M., Yu I.-K. Design and electromagnetic analysis of an induction-type coilgun system with a pulse power module. *IEEE Transactions on Plasma Science*, 2019, vol. 47, no. 1, pp. 971-976. doi: https://doi.org/10.1109/tps.2018.2874955.

3. Angquist L., Baudoin A., Norrga S., Nee S., Modeer T. Low-cost ultra-fast DC circuit-breaker: Power electronics integrated with mechanical switchgear. *2018 IEEE International Conference on Industrial Technology (ICIT)*, 2018, Lyon, pp. 1708-1713. doi: https://doi.org/10.1109/icit.2018.8352439.

4. Vilchis-Rodriguez D.S., Shuttleworth R., Barnes M. Modelling thomson coils with axis-symmetric problems: practical accuracy considerations. *IEEE Transactions on Energy Conversion*, 2017, vol. 32, no. 2, pp. 629-639. doi: https://doi.org/10.1109/tec.2017.2651979.

5. Kondratiuk M., Ambroziak L. Concept of the magnetic launcher for medium class unmanned aerial vehicles designed on the basis of numerical calculations. *Journal of Theoretical and Applied Mechanics*, 2016, vol. 54, iss. 1, pp. 163-177. doi: https://doi.org/10.15632/jtam-pl.54.1.163.

6. Liu X., Yu X., Ban R., Li Z. Analysis of the capacitor-aided meat grinder circuits for an inductive pulsed power supply. *IEEE Transactions on Plasma Science*, 2017, vol. 45, no. 7, pp. 1339-1346. doi: https://doi.org/10.1109/tps.2017.2705179.

7. Gorodzha K.A., Podoltsev O.D., Troshchinsky B.A. Electromagnetic processes in pulse electrodynamic emitter for exciting elastic oscillations in concrete structures. *Technical Electrodynamics*, 2019, no. 3, pp. 23-28. doi: https://doi.org/10.15407/techned2019.03.023.

8. Yadong Z., Ying W., Jiangjun R. Capacitor-driven coil-gun scaling relationships. *IEEE Transactions on Plasma Science*, 2011, vol. 39, no. 1, pp. 220-224. doi: https://doi.org/10.1109/tps.2010.2052266.

9. Bolyukh V.F., Shchukin I.S. *Lineinye induktsionno-dinamicheskie preobrazovateli* [Linear induction-dynamic converters]. Saarbrucken, Germany, LAP Lambert Academic Publ., 2014. 496 p. (Rus).

10. Driga M.D., Weldon W.F., Woodson H.H. Electromagnetic induction launchers. *IEEE Transaction on Magnetics*, 1986, vol. 22, no. 6, pp. 1453-1458. doi: https://doi.org/10.1109/tmag.1986.1064639.
11. Balikci A., Zabar Z., Birenbaum L., Czarkowski D. Improved performance of linear induction launchers. *IEEE Transactions on Magnetics*, 2005, vol. 41, no. 1, pp. 171-175. doi: https://doi.org/10.1109/tmag.2004.839283.
12. Bolyukh V.F., Kocherga A.I., Schukin I.S. Investigation of a linear pulse-induction electromechanical converter with different inductor power supply circuits. *Electrical Engineering & Electromechanics*, 2018, no.1, pp. 21-28. doi: https://doi.org/10.20998/2074-272x.2018.1.03.
13. Bolyukh V.F., Katkov I.I. Influence of the Form of Pulse of Excitation on the Speed and Power Parameters of the Linear Pulse Electromechanical Converter of the Induction Type. *Volume 2B: Advanced Manufacturing*, Nov. 2019, 8 p. doi: https://doi.org/10.1115/imece2019-10388.
14. Bolyukh V.F. Effect of electric conducting element on indicators of linear pulse electromechanical converter induction type. *Technical Electrodynamics*, 2020, no. 3, pp. 22-29. doi: https://doi.org/10.15407/techned2020.03.022.
15. Bolyukh V.F., Oleksenko S.V., Schukin I.S. Efficiency of linear pulse electromechanical converters designed to create impact loads and high speeds. *Electrical Engineering & Electromechanics*, 2015, no. 3, pp. 31-40. doi: https://doi.org/10.20998/2074-272X.2015.3.05.
16. Bolyukh V.F., Shchukin I.S. The thermal state of an electromechanical induction converter with impact action in the cyclic operation mode, *Russian Electrical Engineering*, 2012, vol. 83, no. 10, pp. 571-576. doi: https://doi.org/10.3103/S1068371212100045.

Received 25.10.2020
Accepted 05.12.2020
Published 25.02.2021

V.F. Bolyukh[1], *Doctor of Technical Science, Professor,*
Yu.V. Kashansky[1], *Graduate Student,*
I.S. Schukin[2], *Ph.D., Associate Professor,*
[1] National Technical University «Kharkiv Polytechnic Institute»,
2, Kyrpychova Str., Kharkiv, 61002, Ukraine,
e-mail: vfbolyukh@gmail.com
[2] Firm Tetra, LTD,
18, Gudanova Str., Kharkiv, 61024, Ukraine,
e-mail: tech@tetra.kharkiv.com.ua

How to cite this article:
Bolyukh V.F., Kashansky Yu.V., Schukin I.S. Features of excitation of a linear electromechanical converter of induction type from an AC source. *Electrical Engineering & Electromechanics*, 2021, no. 1, pp. 3-9. **doi: 10.20998/2074-272X.2021.1.01.**

UDC 621.3.048.13 **doi: 10.20998/2074-272X.2021.1.02**

V.V. Vasilevskij, M.O. Poliakov

REPRODUCING OF THE HUMIDITY CURVE OF POWER TRANSFORMERS OIL USING ADAPTIVE NEURO-FUZZY SYSTEMS

Introduction. *One of the parameters that determine the state of the insulation of power transformers is the degree of moisture content of cellulose insulation and transformer oil. Modern systems of continuous monitoring of transformer equipment have the ability to accumulate data that can be used to reproduce the dynamics of moisture content in insulation. The* ***purpose*** *of the work is to reproduce the curve of the of humidity of transformer oil based on the results of measuring the temperature of the upper and lower layers of oil without the need for direct measurement of moisture content by special devices.* ***Methodology***. *The construction of a fuzzy neural network is carried out using networks based on adaptive neuro-fuzzy system ANFIS. The network generated using the Grid Partition algorithm without clustering and Subtractive Clustering.* ***Results***. *The paper presents a comparative analysis of fuzzy neural networks of various architectures in terms of increasing the accuracy of reproducing the moisture content of transformer oil. For training and testing fuzzy neural networks, the results of continuous monitoring of the temperature of the upper and lower layers of transformer oil during two months of operation used. Considered twenty four variants of the architecture of ANFIS models, which differ in the membership functions, the number of terms of each input quantity, and the number of training cycles. The results of using the constructed fuzzy neural networks for reproducing the dynamics of moisture content of transformer oil during a month of operation of the transformer are presented. The reproducing accuracy was assessed using the root mean square error and the coefficient of determination. The test results indicate the sufficient adequacy of the proposed models. Consequently, the RMSE value for the network constructed using Grid Partition method was 0.49, and for the network built using the Subtractive Clustering method – 0.40509.* References 14, tables 2, figures 7.

Key words: **power transformer, transformer oil, cellulose insulation, ANFIS, modeling.**

Вступ. *Одним з параметрів, що визначають стан ізоляції силових трансформаторів, є ступінь вологості целюлозної ізоляції та трансформаторного масла. Сучасні системи неперервного контролю трансформаторного обладнання мають можливість накопичувати дані, які можуть бути використані для відтворювання динаміки вологості ізоляції при зміненні теплового режиму трансформатора.* ***Метою роботи*** *є відтворення кривої вологості трансформаторного масла за результатами вимірювання температури верхніх і нижніх шарів масла без необхідності прямого вимірювання вологовмісту спеціальними пристроями.* ***Методологія***. *Побудова нечіткої нейронної мережі здійснюється із використанням адаптивних нейро-нечітких систем виводу ANFIS. Генерування моделі виконано за методами Grid Partition та Subtractive Clustering.* ***Результати***. *Наведено порівняльний аналіз моделей ANFIS різної архітектури з точки зору підвищення точності відтворення кривої вологовмісту трансформаторного масла за результатами контролю температури його верхніх та нижніх шарів. При навчанні та тестуванні моделей ANFIS використовувались результати неперервного контролю трансформаторного масла протягом двох місяців експлуатації. Розглянуто двадцять чотири варіанти архітектури моделей ANFIS, які відрізняються функціями приналежності, кількістю термів кожної вхідної величини та кількістю циклів навчання. Представлені результати використання побудованих моделей ANFIS для відтворення кривої динаміки вологості масла протягом місяця експлуатації трансформатора. Точність відтворення кривої вологості масла оцінювалась шляхом розрахунку кореневої середньоквадратичної помилки та коефіцієнта детермінації. Результати тестувань свідчать про достатню адекватність запропонованих моделей. Значення кореневої середньоквадратичної помилки для моделі, побудованої із використанням методу Grid Partition, становило 0,49, а для моделі, побудованої з використанням методу Subtractive Clustering – 0,40509.* Бібл. 14, табл. 2, рис. 7.

Ключові слова: **силовий трансформатор, трансформаторне масло, целюлозна ізоляція, ANFIS, моделювання.**

Introduction. Power transformers are one of the most important and expensive components of modern power supply systems. A factor, which has a significant impact on the technical condition of the oil-immersed power transformers in operation, is the moisture content of his cellulose insulation and transformer oil. Sources of moisture in cellulose insulation and transformer oil are the moisture penetration from the atmosphere and the decomposition of cellulose and oil as a result of aging.

Increased moisture content of cellulose insulation can have the following negative consequences [1]:

1. Increasing the thermal-aging rate of cellulose. At a moisture content of 2 % by weight of paper, the thermal-aging rate increases by 6-16 times, and at 4 % – by 12-45 times than at a humidity of 0,3 %.

2. Increased probability of breakdown of transformer oil as a result of the formation of water vapor bubbles during transformer overload.

3. Precipitation of water in transformer oil when the transformer is turned off, which causes a risk of electrical breakdown when the transformer is next turned on.

A number of techniques are currently used to measure the moisture content of cellulose insulation, such as Karl Fischer titration, frequency dielectric spectroscopy, using moisture equilibrium curves with oil Karl Fischer titration data [2, 3]. At this stage, there are no generally accepted methods for directly on-line measuring the moisture content of cellulose insulation.

One of the indirect methods for identifying the degree of moisture content of cellulose insulation is its assessment by the measured humidity of transformer oil and moisture equilibrium curves [4]. At change of a transformer thermal mode there is a migration of moisture in *«cellulose insulation – transformer oil»* system. The direction of moisture migration is due to the fact that the

hygroscopicity of cellulose decreases and the solubility of water in transformer oil increases with a temperature rise [5 – 7]. Thus, the temperature change is a factor that affects the humidity dynamics of transformer oil.

The purpose of the work is to reproduce the curve of the of humidity of transformer oil based on the results of measuring the temperature of the upper and lower layers of oil without the need for direct measurement of moisture content by special devices.

To construct such a curve, the use of the mathematical apparatus of fuzzy logic, in particular, adaptive neuro-fuzzy systems (fuzzy neural network, Adaptive-Network-based Fuzzy Inference System, ANFIS), is promising. Continuous monitoring systems for transformer equipment, which are currently widely used, allow to accumulate significant amounts of data that can be used to train ANFIS models. For example, such systems allow constant monitoring of the temperature and humidity of transformer oil. The results of monitoring the temperature and humidity of transformer oil during 13 days of operation are given in [1]. The obtained graphs demonstrate the presence of a significant correlation between the dynamics of the moisture content in transformer oil and its temperature.

Previous research. Adaptive-Network-based Fuzzy Inference Systems were developed in 1993 [8]. The advantage of ANFIS is the ability to use neural networks to form the rule bases of fuzzy products of the Takagi-Sugeno-Kang models. Such systems are widely used for reproducing and identifying parameters of transformer equipment.

Thus, a description of the adaptive neuro-fuzzy system ANFIS for assess changes in the degree of polymerization of power transformers cellulose insulation is given in [9]. The dielectric characteristics of transformer oil during operation and the gases dissolved in transformer oil were used as input variables for modeling. Authors propose using this model as an alternative to assessing the aging of cellulose insulation under the content of furan derivatives in oil.

In the work [10] the following fuzzy inference methods were used for interpretation the results of analysis of gases dissolved in transformer oil: Mamdani, Takagi Sugeno, and ANFIS. It is noted that the ANFIS model has high accuracy, which can be improved in case of an increase in the data array on which the ANFIS model is trained. A similar problem of identifying and localizing a malfunction in the cellulose insulation of a power transformer based on the analysis of gases dissolved in oil by using ANFIS models were considered in [11, 12].

A method for detecting partial discharges in insulation, in which a nonlinear adaptive system using the ANFIS model is used to solve the noise reduction problem of the measured signal have been proposed in [13]. For training ANFIS model with two inputs is used. A hybrid learning algorithm, in which a generalized bell-shaped membership functions are implemented, is employed.

The results presented in the considered works demonstrate the relevance of using adaptive neuro-fuzzy systems for identification, reproducing and prediction parameters of cellulose insulation and transformer oil. At the same time, in the articles that have been analyzed, the issue of reproducing the curve of the humidity of transformer insulation by using ANFIS is not considered.

Monitoring of temperature and moisture content of transformer oil. A significant part of the transformer park of Ukraine consists of transformers with oil-barrier insulation. The existing systems for continuous monitoring of transformer equipment have the ability to control the following parameters of transformer oil: temperature of the upper and lower layers, measurement of its gas content and degree of moisture content.

The benefits of continuous monitoring of transformer oil humidity are:

1. Taking into account the dynamics of moisture in *«cellulose insulation – transformer oil»* system when a transformer thermal mode changes, while during the scheduled oil sampling and Karl Fischer titration it is necessary that the *«cellulose insulation – transformer oil»* system was in equilibrium state to obtain adequate results.

2. Possibility to estimate the moisture content of cellulose insulation directly during transformer operation using the results of continuous oil control and moisture equilibrium curves.

Relative humidity can be measured by using capacitive thin-film sensors immersed in oil. The moisture sensor should be located in the flowing oil at the top of the transformer tank. Measured relative humidity expressed as a percentage and is equivalent of dissolved (active) water [6]. Methods for measuring the temperature of transformer oil are given in IEC 60076-2. The top-liquid temperature is conventionally determined by sensors immersed in the transformer oil at the top of the tank. The bottom liquid temperature shall be determined by sensors placed at the return headers from coolers or radiators. The results of continuous monitoring of the transformer oil parameters, which were used for training ANFIS models, are shown in Fig. 1, 2.

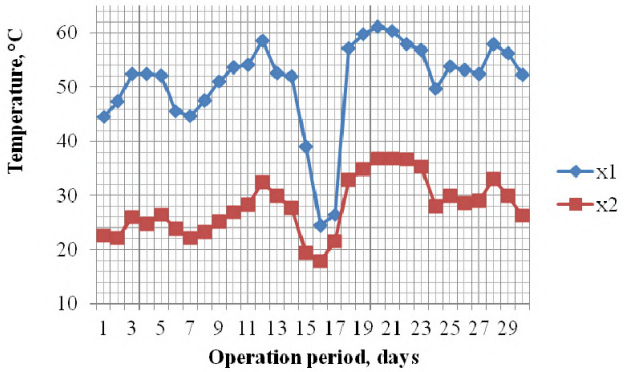

Fig. 1. The results of continuous temperature monitoring of the upper (x1) and lower (x2) layers of transformer oil during the month of operation

Fuzzy neural network which is based on Grid Partition algorithm. Twenty-four variants of ANFIS models were considered in order to select the optimal neural fuzzy network architecture according to the criterion of accuracy. They differ in the membership functions, the number of terms of each input quantity, and the number of training cycles (Table 1).

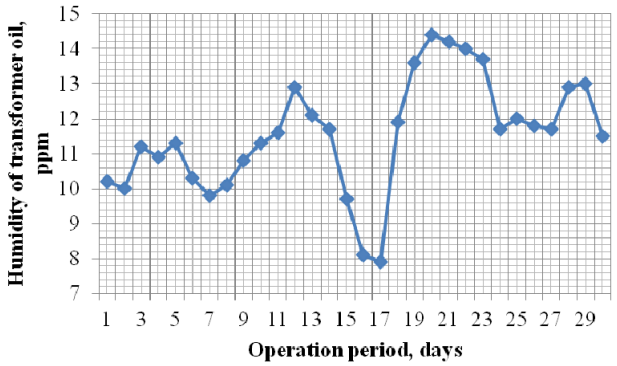

Fig. 2. The results of continuous moisture monitoring of transformer oil during a month of operation

Table 1

Parameters of ANFIS model

ANFIS models	Membership function	Number of terms of each input	Number of training cycles	MAPE, %	RMSE, ppm	R^2
1	trimf	[3 3]	150	3,8	0.53148	0.917
2	trapmf	[3 3]	200	3,69	0.49815	0.888
3	gbellmf	[3 3]	200	7,27	1.4385	0.393
4	gaussmf	[3 3]	250	5,95	1.0115	0.621
5	gauss2mf	[3 3]	450	24,054	7.9	0.0019
6	pimf	[3 3]	1560	31,080	0.64101	0.804280
7	dsigmf	[3 3]	480	12,587	5.89	0.00014
8	psigmf	[3 3]	500	10,284	5.9347	0.00011
9	trimf	[6 6]	200	17,771	8.2638	0.173
10	trapmf	[6 6]	250	29,649	2.678	0.397
11	gbellmf	[6 6]	250	25,562	1.817	0.340
12	gaussmf	[6 6]	150	8,4117	4.4459	0.350
13	gauss2mf	[6 6]	130	22,836	6.94	0.246
14	pimf	[6 6]	630	22,523	7.6274	0.1369
15	dsigmf	[6 6]	260	9,7469	4.4915	0.3271
16	psigmf	[6 6]	260	4,6720	4.4175	0.3311
17	trimf	[9 9]	30	19,703	5.5186	0.0006
18	trapmf	[9 9]	100	19,793	1.9127	0.482
19	gbellmf	[9 9]	50	24,170	5.0538	0.326
20	gaussmf	[9 9]	20	20,175	5.0131	0.302
21	gauss2mf	[9 9]	40	19,892	2.058	0.615
22	pimf	[9 9]	105	8,6381	1.9058	0.53329
23	dsigmf	[9 9]	60	21,305	5.035	0.008617
24	psigmf	[9 9]	60	22,367	5.1968	0.00533

To generate the structure of ANFIS model, Grid Partition algorithm was used. The following membership functions of the input quantities were applied: triangular (trimf), trapezoidal (trapmf), bell-shaped (gbellmf), Gaussian (gaussmf), combination of two Gaussian functions (gauss2mf), pi-shaped (pimf), difference between two sigmoidal membership functions (dsigmf) and product of two sigmoidal membership functions (psigmf). Models containing 3, 6, and 9 terms of input quantities were considered.

Each ANFIS model was trained by using continuous monitoring data snippet of the upper and lower layers of transformer oil temperature of a single power transformer during a month of operation.

The following parameters were accepted as input for ANFIS model: x1 – daily average temperature of the upper layers of transformer oil, °C; x2 – daily average temperature of the lower layers of transformer oil, °C.

The output parameter of the ANFIS model y is the average daily absolute humidity value of transformer oil in ppm.

The total amount of data used for training and testing ANFIS includes 60 values for each parameter x1, x2 and y. This volume is divided into two subgroups - training data and testing data.

The first subgroup, consisting of 30 values for each parameter, was used to train ANFIS. The obtained model was tested using the second subgroup – testing data.

The number of training cycles (epochs) is from 20 to 1560 varies depending on the chosen architecture of the ANFIS model. The training was performed by using a hybrid learning algorithm. After training, ANFIS models were tested by using data not involved in training.

To assess the reliability of the test results, the root mean square error (RMSE) was calculated by using the following well-known expression:

$$RMSE = \sqrt{\frac{1}{N}\sum_{i=1}^{n}(W_{oil}(i)-\tilde{W}_{oil}(i))^2},$$

where N is the total number of data; W_{oil} is the value of moisture content in transformer oil obtained as a result of continuous monitoring of the transformer; $\tilde{W}_{oil}$ is the reproduced value of moisture content in transformer oil.

Lower RMSE value means higher accuracy of the developed model. The lower value RMSE = 0.49 ppm was obtained for ANFIS model No. 2, the topology of which is shown in Fig. 3.

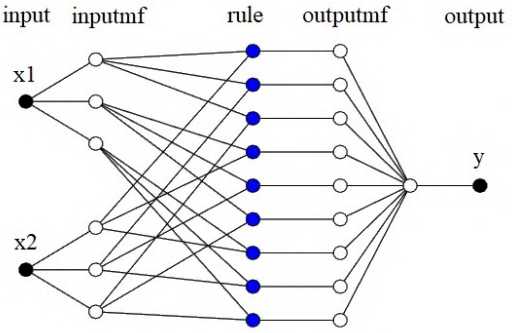

Fig. 3. The structure of ANFIS model No. 2

In addition, the adequacy of the constructed neural networks was estimated by using mean absolute percentage error (MAPE) and the coefficient of determination R^2:

$$R^2(W_{oil},\tilde{W}_{oil}) = \frac{\sum_{i=1}^{n}\left(\tilde{W}_{oil}-\overline{W}_{oil}\right)^2}{\sum_{i=1}^{n}\left(W_{oil}-\overline{W}_{oil}\right)^2},$$

where $\overline{W}_{oil}$ is the average value of experimental data.

The value of the coefficient of determination R^2, lying in the range of 0.8–1 indicates a sufficient adequacy of the developed model. ANFIS models No. 1, No. 2 and No. 6 correspond to this criterion.

ANFIS model No. 2 contains two inputs which are correspond to the temperature values of the upper and lower layers of transformer oil at given times and one

output which is corresponds to the reproduced value of the oil moisture content. Each input variable has 3 terms with trapezoidal membership functions (trapmf). The linear membership function was used for the output quantity.

Grid Partition training error of ANFIS model No. 2 is shown in Fig. 4. It is seen that after 160 epochs, network training has stopped, and the value of the error has stopped decreasing. The results of the ANFIS model testing are shown in Fig. 5.

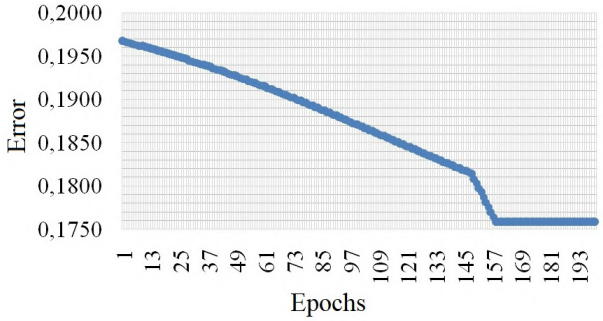

Fig. 4. Grid Partition training error of ANFIS model No. 2

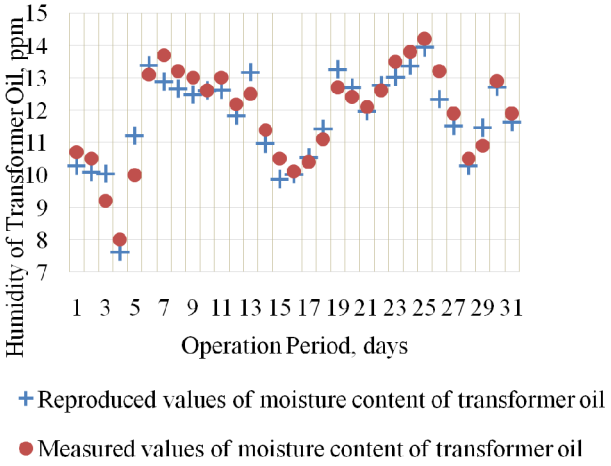

Fig. 5. Testing of ANFIS model No. 2

In the case of a low correlation between the temperature of the transformer oil and the degree of its moisture content, the training efficiency and accuracy of the neuro-fuzzy model test results may decrease.

It is possible to increase the accuracy of the model by taking into account additional parameters that affect the dynamics of transformer oil humidity. Consider the training outcomes of two ANFIS models. The first model has a topology identical to that shown in Fig. 3. The second model differs in the presence of the input parameter x3 – the temperature of the environmental cooling medium, °C.

For training models used the results of continuous monitoring oil parameters of another transformer. The correlation coefficient between the data on the temperature of the upper layers of the oil and its humidity is 0.43 (weak correlation). The training outcomes are given in Table 2.

The obtained value of R^2 and RMSE indicates greater efficiency of training of the model with three inputs.

Table 2

Training error of ANFIS models with low correlation between input and output parameters

ANFIS models	Membership function	Number of terms of each input	MAPE, %	RMSE, ppm	R^2
with 3 inputs	trapmf	[3 3]	0.237	0.0207	0.998
with 2 inputs	trapmf	[3 3]	0.4777	0.344	0.68

Fuzzy neural network which is based on Subtractive Clustering algorithm. The purpose of clustering is the partition large amounts of data into groups of similar objects (cluster centers), which allows to reproduce the system behavior more accurate [14]. In the process of reproducing the moisture content of transformer oil, the Subtractive Clustering method was used to improve the fuzzy model of moisture dynamics.

An ANFIS model based on the Subtractive Clustering algorithm is built, trained and tested. The standard values are accepted when the network structure is forming: Range of influence – 0.5; Squash factor – 1.25; Accept ratio – 0.5; Reject Ratio – 0.15. The resulting error in training of the neural network was 0.20337, after which the network was tested. Figure 6 shows the results of testing of ANFIS model based on Subtracting Clustering algorithm.

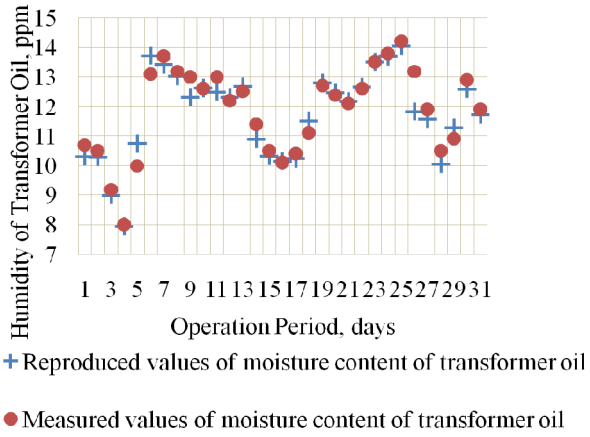

Fig. 6. Testing of ANFIS model based on Subtracting Clustering algorithm

Obtained value of RMSE of ANFIS model based on Subtracting Clustering algorithm test was 0.40509 ppm. It is less than the RMSE value of a fuzzy neural network constructed by using the Grid Partition method. Obtained value of R^2 of the fuzzy neural network constructed by the Subtractive Clustering method amounted to 0.929336 and MAPE value is 2.5 %. Obviously, a network built by using the Subtractive Clustering algorithm is not inferior in accuracy to a network built by using the Grid Partition algorithm. Figure 7 shows moisture content of transformer oil reproducing error by using ANFIS model No. 2 and model based on Subtracting Clustering algorithm in %. It is seen from the graph that the constructed ANFIS models have sufficient accuracy (received error less than 15 %) and can be used for solve the problem of reproducing the humidity of transformer oil of power oil-immersed transformers.

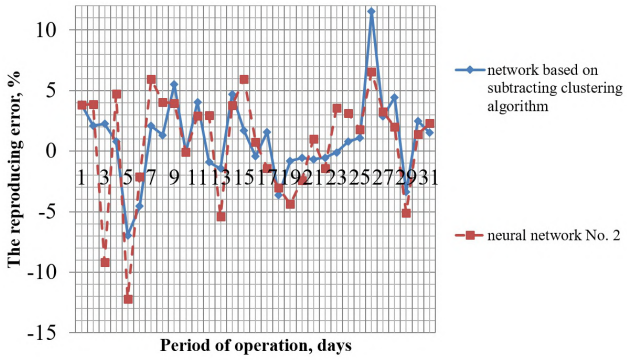

Fig. 7. Moisture content of transformer oil reproducing error by using ANFIS model No. 2 and model based on Subtracting Clustering algorithm

Conclusions.

1. The training, testing and comparison of fuzzy neural networks with different architecture for reproduce the curve of the humidity of transformer oil on the basis of continuous temperature control of the upper and lower layers of oil has been investigated.

2. Studies have shown that the use of fuzzy neutral networks allows to accurately at least 85 % to reproduce the dynamics of the moisture content in the transformer oil during the operation of the transformer without the need for direct measurement of humidity by special devices.

3. To improve reproducing accuracy in the formation of the structure of the neural network, the Grid Partition and Subtractive Clustering methods were used. The neural network was tested by using the results of continuous monitoring of transformer parameters during a month of operation. The RMSE value for the first case was 0.49 (obtained MAPE value – 3.69 %), and for the second case – 0.40509 (MAPE – 2.5 %).

4. Achieving adequate results to reproduce the humidity curve of power transformers oil for each single transformer requires retraining the model using continuous monitoring data from that transformer. In addition, other factors can be taken into account in the model structure, such as the operating mode of the transformer cooling system and the temperature of the cooling medium. In this case, the corresponding input parameters x3 and x4 are add into the model.

Conflicts of interests. The authors declare no conflict of interest.

REFERENCES

1. Saha T.K., Purkait P. *Transformer Ageing: Monitoring and Estimation Techniques*. John Wiley & Sons Singapore Pte. Ltd., 2017. doi: https://doi.org/10.1002/9781119239970.

2. Martin D., Saha T. A review of the techniques used by utilities to measure the water content of transformer insulation paper. *IEEE Electrical Insulation Magazine*, 2017, vol. 33, no. 3, pp. 8-16. doi: https://doi.org/10.1109/MEI.2017.7906158.

3. Liu J., Fan X., Zhang Y., Zheng H., Zhu M. Quantitative evaluation for moisture content of cellulose insulation material in paper/oil system based on frequency dielectric modulus technique. *Cellulose*, 2020, vol. 27. doi: https://doi.org/10.1007/s10570-019-02820-3.

4. Cheng J., Robalino D.M., Werelius P., Ohlen M. Advanced Technique for Moisture Condition Assessment in Power Transformers. *Journal of International Council on Electrical Engineering*, 2014, vol. 4. pp. 185-191. doi: https://doi.org/10.5370/JICEE.2014.4.3.185.

5. Sikorski W., Walczak K., Przybylek P. Moisture Migration in an Oil-Paper Insulation System in Relation to Online Partial Discharge Monitoring of Power Transformers. *Energies*, 2016, vol. 9, no. 12, p. 1082. doi: https://doi.org/10.3390/en9121082.

6. Andrienko P.D., Sakhno A.A., Konogray S.P., Skrupskaya L.S. Online Monitoring of the Insulation Water Content Characteristics of the Oilfilled Electrical Equipment. *Electrical Engineering and Power Engineering*, 2014, vol. 2, pp. 32-40. doi: https://doi.org/10.15588/1607-6761-2014-2-5.

7. Przybylek P. The influence of temperature and aging of cellulose on water distribution in oil-paper insulation. *IEEE Transactions on Dielectrics and Electrical Insulation*, 2013, vol. 20, no. 2, pp. 552-556. doi: https://doi.org/10.1109/TDEI.2013.6508758.

8. Jang J.-S.R. ANFIS: Adaptive-network-based fuzzy inference system. *IEEE Transaction on Systems, Man, and Cybernetics*, 1993, vol. 23, no. 3, pp. 665-685. doi: https://doi.org/10.1109/21.256541.

9. Prasojo R.A., Diwyacitta K., Suwarno, Gumilang H. Transformer paper expected life estimation using ANFIS based on oil characteristics and dissolved gases (Case study: Indonesian transformers). *Energies*, 2017, vol. 10, no. 8, p. 1135. doi: https://doi.org/10.3390/en10081135.

10. Aghaei J., Gholami A., Shayanfar H.A., Dezhamkhooy A. Dissolved gas analysis of transformers using fuzzy logic approach. *European Transactions on Electrical Power*, 2009, vol. 20, pp. 630-638. doi: https://doi.org/10.1002/etep.343.

11. Khan S.A., Equbal M.D., Islam T. ANFIS based identification and location of paper insulation faults of an oil immersed transformer. *2014 6th IEEE Power India International Conference (PIICON)*, Delhi, 2014, pp. 1-6. doi: https://doi.org/10.1109/poweri.2014.7117715.

12. Bin Yaacob M.M., Hussein A.R., Bin Othman M.F. DGA Method-Based ANFIS Expert System for Diagnosing Faults and Assessing Quality of Power Transformer Insulation Oil. *Modern Applied Science*, 2016, vol. 10, no. 1, pp. 13-22. doi: https://doi.org/10.5539/mas.v10n1p13.

13. Jahangir H., Hajipour E., Vakilian M., Akbari A., Blackburn T., Phung B.T. A method to capture and de-noise partial discharge pulses using discrete wavelet transform and ANFIS. *International Transactions on Electrical Energy Systems*, 2014, vol. 25, no. 11, pp. 2696-2717. doi: https://doi.org/10.1002/etep.1986.

14. Chiu S.L. Fuzzy model identification based on cluster estimation. *Journal of Intelligent and Fuzzy Systems*, 1994, vol. 2, no. 3, pp. 267-278. doi: https://doi.org/10.3233/ifs-1994-2306.

Received 10.10.2020
Accepted 30.11.2020
Published 25.02.2021

V.V. Vasilevskij[1], *Ph.D., Senior Lecturer,*
M.O. Poliakov[1], *Ph.D., Professor,*
[1] Zaporizhzhia Polytechnic National University,
64, Zhukovsky Str., Zaporizhzhia, Ukraine, 69063,
e-mail: lisses@ukr.net, polyakov@zntu.edu.ua

How to cite this article:
Vasilevskij V.V., Poliakov M.O. Reproducing of the humidity curve of power transformers oil using adaptive neuro-fuzzy systems. *Electrical Engineering & Electromechanics*, 2021, no. 1, pp. 10-14. **doi: 10.20998/2074-272X.2021.1.02.**

UDC 621.313 **doi: 10.20998/2074-272X.2021.1.03**

V.V. Goman, V.A. Prakht, V.M. Kazakbaev, V.A. Dmitrievskii, E.A. Valeev, A.S. Paramonov

ANALYSIS OF THE PAYBACK PERIOD OF A MODERNIZED PUMP UNIT WITH INDUCTION ELECTRIC MOTORS OF ADVANCED ENERGY EFFICIENCY CLASSES

Aim. *The comparative analysis of energy consumption, electricity costs during lifetime cycle and payback period of a pump unit with 90 kW 2-pole induction motors, belonging to various energy efficiency classes, feeding directly from power grid.* ***Methods.*** *The examined operating modes aligned with a typical operating cycle of a pump unit with approximately constant flow rate of 75-110 % of the rated flow. The calculations were based on the pump and induction motors nameplate data, which, in their turn, were based on the manufacturers' experimental data.* ***Results.*** *The calculations of energy consumption, electricity costs and payback periods of a pump unit with 90 kW 2-pole induction motors, feeding directly from power grid have been performed in the article. The application of induction motors belonging to IE2, IE3 and IE4 energy efficiency classes has been discussed.* ***Practical value.*** *It has been demonstrated, than in case of replacement of an induction motor of energy efficiency class IE2 due to planned retrofit, payback period for an IE4 induction motor is 2.18 years, energy savings within a calculated 20-year operating period are 268MW·h, which makes €41110 in money terms. Under the same conditions, the replacement of an induction motor of energy efficiency class IE2 with an induction motor of energy efficiency class IE3 will allow to save 88 MW·h within a calculated operating period, which, expressed in monetary terms, is €13500 and the payback period is 5.11 years. Thus, the article proves that despite a higher initial price, the choice of an induction motor of energy efficiency class IE4 tends to be more economically advantageous.* References 27, tables 4, figures 1.

Key words: **centrifugal pump, energy efficiency, energy efficiency class, induction motor, throttling control, energy saving, lifetime cycle, payback period.**

Мета. *Порівняльний аналіз розрахунків енергоспоживання, витрат на електроенергію протягом життєвого циклу і термінів окупності насосної установки з 2-полюсними асинхронними електродвигунами потужністю 90 кВт різних класів енергоефективності, що живляться безпосередньо від електричної мережі.* ***Методика.*** *Розглянуті режими роботи відповідають типовому циклу роботи, характерному для насосних установок з приблизно постійною витратою 75-110 % від номінального. Розрахунок ґрунтувався на паспортних даних насоса і електродвигунів, які в свою чергу засновані на експериментальних даних виробників.* ***Результат.*** *У статті проведено розрахунки енергоспоживання, витрат на електроенергію і термінів окупності насосної установки з 2-полюсними асинхронними електродвигунами потужністю 90 кВт, що живляться безпосередньо від електричної мережі. Розглянуто застосування електродвигунів з класами енергоефективності IE2, IE3 і IE4.* ***Практичне значення.*** *Показано, що в разі заміни електродвигуна класу енергоефективності IE2 в зв'язку з плановою модернізацією електродвигуном класу енергоефективності IE4 термін окупності становить 2,18 року, економія електроенергії протягом розрахункового 20-річного терміну експлуатації складає 268 МВт · год, що в грошовому вираженні становить 41110 €. При тих же умовах заміна електродвигуна класу енергоефективності IE2 на електродвигун класу енергоефективності IE3 дозволить досягти економії електроенергії протягом розрахункового терміну експлуатації 88 МВт·год, що становить в грошовому вираженні 13500 €, і термін окупності є 5,11 року. Таким чином, в статті показано, що незважаючи на більш високу початкову вартість, вибір електродвигуна класу енергоефективності IE4 більш вигідний з економічної точки зору.* Бібл. 27, табл. 4, рис. 1.

Ключові слова: **відцентровий насос, енергоефективність, клас енергоефективності, асинхронний електродвигун, дросельне регулювання, енергозбереження, життєвий цикл, термін окупності.**

Цель. *Сравнительный анализ расчетов энергопотребления, затрат на электроэнергию в течение жизненного цикла и сроков окупаемости насосной установки с 2-полюсными асинхронными электродвигателями мощностью 90 кВт различных классов энергоэффективности, питающимися напрямую от электрической сети.* ***Методика*** *Рассматриваемые режимы работы соответствовали типовому циклу работы, характерному для насосных установок с приблизительно постоянным расходом 75-110 % от номинального. Расчет основывался на паспортных данных насоса и электродвигателей, которые в свою очередь основаны на экспериментальных данных производителей.* ***Результат*** *В статье произведен расчеты энергопотребления, затрат на электроэнергию и сроков окупаемости насосной установки с 2-полюсными асинхронными электродвигателями мощностью 90 кВт, питающимися напрямую от электрической сети. Рассмотрено применение электродвигателей с классами энергоэффективности IE2, IE3 и IE4.* ***Практическое значение.*** *Показано, что в случае замены электродвигателя класса энергоэффективности IE2 в связи с плановой модернизацией электродвигателем класса энергоэффективности IE4 срок окупаемости для электродвигателя класса энергоэффективности IE4 составляет 2,18 года, экономия электроэнергии в течение расчетного 20-летнего срока эксплуатации составляет 268 МВт·ч, что в денежном выражении составляет 41110 €. При тех же условиях замена электродвигателя класса энергоэффективности IE2 на электродвигатель класса энергоэффективности IE3 позволит достичь экономии электроэнергии в течение расчетного срока эксплуатации 88 МВт·ч, что составляет в денежном выражении 13500 €, и срока окупаемости 5,11 года. Таким образом, в статье показано, что, несмотря на более высокую начальную стоимость, выбор электродвигателя класса энергоэффективности IE4 более выгоден с экономической точки зрения.* Библ. 27, табл. 4, рис. 1.

Ключевые слова: **центробежный насос, энергоэффективность, класс энергоэффективности, асинхронный электродвигатель, дроссельное регулирование, энергосбережение, жизненный цикл, срок окупаемости.**

Introduction. In the world and, in particular, in the European Union, work has long and consistently been carried out to increase the energy efficiency of household appliances, industrial equipment and technological processes. An important part of it is the establishment of energy efficiency classes for electric motors, both powered directly from the electrical network [1], and operating as part of a variable frequency drive (VFD) [2].

This is due to the fact that according to the research [3], electric motors consume 46 % of the electricity generated in the world, and the share of electricity consumption by electric motors in industry is about 70 %.

In accordance with the EU regulation [4] of 2009, with the addition of 2014, from January 1, 2017 all electric motors with power from 0.75 to 375 kW, with the exception of those specified in the Standard, must have an energy efficiency class of at least IE3 or IE2, if they are used as part of a VFD. In 2019, the requirements for the energy efficiency of electric motors were updated in the new EU regulation [5], according to which the scope of application of the requirements was expanded and the timing of the introduction of more stringent requirements was determined. So, in [5] it is indicated that from July 1, 2021 2-, 4-, 6-, 8-pole electric motors with power from 0.75 to 1000 kW, with the exception of those specified in the Standard, must have an energy efficiency class of at least IE3. From July 1, 2023 2, 4, 6-pole electric motors from 75 to 200 kW inclusive must have an energy efficiency class of at least IE4 [5]. In the USA, Switzerland, Turkey, Canada, Mexico, South Korea, Singapore, Japan, Saudi Arabia, Brazil, Taiwan and a number of other countries, the use of electric motors with an energy efficiency class of at least IE3 is mandatory [6].

The relevance of the work. According to a European Commission report [3], pumping systems account for almost 22 % of the energy consumed by electric motors worldwide. Therefore, studying the possibilities of increasing the energy efficiency of pumping units is an urgent task.

Centrifugal pumps often do not require a wide control range, as well as high starting torque and speed. Therefore, induction electric motors (IMs), operating directly from the electrical network, are widely used in the drives of the mechanisms mentioned above. In this case, the regulation of the performance of the pumps is carried out using valves (throttle control), by means of a controlled change in the characteristics of the hydraulic network. It is known that due to the high costs of frequency converters, not only pumps are characterized by the use of electric motors powered directly from the electrical network. For example, according to the European Commission [1], the share of VFD was about 30 % for Germany, and about 20 % for Switzerland, according to the study described in [7].

Increasing the energy efficiency of a pumping unit is possible due to changes in the hydraulic network on which the unit operates, the use of VFDs, optimization and distribution of loads (in the case of parallel pumping units), as well as due to the proper selection of unit elements, in particular the use of higher energy efficiency class electric motors [8]. A large number of articles [9-12] are devoted to the issues of reducing the energy consumption of pumping units by using electric motors of different operating principles of higher energy efficiency classes. However, in all of the above-mentioned articles [9-12], a method of regulating pump performance using a VFD is considered. This article discusses the use of electric motors with a higher energy efficiency class, as the most relevant way to improve the energy efficiency of pumps with throttle control.

Note that the classification of electric motors for energy efficiency in the regulatory documents [1, 5] is based only on the efficiency in the nominal operating mode, i.e. at rated shaft power, and does not take into account the efficiency of electric motors at a load different from the rated load, which is more or less characteristic of electric motors as part of pumping units. So, for circulating pumps with power up to 2.5 kW operating mainly with variable flow rate according to [13-15], the relative operating time in the nominal mode does not exceed 6 %.

For water pumps, according to [16], standard operating modes with flaw rate of 75 %, 100 % and 110 % of the nominal flow rate are adopted, and the requirements for energy efficiency in these modes are presented. In [14, 15], a typical operating cycle for these modes is given, typical for pumping systems with an approximately constant flow rate. This profile assumes operation 25 % of the time at 75 % flow, 50 % of the time at nominal flow rate and 25 % of the time at 110 %.

Literature review. In [17], a pump unit with nominal power of 2.2 kW operating at a variable flow rate was analyzed. Line-start permanent magnet synchronous motors and IMs with energy efficiency classes IE3 and IE4 were considered. Annual electricity consumption, annual electricity costs, share of life cycle costs determined by the cost of electricity and annual energy savings in kind and in monetary terms when choosing an electric motor were calculated. However, the calculation of the payback period was not made, since the main goal of the article was to show that the choice of an electric motor only according to the energy efficiency class, which is assigned according to the efficiency at the rated load, does not lead to the minimum energy consumption when operating a pumping unit with a variable flow rate according to the typical operating cycle given in [13].

In the article [18], the analysis of the same indicators was carried out for a pumping unit operating at an approximately constant flow rate, with power of 11 kW with two IMs of energy efficiency classes IE1 and IE2, and the payback periods of technical solutions for replacing an electric motor of class IE1 with an electric motor of class IE2 were calculated. However, it should be noted that replacing the IE1 energy efficiency class with IE2 electric motors is relevant only in some countries. For example, in the countries of the Eurasian Economic Union (Russia, Kazakhstan, Belarus, Kyrgyzstan, Armenia), the legislation of which in the field of energy efficiency [19] does not prohibit the use of electric motors of the IE1 class until September 1, 2021.

Thus, as the review of literature sources shows, a comparative analysis of energy consumption and economic indicators of operation of electric motors of energy efficiency classes IE2, IE3, IE4 in pumping units of medium and high power with throttle regulation and approximately constant flow rate has not been previously carried out.

The goal of the work is a comparative analysis of energy consumption and payback periods of a pumping unit using 2-pole IMs of energy efficiency classes IE2 [20], IE3 [21] and IE4 [22] of power of 90 kW from one manufacturer, powered directly from the mains, for a

typical cycle of operation, typical for an approximately constant flow rate according to [14, 15].

Initial data and calculation methods. For the calculation, the data of the pump Grundfos NB 65-315/308 AF2ABAQE – 97836805 [23] with rated power P_{RATE} = 90 kW and rated speed n_{RATE} = 2980 rpm are used. Pump data are given in Table 1, where Q_{BEP} is the flow rate at the best efficient point (BEP) and H_{BEP} is the pump pressure at the BEP.

Table 1

Pump passport data

Parameter	Value
Type	NB 65-315/308
P_{RATE}, W	90 000
n, rpm	2980
Q_{BEP}, m³/h	182
H_{BEP}, m	120.6
Efficiency, %	73.8

The graphs of the main characteristics of the pump (dependence of pressure, power consumption and efficiency on flow) are shown in Fig. 1.

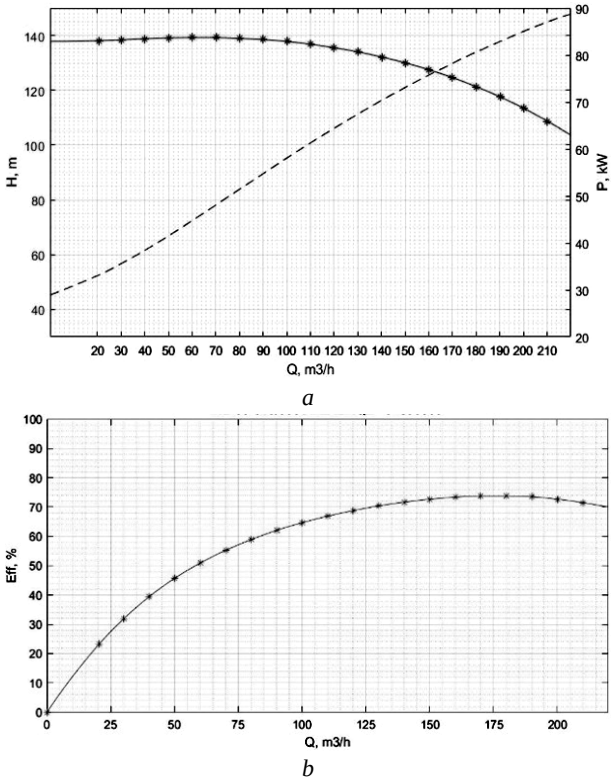

a

b

Fig. 1. Interpolated pump characteristics and reference points from catalog data:
a) *Q-H* characteristic and power consumption versus flow rate;
b) dependence of pump efficiency on flow

The active power of the *m*-th IM in the *i*-th operating mode consumed from the electrical network was calculated according to (1) taking into account the interpolated values of the efficiency of electric motors $\eta_{M.i.m}$ and the mechanical power $P_{mech.i.m}$ for modes corresponding to a typical cycle of operation, similar to the approach used in work [17]

$$P_{1.i.m} = P_{mech.i.m} / \eta_{M.i.m}. \quad (1)$$

The annual energy consumption for each IM in the considered typical operating cycle of the pumping unit, taking into account year-round and round-the-clock operation, was determined as

$$E_{d.m.} = 365 \cdot t_{\Sigma} \cdot \sum_{i=1}^{3} \left(P_{1.i.m} \cdot \frac{t_i}{t_{\Sigma}} \right). \quad (2)$$

where t_{Σ} is the total operating time taken equal to 24 h and t_i is the operating time in each mode.

Electricity cost (€) at tariff GT = € 0.188 / kWh for industrial consumers in Germany in the second half of 2019 [24] was determined by the formula

$$C_{y.m} = E_{y.m} \cdot GT. \quad (3)$$

The annual cost savings in electricity were calculated as

$$S_{y.31} = C_{y.3} - C_{y.1};\ S_{y.32} = C_{y.3} - C_{y.2};\ S_{y.21} = C_{y.2} - C_{y.1}. \quad (4)$$

Taking into account that the life cycle of pumping units according to the data [25, 26] is about 15–20 years, for the calculations the service life was assumed n = 20 years. The electricity costs were calculated over the life cycle of the pumping unit, since the total cost of the life cycle of a pumping unit is mainly the cost of consumed electricity (at least more than 50-60 %) [25, 26]. The net present value (*NPV*) of the life cycle, determined by the cost of electricity consumed, was calculated as

$$C_{LCCen.m} = C_{y.m}/(1 + (y - p))^n, \quad (5)$$

where y is the interest rate (taken equal to 0.04) and p is the expected annual inflation (taken equal to 0.02) [25, 26].

The difference in electricity costs during the life cycle of the *m*-th IM relative to the existing IM was determined as

$$\Delta C_{LCCen.3m} = C_{LCCen.3} - C_{LCCen.m}. \quad (6)$$

In the case of replacing the existing IM of the IE2 energy efficiency class with an IE4 or IE3 IM, the payback period T_m of the *m*-th IM was determined as

$$T_m = C_{iic.m} / S_{y.3m}. \quad (7)$$

where $C_{iic.m}$ is the initial cost of the considered electric motors, which are given in Table 4 according to [27].

Results of calculations and their discussion. Table 2 shows the results of calculating the pump operating modes.

Table 2

Results of calculating the pump operating modes

Number of modes (i)	1	2	3
Q_i, %	75	100	110
Q_i, m³/h	136.5	182.0	200.2
$H_{pump.i}$, m	132.6	120.6	113.9
$\eta_{pump.i}$, %	71.3	73.8	72.7
$P_{mech.i}$, W	69176	81045	85471
$P_{mech.i}$, %	76.86	90.05	94.97

Table 3 shows the efficiency values of electric motors according to the catalog for loads of 50 %, 75 % and 100 %, as well as for each operating mode of the pump in accordance with the considered typical operating cycle.

The calculation results using (1)-(7) are shown in Table 4. If an IE2 electric motor in an existing pumping unit is replaced by an IE4 electric motor, the energy savings over the design life are 268 MWh, which is € 41,100 in monetary terms, and the payback period is 2.18 years. In case of replacement with an electric motor of the energy efficiency class IE3, the energy savings during the

Table 3

Initial and interpolated efficiency values of electric motors

m	Electric motor type, IE class	Efficiency according to catalog data, % at load		
		50 %	75 %	100 %
1	IM WEG W22, IE4	95.5	96.2	96.5
2	IM WEG W22, IE3	94.3	95.2	95.2
3	IM WEG W22, IE2	94.0	94.6	94.6
m	Electric motor type, IE class	Interpolated values of efficiency $\eta_{M.i.m}$, % in operating modes		
		1	2	3
1	IM WEG W22, IE4	96.27	96.43	96.46
2	IM WEG W22, IE3	95.20	95.20	95.20
3	IM WEG W22, IE2	94.60	94.60	94.60

Table 4

Results of calculating energy consumption and electrical energy savings

m	1	2	3
Electric motor type, IE class	АД WEG W22, IE4	АД WEG W22, IE3	АД WEG W22, IE2
$E_{y.m}$, MWh	719.5	728.5	732.9
$C_{y.m}$, thousand €	135.27	136.96	137.78
$S_{y.3m}$, €	2513.4	824.8	0
$C_{LCCen.m}$, thousand €	2211.9	2239.5	2253.0
$\Delta C_{LCCen.3m}$, thousand €	41.1	13.5	0
$C_{iic.m}$, €	5486	4220	0
T_m, years	2.18	5.11	–

design life are 88 MWh, which is € 13,500 in monetary terms, the payback period is 5.11 years. Thus, for the considered conditions, it is advisable to modernize the pumping unit by replacing the electric motor of the IE2 energy efficiency class. Here, despite the higher cost, the use of an electric motor of the energy efficiency class IE4 will provide a significantly shorter payback period than the use of an electric motor of the class IE3.

Conclusions. In the work, calculations of electricity consumption and cost indicators of energy savings for induction electric motors of IE2, IE3, IE4 classes were made, in the case if they are used in a pumping unit operating with flow rate varying within 75-110 % of the nominal one. A comparison was made of the payback periods and electrical energy costs throughout the life cycle for the case of replacing the electric motor in connection with a planned modernization. The payback period for replacing an IE2 motor with an IE4 motor is 2.18 years. Here, the payback period in case of replacement of an electric motor of the energy efficiency class IE2 with an electric motor of the energy efficiency class IE3 is much longer and amounts to 5.11 years. Thus, the choice of an IE4 motor is more cost-effective when upgrading, even though its cost is 30 % higher than that of an IE3 motor. It should be noted that such a technical solution will be especially relevant in light of the requirements of the document [5], according to which in the European Union the use of IE4 class electric motors for powers above 75 kW is mandatory from July 1, 2023.

Acknowledgment. The work was partially supported by the Ministry of Science and Higher Education of the Russian Federation (through the basic part of the government mandate, Project No. FEUZ-2020-0060).

Conflict of interests. The authors declare no conflicts of interest.

REFERENCES

1. *Rotating electrical machines – Part 30-1: Efficiency classes of line operated AC motors (IE code).* IEC 60034-30-1/ Ed. 1; IEC: 2014-03. Available at: https://webstore.iec.ch/publication/136 (accessed on 10 June 2020).

2. *Rotating electrical machines – Part 30-2: Efficiency classes of variable speed AC motors (IE-code)* IEC 60034-30-2/ IEC: 2016-12. Available at: https://webstore.iec.ch/publication/30830 (accessed on 10 June 2020).

3. *European Commission. Study on improving the energy efficiency of pumps*, 2001. Available at: https://www.jacobalbertsen.dk/komposit/Darmstadtrapport.pdf (accessed on 10 June 2020).

4. *European Commission Regulation (EC) No. 640/2009 implementing Directive 2005/32/ EC of the European Parliament and of the Council with Regard to Ecodesign Requirements for Electric Motors*, (2009), amended by Commission Regulation (EU) No 4/2014 of January 6, 2014. Document 32014R0004. Available at: https://eur-lex.europa.eu/legal-content/EN/TXT/?uri=CELEX%3A32014R0004 (accessed on 11 June 2020).

5. *Commission Regulation (EU) 2019/1781 of 1 October 2019 laying down ecodesign requirements for electric motors and variable speed drives pursuant to Directive 2009/125/EC of the European Parliament and of the Council, amending Regulation (EC) No 641/2009 with regard to ecodesign requirements for glandless standalone circulators and glandless circulators integrated in products and repealing Commission Regulation (EC) No 640/2009*. Available at: https://eur-lex.europa.eu/legal-content/EN/TXT/PDF/?uri=CELEX:32019R1781&from=EN (accessed on 10 June 2020).

6. *Efficiency regulations for motors: international norms. NORD DRIVESYSTEMS Group, S4700 Part. No. 6069202 / 4019*. Available at: https://www.nord.com/cms/media/documents/bw/S4700_6069202_4019_Screen.pdf (accessed on 11 June 2020).

7. Phillips R., Tieben R. Improvement of Electric Motor Systems in Industry (IEMSI). *Proceedings of the 10th international conference on energy efficiency in motor driven systems (EEMODS' 2017)*, Rome, Italy, September 6-8, 2017. pp. 53-67. doi: http://dx.doi.org/10.2760/345473.

8. Arun Shankar V.K., Umashankar S., Paramasivam S., Hanigovszki N. A comprehensive review on energy efficiency enhancement initiatives in centrifugal pumping system. *Applied Energy*, 2016, vol. 181, pp. 495-513. doi: https://doi.org/10.1016/j.apenergy.2016.08.070.

9. Ahonen T., Orozco S.M., Ahola J., Tolvanen J. Effect of electric motor efficiency and sizing on the energy efficiency in pumping systems. *2016 18th European Conference on Power Electronics and Applications (EPE'16 ECCE Europe)*, Sep. 2016, Karlsruhe, pp. 1-9. doi: https://doi.org/10.1109/epe.2016.7695671.

10. Van Rhyn P., Pretorius J.H.C. Utilising high and premium efficiency three phase motors with VFDs in a public water supply system. *2015 IEEE 5th International Conference on Power Engineering, Energy and Electrical Drives (POWERENG)*, May 2015, Riga, pp. 497-502. doi: https://doi.org/10.1109/powereng.2015.7266367.

11. Brinner T.R., McCoy R.H., Kopecky T. Induction versus permanent-magnet motors for electric submersible pump field and laboratory comparisons. *IEEE Transactions on Industry Applications*, 2014, vol. 50, no. 1, pp. 174-181. doi: https://doi.org/10.1109/tia.2013.2288203.

12. Kazakbaev V., Prakht V., Dmitrievskii V., Ibrahim M., Oshurbekov S., Sarapulov S. Efficiency analysis of low electric power drives employing induction and synchronous reluctance motors in pump applications. *Energies*, 2019, vol. 12, no. 6, p. 1144. doi: https://doi.org/10.3390/en12061144.
13. *Commission Regulation (EC) No 641/2009 of July 22, 2009 implementing Directive 2005/32/EC of the European Parliament and of the Council with regard to ecodesign requirements for glandless standalone circulators and glandless circulators integrated in products, amended by Commission Regulation (EU) No 622/2012 of July 11, 2012*. Document 02009R0641-20170109. Available at: https://eur-lex.europa.eu/legal-content/EN/TXT/?uri=CELEX%3A02009R0641-20170109 (accessed on 11 June 2020).
14. *Extended product approach for pumps*, Copyright © 2014 by Europump. Published by Europump. Available at: http://europump.net/uploads/Extended%20Product%20Approach%20for%20Pumps%20-%20A%20Europump%20guide%20(27OCT2014).pdf (accessed on 11 June 2020).
15. Stoffel B. *Assessing the Energy Efficiency of Pumps and Pump Units. Background and Methodology*. Elsevier: Amsterdam, The Netherlands, 2015. doi: https://doi.org/10.1016/b978-0-08-100597-2.00009-4.
16. *Commission regulation (EU) No 547/2012 of June 25, 2012 implementing Directive 2009/125/EC of the European Parliament and of the Council with regard to ecodesign requirements for water pumps.* Available at: https://eur-lex.europa.eu/legal-content/EN/TXT/?uri=CELEX%3A32012R0547 (accessed on 11 June 2020).
17. Goman V.V., Oshurbekov S.Kh., Kazakbaev V.M., Prakht V.A., Dmitrievskii V.A. Comparison of energy consumption of various electrical motors operating in a pumping unit. *Electrical engineering & electromechanics*, 2020, no. 1, pp. 16-24. doi: https://doi.org/10.20998/2074-272X.2020.1.03.
18. Oshurbekov S.Kh., Kazakbaev V.M., Prakht V.A., Dmitrievskii V.A., Paramonov A.S. Analysis of electricity consumption of induction motors of IE1 and IE2 efficiency classes in a 11 kW pump installation. *Electrical engineering & electromechanics*, 2020, no. 5, pp. 18-24. doi: https://doi.org/10.20998/2074-272X.2020.5.03.
19. *Technical regulations of Eurasian Economic Union (TR EAEC 048/2019). About requirements of the energy efficiency of power consuming devices.* (Rus). Available at: https://www.garant.ru/products/ipo/prime/doc/73240518/ (accessed on 01 June 2020).
20. *W22 High Efficiency IE2 90 kW 2P 280S/M 3Ph 380-415/660//460 V 50 Hz IC411 – TEFC – B34T. Product Details*. Available at: https://www.weg.net/catalog/weg/CI/en/Electric-Motors/Low-Voltage-IEC-Motors/General-Purpose-ODP-TEFC/Cast-Iron-TEFC-General-Purpose/W22---Cast-Iron-TEFC-General-Purpose/W22-IE2/W22-IE2-90-kW-2P-280S-M-3Ph-380-415-660-460-V-50-Hz-IC411---TEFC---B34T/p/12999061 (accessed on 01 June 2020).
21. *W22 Premium Efficiency IE3 90 kW 2P 280S/M 3Ph 380-415/660//460 V 50 Hz IC411 – TEFC – B3T. Product Details*. Available at: https://www.weg.net/catalog/weg/CI/en/Electric-Motors/Low-Voltage-IEC-Motors/General-Purpose-ODP-TEFC/Cast-Iron-TEFC-General-Purpose/W22---Cast-Iron-TEFC-General-Purpose/W22-IE3/W22-IE3-90-kW-2P-280S-M-3Ph-380-415-660-460-V-50-Hz-IC411---TEFC---B3T/p/12862411 (accessed on 10 June 2020).
22. *W22 Super Premium Efficiency IE4 90 kW 2P 280S/M 3Ph 400/690//460 V 50 Hz IC411 – TEFC – B3T. Product Details*. Available at: https://www.weg.net/catalog/weg/AZ/en/Electric-Motors/Low-Voltage-IEC-Motors/General-Purpose-ODP-TEFC/Cast-Iron-TEFC-General-Purpose/W22---Cast-Iron-TEFC-General-Purpose/W22-IE4/W22-IE4-90-kW-2P-280S-M-3Ph-400-690-460-V-50-Hz-IC411---TEFC---B3T/p/12774372 (accessed on 10 June 2020).
23. *NB 65-315/308 AF2ABAQE 97836805. Product Details*. Available at: https://product-selection.grundfos.com/product-detail.product-detail.html?custid=GMO&productnumber=97836805&qcid=1019268753 (accessed on 10 June 2020).
24. *Eurostat Data for the Industrial Consumers in Germany*. Available at: http://ec.europa.eu/eurostat/statistics-explained/index.php/Electricity_price_statistics#Electricity_prices_for_industrial_consumers (accessed on 11 June 2020).
25. *Pump Life Cycle Costs: A Guide to LCC Analysis for Pumping Systems. Executive Summary*. Hydraulic Institute (Parsippany, NJ); Europump (Brussels, Belgium); Office of Industrial Technologies Energy Efficiency and Renewable Energy U.S. Department of Energy (Washington, DC). January 2001, pp. 1–19. Available at: https://www.energy.gov/sites/prod/files/2014/05/f16/pumplcc_1001.pdf.
26. Waghmode L.Y., Sahasrabudhe A.D. A comparative study of life cycle cost analysis of pumps. *In Proceedings of the International Design Engineering Technical Conferences and Computers and Information in Engineering Conference (ASME 2010)*, Montreal, QC, Canada, 15-18 August 2010, vol. 6, pp. 491-500. doi: https://doi.org/10.1115/DETC2010-28034.
27. *AC Electric Motor*. Available at: https://www.acelectricmotor.co.uk/ (accessed on 11 June 2020).

Received 04.10.2020
Accepted 10.12.2020
Published 25.02.2021

V.V. Goman[1], *Ph.D.*,
V.A. Prakht[2], *Ph.D.*,
V.M. Kazakbaev[2], *Ph.D.*,
V.A. Dmitrievskii[2], *Ph.D.*,
E.A. Valeev[1], *Student*,
A.S. Paramonov[2], *Student*,
[1] Nizhny Tagil Technological Institute (branch)
of Ural Federal University,
59, Krasnogvardeiskaia Str., Nizhny Tagil,
Sverdlovsk Region, 622013, Russia,
e-mail: v.v.goman@urfu.ru, valieievewot@mail.ru
[2] Ural Federal University,
19, Mira Str., Ekaterinburg, 620002, Russia,
e-mail: va.prakht@urfu.ru, vadim.kazakbaev@urfu.ru,
vladimir.dmitrievsky@urfu.ru, paramonov.aleksey@inbox.ru

How to cite this article:
Goman V.V., Prakht V.A., Kazakbaev V.M., Dmitrievskii V.A., Valeev E.A., Paramonov A.S. Analysis of the payback period of a modernized pump unit with induction electric motors of advanced energy efficiency classes. *Electrical Engineering & Electromechanics*, 2021, no. 1, pp. 15-19. **doi: 10.20998/2074-272X.2021.1.03.**

UDC 62-503.55 **doi: 10.20998/2074-272X.2021.1.04**

V.A. Lebedev

ON THE SOLUTION OF THE PROBLEM OF SYNTHESIS OF THE CONTROL SYSTEM FOR THE PROCESS OF DOSED FEED OF ELECTRODE WIRE FOR ARC WELDING EQUIPMENT

Goal. *Refinement of the methodology for the development of an effective control system for an electric drive with controlled relay-type regulators for organizing a metered feed of an electrode wire using the parameters of the arc process with the possibility of using it in design practice and practice of technological application.* ***Methodology.*** *The proposed method for the mathematical description (mathematical model) of the system of the developed structure electric drive - arc process with current feedback of welding with a variable structure device is based on the theory of automatic control as applied to nonlinear elements, the application of the theory of operational calculus. At the same time, a selection and description of a nonlinear node in the feedback circuit in the form of a relay element with a certain structure and subsequent linearization of this element was made. As an electric motor of the electrode wire feeder, a new development of a specialized valve electric motor is used, which is used in the system with a microprocessor controller.* ***Results.*** *Due to the presence of a substantially nonlinear link, the calculation of the valve electric drive system – the arc process can be found on the basis of a system of nonlinear differential equations, which is practically impossible for practical application. In this work, these complications are overcome on the basis of a rational choice of the description of the nonlinear link, its harmonic linearization and obtaining on this basis a mathematical description of the system, from which, using the methodology of operational calculus, the relations necessary for calculating the parameters of the system are determined in analytical form.* ***Originality.*** *The problem of calculating a rather complex problem of mathematical description of the valve electric drive system – a technological link in the form of an arc process with a substantially nonlinear link in the feedback circuit in the work is solved with the effective use of a set of methodological methods, which include as a means of representing individual links, including nonlinear links selected simplifications and solutions of the obtained differential equations using original methods of operational calculus. The proposed method (mathematical model) is tested in two directions – oscillography of a real system, as well as system simulation.* ***Practical significance.*** *Using the developed methods for describing the control system, it is possible to calculate its characteristics and, on their basis, select the parameters for setting the electric drive controller, which allows, without additional experimental research, to obtain the necessary character of the transfer of electrode metal, and, consequently, the quality of the result of the arc process.* References 12, figures 4.

Key words: **welding process, electrode wire, pulse feed, control system, mathematical description, calculation.**

Проаналізовано існуючі системи активного впливу на перенесення електродного металу при управлінні процесом дугового зварювання плавким електродом, в тому числі, і на основі імпульсної подачі електродного дроту. Особливо виділено новий спосіб зварювання – з керованими параметрами руху за рахунок введення в електропривод зворотних зв'язків за параметрами дугового процесу зварювання-наплавлення з дозованою подачею дроту. Розглянуто алгоритм реалізації зварювання з дозованою подачею. Обрано електропривод механізму подачі, який базується на спеціально розробленому швидкодіючому вентильному електродвигуні з комп'ютеризованим регулюванням. Для аналізу і вибору параметрів цієї системи запропоновано розглядати її в комплексі з дуговим процесом із застосуванням методів гармонійної лінеаризації. Бібл. 12, рис. 4.

Ключові слова: **зварювальний процес, електродний дріт, імпульсна подача, система управління, математичний опис, розрахунок.**

Проанализированы существующие системы активного влияния на перенос электродного металла при управлении процессом электродуговой сварки плавящимся электродом, в том числе, и на основе импульсной подачи электродной проволоки. Особо выделен новый способ сварки – с управляемыми параметрами движения за счёт введения в электропривод обратных связей по параметрам дугового процесса свврки-наплавки с дозированной подачей проволоки. Рассмотрен алгоритм реализации сварки с дозированной подачей. Выбран электропривод механизма подачи, который базируется на специально разработанном быстродействующем вентильном электродвигателе с компьютеризованным регулированием. Для анализа и выбора параметров этой системы предложено рассматривать её в комплексе с дуговым процессом с применением методов гармонической линеаризации. Библ. 12, рис. 4.

Ключевые слова: **сварочный процесс, электродная проволока, импульсная подача, система управления, математическое описание, расчёт.**

Introduction. Arc mechanized and automatic welding and consumable electrode surfacing is one of the most common technological processes with a wide range of applications and it is predicted that it will continue to develop in the future, improving in all directions and areas of application. The widespread use of mechanized arc welding using both solid and flux-cored electrode wires determines the search for new technical solutions aimed at improving the process technology, as well as updating the park of mechanized and automatic equipment with new technical capabilities [1].

The main directions in improving the technology of welding and surfacing and the corresponding types of equipment are associated with the use of pulse algorithms for the functioning of automatic and semi-automatic

systems [2]. Recently, the technical and technological improvement of automatic and semi-automatic devices is associated with the development and designing of one of the main systems – an electrode wire feed system with a basic unit – a feed mechanism. The main developments in this direction are associated with the use of a pulse feed of an electrode wire. There are developments of both simple systems with practically no regulation of pulse parameters, and with sufficiently perfect mechanisms, and this is described in detail in [3]. It can be noted that the use of a modern feed mechanism providing pulse motion of the electrode wire allows, with correctly selected parameters, to control the transfer of electrode metal drops, which in turn allows (mainly) [4, 5]:

- to significantly reduce the loss of electrode metal for waste and splashing;
- to change the geometrical dimensions of the weld and weld bead, as well as the heat-affected zone;
- to influence the structure of the weld metal, improving its operational properties (strength, wear resistance, including corrosion, etc.);
- to reduce energy costs for conducting welding and surfacing processes.

Additionally, it should be noted the low value of the inertia of the electric motor.

The improvement of the electrode wire feed system is developed using the achievements of the element base and technical solutions based on them. The latest developments of mechanisms with pulse algorithms of functioning are based on the use of gearless electric drives with brushless valve and stepper motors with microprocessor control of the rotation frequency of their shafts, and, consequently, the movement of the electrode wire with high speed levels. Such systems are constantly being improved in different directions and in different systems of automatic welding and surfacing equipment. One of them develops quite intensively in the electrode wire feed system and is associated with the introduction of feedbacks into the electric drive regulator according to the parameters of the arc process – either current or voltage. This solution made it possible to implement a new type of arc process – welding-surfacing with a dosed feed of the electrode wire [6].

The goal of the work is the refinement of the methodology for the development (synthesis) of an effective control system for an electric drive with controlled relay-type regulators for organizing a dosed feed of electrode wire using the parameters of the arc process with the possibility of using it in design practice and practice of technological application.

Statement of the problem. Figure 1 schematically shows the formation of feedback on the arc process. In this case – by the welding current in the process with short circuits of the arc gap at the moments of switching on and off the drive of the electrode wire feed, depending on the desired (required) results of technological processes of welding and surfacing. Switching times on the graph in Fig. 1 marked with points «*c*» ($I_{w\,\min}$) and «*b*» ($I_{w\,\max}$).

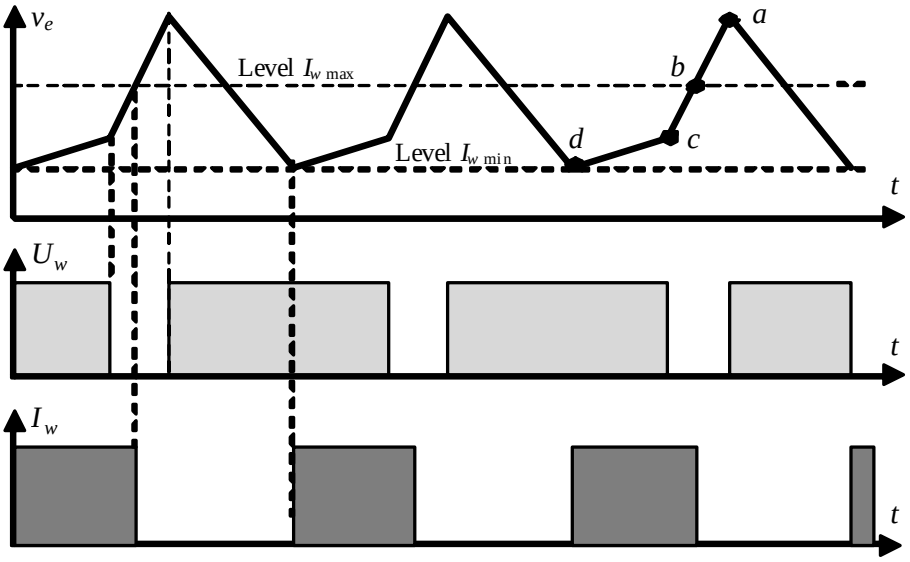

Fig. 1. The operation algorithm of the electrode metal transfer control system associated with the parameters of the arc process current: I_w – welding current; U_w – welding voltage; v_e – feed speed of the electrode wire; *a* – transition of the drop into the bath; *b* – pause in feed rate; *c*, *d* – start of feeding

For synchronization (coincidence) of mechanical pulses (feed pulses) with the frequency of short circuits of the arc gap, information feedback on the parameters of the arc is introduced into the control system so that a pause in the supply always begins after a short circuit.

It should be noted that informational feedback on the arc process current is more effective than voltage feedback due to the fact that arc power sources used in the welding-surfacing process, having, as a rule, rigid external volt-ampere characteristics, are less sensitive to

the voltage of the welding process in the feedback. Conditions may exist where voltage feedback will take priority.

Feedback makes it possible to automatically self-adjust the electric drive of the feed mechanism according to the parameters corresponding to the natural (physical) nature of the welding arc and, which eliminates the time-consuming choice of frequency and duty cycle of mechanical pulses, the parameters of which are very difficult to predetermine.

Figure 2 schematically shows the system of dosed control of the arc welding process with short circuits of the arc gap, including the main links of the system with transmission elements: W_d – valve motor; W_s – arc welding process; W_r – electric drive regulator; W_{nl} – nonlinear link that determines the moments of switching the welding current at the minimum $i_{w\,\min}$ and maximum $i_{w\,\max}$ currents of the welding process.

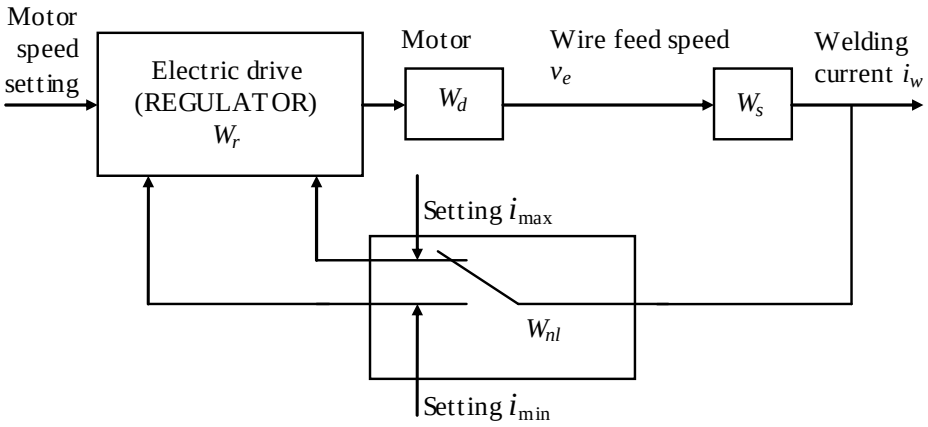

Fig. 2. Block diagram of the control system of the welding process with dosed wire feed with non-linear switching link

The expressions for determining the gear ratios of the links are defined as follows.

It is known that the transfer function of a valve motor in operator form can be identified with the transfer function of a DC motor [7] and written in a somewhat simplified form

$$W_d(p)=\frac{\omega(p)}{U(p)}=\frac{K}{T_m p+1}, \qquad (1)$$

where ω is the shaft rotation frequency; U is the supply voltage; K is the value inversely proportional to the constructive constant of the electric motor; T_m is the electromechanical constant of the phase of the electric motor, taking into account the inertial characteristics of the gearless feed mechanism (rollers).

For the transfer function of the link describing in the operator form the arc welding process with short circuits of the arc gap, an expression is proposed that we obtained in [8].

$$W_{nl}(p)=\frac{i_w(p)}{\omega(p)}\cdot\frac{\frac{E}{R+0{,}5\cdot b}}{T\cdot p^2+p+k}$$

or

$$W_{nl}(p)=\frac{i_w(p)}{\omega(p)}\cdot\frac{S}{T_1^2\cdot p^2+p+k}, \qquad (2)$$

where

$$T=\frac{L}{R+0{,}5\cdot b_1};\quad k=\frac{A\cdot H\cdot E}{R+0{,}5\cdot b_1},$$

in turn L, R are the inductance and equivalent resistance of the welding circuit, respectively; b_1 is the coefficient characterizing the slope of the static characteristics of the arc to the current axis; E is the electric field strength in the arc column;

$$A=\frac{1}{M\cdot\pi\cdot r^2};\quad H=U_i(0{,}285-0{,}0052\cdot U),$$

where U_i is the open circuit voltage of the welding power source; M is the coefficient determining the thermal state of the electrode metal

$$M=C_n\cdot\gamma_n\cdot T_n-C_o\cdot\gamma_o\cdot T_o+r_n\cdot\gamma_o,$$

where C_n, C_o is the heat capacity of the metal at melting and ambient temperatures, respectively; γ_n, γ_o is the density of the metal at melting and ambient temperatures, respectively; r_n is the latent heat of fusion; T_n, T_o are the melting temperature of the electrode metal and the ambient temperature, respectively;

$$S=\frac{E}{R+0{,}5b_1}.$$

Usually, for an electric drive regulator providing additional control qualities (minimum overshoot, minimum possible time for changing the frequency of rotation of the electric motor shaft in transients, etc.), various structures are used, for example, PI regulators, relay current regulators, etc. In our case, to simplify consideration of the dosed control system without prejudice to the essence of the analysis, we take the regulator transfer function in the operator representation in the following form

$$W_p(p)=\frac{U_{sv}(p)}{U(p)}=\frac{K_p}{T_p\cdot p+1}, \qquad (3)$$

where U_{sv} is the supply voltage; K_p is the regulator gain; T_p is the controller time constant.

The description of the transfer function of a nonlinear link providing switching of voltage levels proportional to the current of the welding process presents some difficulties, in particular, because the nonlinearity has an asymmetric nature.

Several options for analyzing such a nonlinear system can be proposed. The simplest and most effective option may be using mathematical modelling. However, such a solution is not always possible for use in design and especially technological practice when choosing the parameters of the nonlinear link in the feedback circuit that determine the characteristics of the transfer of electrode metal drops.

Presentation of the main material. In the system under consideration, by switching, the connections between the elements change depending on its state, therefore, such a system can be fully attributed to a system with a variable structure [9]. The structural diagram of such a system changes during the transient in such a way as to ensure the high-quality performance of control tasks for the welding process by influencing the transfer of electrode metal drops. A serious obstacle to the use of analytical methods and computational tools for the construction of effective control algorithms for modern technical objects, which include arc welding processes, including with doses feed, is a wide range of their characteristics, both in the composition of the system components and in the effects. A promising method in solving problems of describing systems with variable structure can be the use of techniques for analyzing sliding modes. However, the obvious complexity of obtaining analytical expressions for this method of studying a system with a variable structure also cannot be applied both in design and in technological practice.

The two above-mentioned methods of analyzing a system with a nonlinear element are quite accurate, but obviously difficult for application. It is necessary to consider approximate methods of obtaining the mathematical description of nonlinear links [10, 11]. A number of these methods are discussed in the monograph [12]. It seems to us that the harmonic balance method will be the most acceptable for the considered control system.

Figure 3 in a formalized form shows a nonlinear asymmetric relay element corresponding to the W_{nl} link in Fig. 2.

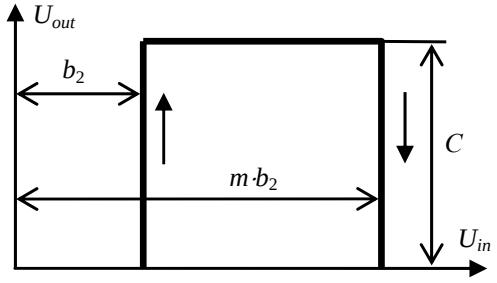

Fig. 3. Formalized representation of a relay asymmetric link (designation in the text)

Obviously, nonlinearity is ambiguous, which should be reflected in the transfer function of the nonlinear link.

The transfer function of the nonlinear link in Fig. 3 consists of an equivalent complex transfer coefficient, which includes a constant component F^0 and harmonic linearization coefficients q and q'

$$W_{nl} = F^0(A, x^0) + q(A, x^0) + q'(A), \quad (4)$$

where F^0 is the constant component; A, x^0 are the amplitude and displacement of the center of oscillations, which, according to [10], can be defined as

$$F^0(A, x^0) = \frac{c}{2} - \frac{c}{2\pi}\left(\arcsin\frac{b_2 - x^0}{A} + \arcsin\frac{m \cdot b_2 - x^0}{A}\right);$$

At

$$A \geq \left| b_2 - x^0 \right|, \quad A \geq \left| x^0 - m \cdot b_2 \right|, \quad (5)$$

where c, b, m are the maximum value of the relay pulse; the period in which the pulse is switched off; the part of the period at which the pulse turns on, respectively

$$q(A, x^0) = \frac{c}{\pi A}\left[\sqrt{1 - \frac{(b_2 - x^0)^2}{A^2}} + \sqrt{1 - \frac{(m \cdot b_2 - x^0)^2}{A^2}}\right], \quad (6)$$

at

$$A \geq \left| b_2 - x^0 \right|, \quad A \geq \left| x^0 - m \cdot b_2 \right|,$$

$$q'(A) = -\frac{c \cdot b_2}{\pi \cdot A}(1 - m),$$

at

$$A \geq \left| b_2 - x^0 \right|, \quad A \geq \left| x^0 - m \cdot b_2 \right|, \quad (7)$$

Taking into account (4)-(7), as well as using simple algebraic transformations, we obtain an approximate linear dependence of the output variable of the nonlinear link on its input variable: with the transfer function

$$W_{nl}(p) = c\{\frac{1}{2} - \frac{1}{2 \cdot \pi}\left(\arcsin\frac{b_2 - x^0}{A} + \arcsin\frac{m \cdot b_2 - x^0}{A}\right) + \\ + \frac{1}{\pi \cdot A}\left[\sqrt{1 - \frac{(b_2 - x^0)^2}{A^2}} + \sqrt{1 - \frac{(m \cdot b_2 - x^0)^2}{A^2}}\right] - \\ - - \frac{b_2 \cdot p}{\pi \cdot \omega \cdot A}(1 - m)\}. \quad (8)$$

Thus, under the influence of harmonic vibrations, the nonlinear link seems to be linearized and can be considered approximately as a linear link. The coefficients q and q' indicated above can be called harmonic gains of the nonlinear link. It can be seen from the formulas for the coefficients that F^0, q and q' depend on the amplitude of the input signal. This dependence reflects the nonlinear properties of the link and because of it, the superposition principle is inapplicable for a harmonically linearized nonlinear link.

The transfer function of the closed-loop control system of the arc welding process with a dosed feed of the

electrode wire can be written as an equation in operator form as follows:

$$\frac{i(p)}{U_{vt}(p)} = \frac{W_p(p)\cdot W_d(p)\cdot W_w(p)}{1+W_p(p)\cdot W_d(p)\cdot W_w(p)\cdot W_{nl}(p)}, \quad (9)$$

where U_{vt} is the setting voltage.

Let us introduce the notation

$$D = c\{\frac{1}{2} - \frac{1}{2\pi}(\arcsin\frac{b_2 - x^0}{A} + \arcsin\frac{mb_2 - x^0}{A}) + \\ + \frac{1}{\pi A}[\sqrt{1-\frac{(b_2 - x^0)^2}{A^2}} + \sqrt{1-\frac{(mb_2 - x^0)^2}{A^2}}]\}; \quad (10)$$

$$N = -\frac{b_2}{\pi\cdot\omega\cdot A}(1-m). \quad (11)$$

Taking into account (1)-(3), (9)-(11), we obtain a complete expression for determining the desired dependence $\frac{i(p)}{U_{vt}(p)}$ in the operator form:

$$\frac{i(p)}{U_{vt}(p)} = \\ = \frac{K_p\cdot K_d\cdot S}{(T_p\cdot p+1)\cdot(T_d\cdot p+1)\cdot(T_1^2\cdot p^2+T_2\cdot p+k)+K_p\cdot K_d\cdot S(D-N\cdot p)} \quad (12)$$

The solution of the operator equation (12) in the form of obtaining the analytical dependence $i = f(U_{vt})$ presents certain difficulties, including because of the high order of p. Such a possibility is presented when using machine research methods and using mathematical modelling.

Modern mathematics does not allow solve equations in general form above the third order by simple methods, so we will look for ways to lower the order of the unknown p whose maximum order is p^4.

Several engineering calculation methods are used to study a linearized link system. First of all, take into account that the time constant of the regulator is very small and the transfer function of the link (3) can be excluded or included in the transfer function with the gain that is taken into account by the link (1). Taking this into account, equation (12) can be rewritten in a simplified form

$$\frac{i(p)}{U_{vt}(p)} = \\ = \frac{K_d\cdot S}{T_d\cdot T_1^2\cdot p^3+(T_1^2+T_d\cdot T_2)\cdot p^2+(T_d\cdot k+T_2)\cdot p+k+K_d\cdot S(D-N\cdot p)}. \quad (13)$$

We will study the linearized equation (13) using one of the engineering methods – the frequency method of E.P. Popov.

From expression (13) we determine the characteristic equation

$$T_d\cdot T_1^2\cdot p^3+(T_1^2+T_d\cdot T_2)\cdot p^2+ \\ +(T_d\cdot k+T_2)\cdot p+k+K_d\cdot S(D-N\cdot p)=0. \quad (14)$$

Let us divide equation (14) into the real and imaginary parts by substituting $p = j\cdot\omega$ as shown below

$$(k+K_d\cdot S\cdot D-(T_1^2+T_d\cdot T_2)\cdot\omega^2=0; \quad (15)$$

$$(T_d\cdot k+T_2+K_d\cdot S\cdot N)\cdot\omega+k-T_d\cdot T_1^2\cdot\omega^2=0. \quad (16)$$

The frequency of the periodic process ω is determined by solving the quadratic equation (16). The discriminant of equation (16)

$$(T_d\cdot k+T_2+K_d\cdot S\cdot N)^2-4\cdot T_d\cdot T_1^2\cdot k=0. \quad (17)$$

An important conclusion follows from expression (17) that self-oscillations with frequency ω can take place under the condition

$$(T_d\cdot k+T_2+K_d\cdot S\cdot N)^2\geq 4\cdot T_d\cdot T_1^2\cdot k. \quad (18)$$

Having determined the frequency ω from equation (15) and substituted it into equation (15), one can also determine the amplitude of self-oscillations.

Since, among other things, the frequency and amplitude of self-oscillations are determined by the values of b_2 and $m\cdot b_2$, which practically corresponds to the minimum $i_{w\,\min}$ and the maximum $i_{w\,\max}$ values of the current of the arc process, which in turn determines the nature of the transfer of the electrode metal, which determines the results of welding with the use of a dosed feed of the electrode wire.

Checking the obtained results. The evaluation and reliability of the results obtained were carried out by comparing the oscillograms of the arc process current with the results obtained in mathematical modelling with the same initial data.

Figure 4 shows several options for presenting currents and voltages for mechanized electric arc welding in a protective gas environment when feeding the electrode wire in the usual way (Fig. 4,*a*) and using the algorithms for dosed feed (Fig. 4,*b*).

Comparison of real oscillograms of current and voltage with data obtained by computer simulation using the MATLAB (Simulink) environment (Fig. 4,*c*) indicate a fairly close result in frequency of the transfer of electrode metal.

A coincidence was obtained within 10-15 % and this is an acceptable result for the technologies of mechanized and automatic welding processes – surfacing with pulse algorithms for feeding the electrode wire and confirming the efficiency of the proposed method.

The proposed method for calculating the operating parameters of an electric drive in the system of technical implementation of the welding and surfacing method with a dosed feed of the electrode wire based on the introduction of an adjustable feedback on the arc process current has a very important practical application and makes it possible to determine the combination of the minimum $i_{w\,\min}$ and maximum $i_{w\,\max}$ values of the welding process current which determine the frequency and amplitude of the arc current pulses and, as a result, the controlled frequency of transfer of the electrode metal drops and thereby provide the quality indicators of the resulting welds and deposited layers (spattering, heat input, formation, penetration, electricity consumption, etc.). Experimentally, it is rather difficult to select the parameters of the feedback settings, since in practice various types and diameters of the electrode wire are used, different process modes are used, etc.

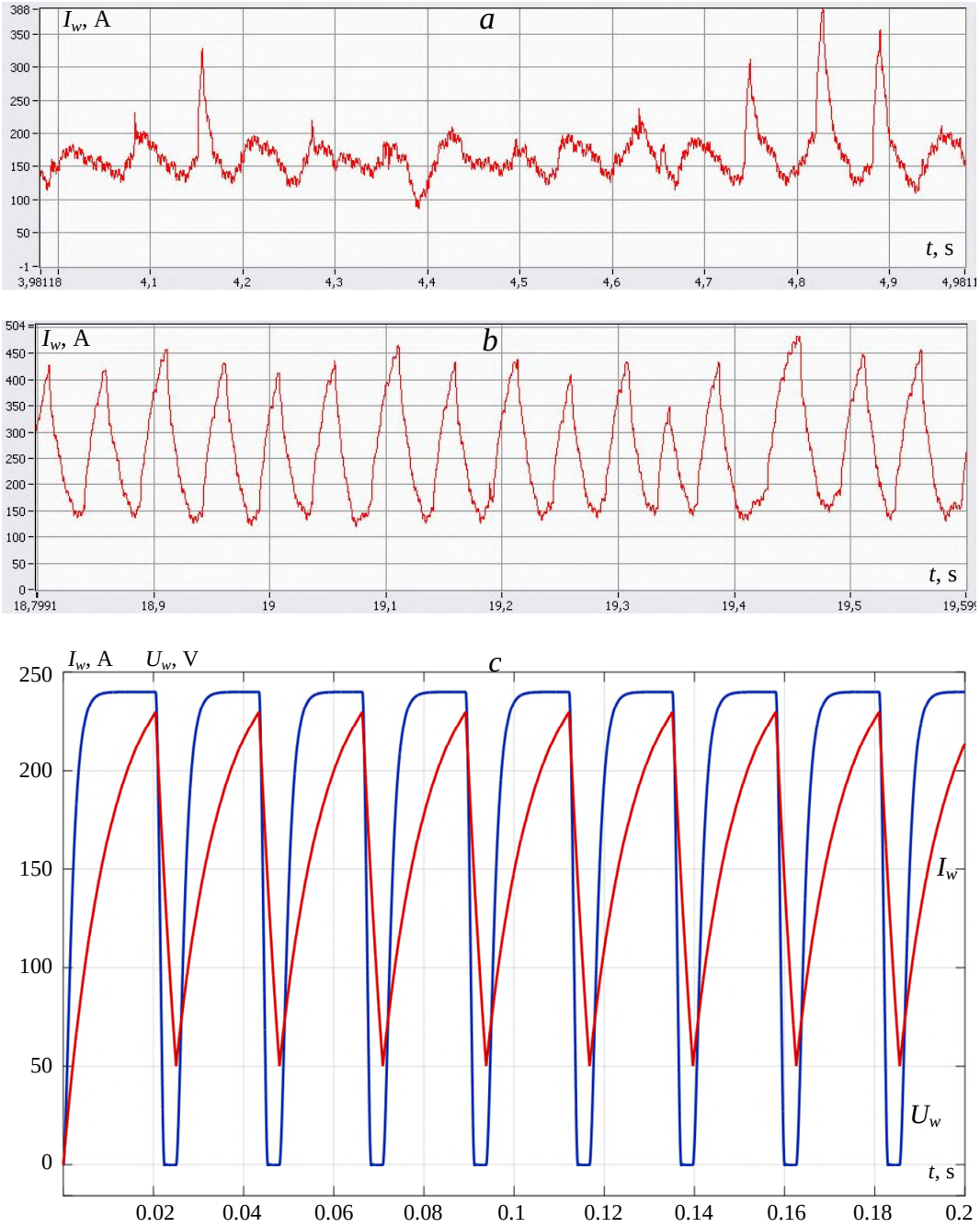

Fig. 4. Comparative results of the study of the arc welding and surfacing process: *a* – current of the conventional process; *b* – current of the process with dosed electrode wire feed; *c* – modelling of the welding process (qualitative representation)

Conclusions.

1. The control system for the arc welding process with a dosed pulse feed of the electrode wire, which includes a mathematical representation of the welding process, contains a substantially nonlinear link in the arc process current feedback loop, which can be linearized to study the system. In this case, for the problems of choosing the parameters for controlling the transfer of electrode metal, the method of harmonic linearization is most applicable, in which a nonlinear element can be represented by an asymmetric relay link.

2. The study of the developed control system can most expediently be carried out using the methods of operational calculus, the use of which makes it possible to obtain results applicable in design and technological practice, and determining the results of the arc process.

3. Verification of the applied research methods of the developed control system of the welding process with the use of a dosed feed of the electrode wire carried out using computer simulation and obtaining characteristic oscillograms confirms the adequacy of the selected research methods.

Conflicts of interests. The authors declare no conflict of interest.

REFERENCES

1. Paton B.E. Welding problems at the turn of the century. *Automatic welding*, 1999, no. 1, pp. 4-14. (Rus).

2. Harris I. Transfer of heat and mass to the base metal in gas metal arc welding. *Welding, Brazing, and Soldering*, 2011, vol. 6, pp. 82-88.
3. Paton B.E., Lebedev V.A., Pichak V.G., Poloskov S.Yu. The evolution of pulsed wire feed systems for welding and surfacing. *Welding and Diagnostics*, 2009, no. 3, pp. 46-51. (Rus).
4. Zhao Y., Lee P.-S., Chung H. Effect of pulsing parameters on drop transfer dynamics and heat transfer behavior in pulsed gas metal arc welding. *International Journal of Heat and Mass Transfer*, 2019, vol. 129, pp. 1110-1122. doi: https://doi.org/10.1016/j.ijheatmasstransfer.2018.10.037.
5. Nadzam J. Tandem GMAW: The Flexibility of Pulsed Spray Transfer. *Welding Innovation*, 2002, vol. 19, no. 2, pp. 18-21.
6. Lebedev V.A., Zhuk G.V. Transferal control of electrode metal on the basis of pulsed-type algorithms of system operation with dosing activity of continuous electrode by mechanized arc welding. *Heavy Engineering*, 2017, no. 6, pp. 27-32. (Rus).
7. Lebedev V.A., Guly M.V. The high-speed valve electric drive for the equipment of the mechanized arc welding. *Mechatronics, automation, control*, 2014, no. 6. pp. 47-51. (Rus).
8. Lebedev V.A. *Povyshenie effektivnosti svarochnogo oborudovaniia na osnove issledovaniia impul'snykh vozdeistvii v sisteme podachi elektrodnoi provoloki*. Diss. dokt. techn. nauk [Increasing the efficiency of welding equipment based on the study of impulse effects in the electrode wire feed system. Doc. tech. sci. diss.]. Kyiv, 2010. (Rus).
9. Emelyanov S.V. *Teoriya sistem s peremennoj strukturoj* [Theory of systems with variable structure]. Moscow, Science Publ. House, 1970. 592 p. (Rus).
10. Abu-Khalaf M., Huang J., Lewis F.L. *Nonlinear H2/H-Infinity Constrained Feedback*. Control Springler, 2006. 203 p.
11. Agachi P.S., Cristea M.V., Csavdari A.A., Szilagyi B. *Advanced process engineering control*. Walter de Gruyter GmbH, Berlin, Germany, 2017. 412 p.
12. Besekersky V.A., Popov E.P. *Teoriya sistem avtomaticheskogo regulirovaniya* [Theory of automatic control systems]. Moscow, Science Publ. House, 1975. 768 p. (Rus).

Received 04.09.2020
Accepted 10.11.2020
Published 25.02.2021

V.A. Lebedev, Doctor of Technical Science, Professor,
SF «Experimental Design-Technological Office
of the E.O. Paton Electric Welding Institute
of the National Academy of Sciences of Ukraine»,
7, Bogenko Str., Kiev, 03150, Ukraine,
e-mail: valpaton@ukr.net

How to cite this article:
Lebedev V.A. On the solution of the problem of synthesis of the control system for the process of dosed feed of electrode wire for arc welding equipment. *Electrical Engineering & Electromechanics*, 2021, no. 1, pp. 20-26. **doi: 10.20998/2074-272X.2021.1.04.**

UDC 621.314 **doi: 10.20998/2074-272X.2021.1.05**

F. Slama, H. Radjeai, S. Mouassa, A. Chouder

NEW ALGORITHM FOR ENERGY DISPATCH SCHEDULING OF GRID-CONNECTED SOLAR PHOTOVOLTAIC SYSTEM WITH BATTERY STORAGE SYSTEM

Purpose. *In last decade the problem of energy management system (EMS) for electric network has received special attention from academic researchers and electricity companies. In this paper, a new algorithm for EMS of a photovoltaic (PV) grid connected system, combined to an storage system is proposed for reducing the character of intermittence of PVs power which infect the stability of electric grid. In simulation model, the PV system and the energy storage system are connected to the same DC bus, whereas EMS controls the power flow from the PV generator to the grid based on the predetermined level of PV power. In the case where the PV power is less than the predefined threshold, energy is stored in the batteries banc which will be employed in the peak energy demand (PED) times. Otherwise, it continues to feed the principal grid. The* ***novelty*** *of the proposed work lies in a new algorithm (smart algorithm) able to determine the most suitable (optimal) hours to switching between battery, Solar PVs, and principal grid based on historical consumption data and also determine the optimal amount of storage energy that be injected during the peak demand.* ***Methods****. The solution of the problem was implemented in the Matlab R2010a Platform and the simulation conducted on Laptop with a 2.5 GHz processor and 4 GB RAM.* ***Results****. Simulation results show that the proposed model schedules the time ON/OFF of the switch in the most optimal way, resulting in absolute control of power electric path, i.e. precise adaptation at the peak without compromising consumers comfort. In addition, other useful results can be directly obtained from the developed scheme. Thus, the results confirm the superiority of the proposed strategy compared to other improved techniques.* References 14, tables 1, figures 12.

Key words: **PV generator and maximum power point tracker (MPPT), inverter, battery storage, management and control strategies, injection of energy.**

Мета. *В останнє десятиліття проблемі системи енергоменеджменту (СЕМ) для електричної мережі приділялася особлива увага з боку науковців та електроенергетичних компаній. У цій роботі пропонується новий алгоритм для СЕМ фотоелектричної (ФЕ) системи, підключеної до мережі, об'єднаної з системою накопичення енергії для зменшення характеру переривчастості потужності ФЕ системи, що впливає на стабільність електричної мережі. У розрахунковій моделі ФЕ система та система накопичення енергії підключені до однієї і тієї ж шини постійного струму, тоді як СЕМ керує потоком потужності від ФЕ генератора до мережі на основі заздалегідь визначеного рівня потужності ФЕ. У тому випадку, коли потужність ФЕ менше заздалегідь визначеного порогу, енергія накопичується в батареях акумуляторів, що буде використано в часи пікового попиту на енергію. В іншому випадку ФЕ продовжує живити основну мережу.* ***Новизна*** *запропонованої роботи полягає в новому алгоритмі (розумному алгоритмі), здатному визначити найбільш підходящі (оптимальні) години для перемикання між акумулятором, сонячними ФЕ та основною мережею на основі даних про історію споживання, а також визначити оптимальну величину енергії накопичення, що вводиться під час пікового попиту.* ***Методи***. *Розв'язання задачі було реалізовано на платформі Matlab R2010a, а моделювання проведено на ноутбуці з процесором 2,5 ГГц та 4 ГБ оперативної пам'яті.* ***Результати***. *Результати моделювання показують, що запропонована модель найоптимальніше планує час увімкнення/вимкнення вимикача, що призводить до абсолютного контролю потужності шляху електроенергії, тобто точної адаптації на піку без шкоди для комфорту споживачів. Крім того, з розробленої схеми можна безпосередньо отримати інші корисні результати. Таким чином, результати підтверджують перевагу запропонованої стратегії порівняно з іншими вдосконаленими методами.* Бібл. 14, табл. 1, рис. 12.

Ключові слова: **фотоелектричний генератор та трекер точки максимальної потужності, інвертор, акумулятор, стратегії управління та контролю, впорскування енергії.**

Introduction. The photovoltaic (PV) technology has the reliability to become potentially one of the most important renewable energy sources for future electricity supply, Also under the implementing effective and efficient policies that attract sufficient investments to deploy renewable energy sources [1]. Also, the PV generators are environmentally friendly as that don't contribute air, water or greenhouse gas pollution [2].

The large-scale installation of photovoltaic distributed generators (PV-DG) connected on the low voltage grid; it requires more attention due to its impact on the electric grid. Because, high integration bring some negative impact on the system such as reverse power flow, voltage rise, transformer and cable rating, voltage unbalance and increase power losses [3].

A previous study also proved that the main factors for integrating renewable energy sources (RES) such as solar energy into the modern electricity grid are climate change [4], and due to the intermittent nature of solar energy, Therefore there is a difficulty in accurately predicting the power product by the PV-DG, then is injected to the grid.

A wide range of solution measures have been suggested in several literary works to reduce problems arising from by large scale PV integration into power grids [5]. In a paper [6], the author explains the accelerated energy transition using new datasets renewable energy data. Technological advancements in control and communication schemes lead to the modernity of the smart grid, and the role of the smart grid and the development of communication between devices and data analytics are very important in the effective and successful implementation of the proposed solutions.

It is recognized that the burden of voltage regulation falls in the PV producers, this requires the use of a smart grid that relies on Smart Meters to acquire and monitor the electrical signal characteristics signal during the day [7]. The suggested solutions to reduce voltage deviations problem is to constrain the PV generation during the

lower energy demand. However, this solution it's not an appropriate ones, because leading to lost revenue to the producer resulting in limitation into increasing PV penetration. To avoid such solution, it is required of the PV producer using the storage system [8] in an effort to prevent leakage of this energy [9]. The authors in [10] present a study about a PV-battery energy storage system installed in a grid-connected residential house wherein daily experimental results shown that the presence of energy storage system has positive effect by reducing the peak energy demand (PED) in midday feed-in of excess PV power, thus providing benefits to the distribution network in terms of reduced peak load and voltage swings.

In view of aforementioned researches, we can see that almost of them rely on a permanent and accurate communication protocol and these clashes with the reality and capabilities of some rural families or poor countries as they using an unreliable communication network. This makes it difficult to implement the solution with the extreme precision suggested by previous authors. So an alternative solution was proposed in this paper, as the process of communication protocol for data entry has been facilitated, and it helps to expand the presence of photovoltaic energy within the energy system in rural areas and developing countries in particular.

This paper **aims** to present more discussions to create different models having ability to adapt with the conditions and possibilities available. The methodology consists of finding the optimal way to limit to feed the grid by the intermittent energy and to mitigate the impact of intermittence of PV power. In addition, the proposed algorithm is used to adjust the energy value which fed the grid by constant value within period's time despite constant changes in the atmosphere. For this purpose, the PV system and the energy storage system are connected to the same DC bus Fig. 1.

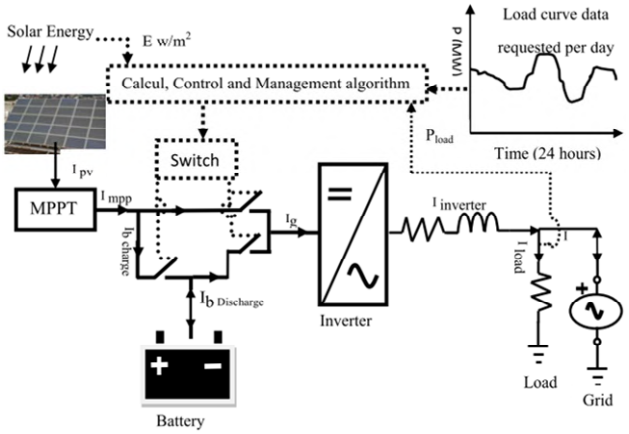

Fig. 1. Schematic of the system model illustrating the main components and energy

Among these positives, it also reduces the possible scenarios of grid-connected photovoltaic with storage-battery of home consumption as a fixed PV matrix size of 3 kWp. In the case where the PV power is less than the predefined threshold value, the energy is stored in the batteries bank, which will be used during PED hours. In the other case, it continues to feed the main grid. It is worth to mention that in this work, we are not interested in studying the capacity of battery storage; detailed study of battery storage are can be obtained in [11].

Modeling and simulation of the system and developed algorithm.

Photovoltaic module modeling system. Numerous models have been developed in the literature for describing the behavior of solar cells; a special attention has been focused on the single-diode model. Basically, the PV cell is a p-n junction semi-conductor which directly converts light energy into electricity. Its equivalent circuit is presented in Fig. 2 [12], in which indicated: I_{ph} is the generated photo-current; V_D is the voltage of diode VD; R_{sh} is the shunt resistance which usually very large can be neglected; R_s is the series resistance of the PV module; I_{cel} and V_{cel} are respectively current and voltage of cell.

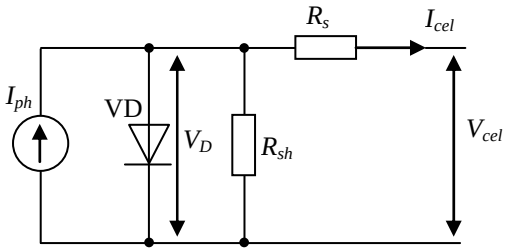

Fig. 2. Equivalent PV cell circuit

In order to extract maximum energy from the photoelectric cell shown in Fig. 2 and to get shape of the injected current into the grid, it's necessary to calculus the coordinates of the maximal power point (V_{mpp}, I_{mpp}). Mathematically it can be defined by the following equations [13]:

$$I_{mpp} = N_p \cdot \left(I_{mr} \cdot \frac{E}{E_n} + K_t \left(T_c - T_n \right) \right); \quad (1)$$

$$V_{mpp} = N_s \cdot \left(V_t \cdot \ln\left(1 + \frac{I_{sc} - I_{mpp}}{I_{sc}} \cdot \left(\exp\left(\frac{V_{oc}}{V_t} \right) - 1 \right) \right) - R_s I_{mpp} \right), \quad (2)$$

where N_p is the parallel cell number; N_s is the series cell number; I_{mr} is the reference short circuit current; E is the irradiation (W/m²); E_n is the normalized insolation; K_t is the temperature coefficient of cell short circuit current I_{sc}; T_c is the cell temperature; T_n is the normalized temperature; R_s is the series resistance of the PV module; V_t is the thermal voltage; V_{oc} is the open-circuit voltage:

$$V_t = \frac{K \cdot B \cdot T_c}{q}; \quad (3)$$

$$V_{oc} = \frac{B \cdot K}{q} \cdot \ln\left(\frac{I_{sc}}{I_0} + 1 \right); \quad (4)$$

$$I_0 = I_{0r} \cdot \left(\frac{T_c}{T_n} \right)^3 \cdot \exp\left(\frac{q \cdot E_g}{B \cdot K} \cdot \left(\frac{1}{T_n} - \frac{1}{T_c} \right) \right), \quad (5)$$

where K is the Boltzmann's constant; B is the diode quality factor; q is the charge of an electron; I_0 is the saturation current of diode are given by [12]; I_{0r} is the reverse saturation current; E_g – energy band gap.

To assess the behavior and simulation of the proposed system we have utilized the real data have been

obtained from an acquisition system available in the Renewable Energy Development Center (REDC) in Algeria, as illustrated in the Fig. 3. The data used here are based on the real data of solar insulation and temperature of one day for both winter season and summer. In our application, module Isofoton 106 Wc is used as PV generator. Table 1 summarizes the manufacturer characteristics of module, in which $V_{\max}$ is the maximum grid voltage; η is the inverter efficiency; L_f, R_{Lf} are the inverter parameters.

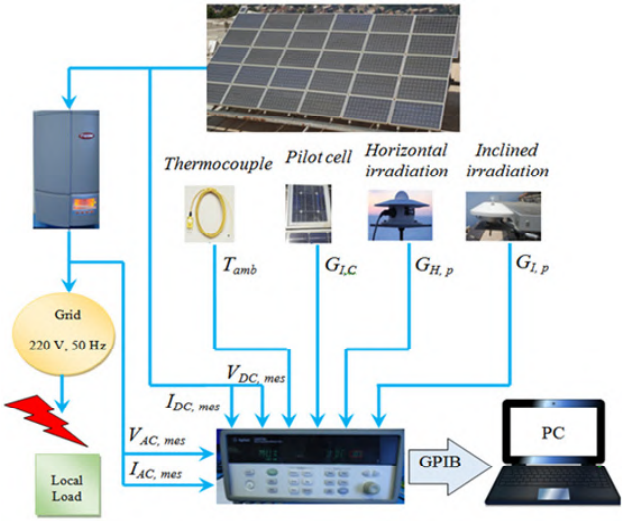

Fig. 3. Synoptic total of the system acquisition (GPIB – general purpose interface bus; T_{amb} – ambient temperature (°C); $G_{H,P}$ – global horizontal irradiation; $G_{I,C}$ and $G_{I,p}$ – inclined irradiation; $V_{DC, mes}$ – DC link voltage measured; $V_{AC, mes}$ – AC voltage measured; $I_{DC, mes}$ – DC link current measured; $I_{AC,mes}$ – AC current measured)

Table 1

Simulation parameters values

Parameters	Values	Parameters	Values
E_n	1000 W/m²	K_t	$2.3{\cdot}10^{-3}$/2 A/°C
T_n	298 K	R_s	0.153·2/36 Ω
I_{sc}	6.69/2 A	K	$1.38.10^{-23}$ J/K
V_{oc}	20.32/36 V	N_s	540
I_{0r}	$1.406{\cdot}10^{-7}$/2 A	N_p	4
I_{mr}	6.03/2 A	L_f	0.02 H
E_g	1.12 eV	R_{Lf}	0.02 Ω
q	$1.602{\cdot}10^{-19}$ C	$V_{\max}$	$220\sqrt{2}$
B	1.3	η	0.95

Inverter modeling. The inverter connected to a grid receives the DC current from PV plant and converting it to AC current to inject in electric grid with unity power factor. A simplification has been introduced to the inverter model. The full bridge DC-AC converter is modeled as current controlled voltage source where the harmonic content is ignored. Fig. 4 shows the schematic diagram of grid connected inverter. The key variable for controlling this operation is the voltage of inverter (V_{inv}). The inverter current (I_g) can be written as

$$I_g = \frac{V_{inv} - V_{ac}}{jL_f\omega}, \qquad (6)$$

where V_{inv} is represent fundamental component of inverter output; V_{ac} is the utility grid waveform; ω defines angular frequency of the voltage vector.

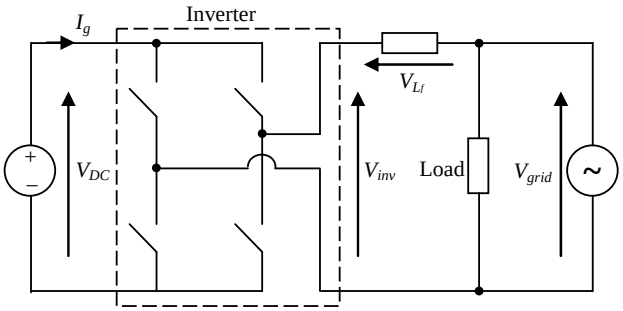

Fig. 4. Grid connected inverter

Simulation of the PV grid inverter.

The implementation of this system in MATLAB platform that the behaviour schematic of PV grid connected inverter is presented in Fig. 5. In this case indirect current control is used for drawing a reference I_g current that must injected to the electric grid is calculated according the power produced from PV generator model and modelled as a controlled current source. The amplitude of current that inverter drawing in from continuous source is deduced by the power balancing principles [13].

$$I_g = \frac{2 \cdot I_m \cdot V_m \cdot \eta}{V_{\max}}, \qquad (7)$$

where I_m and V_m represent the coordinates of the maximal power point.

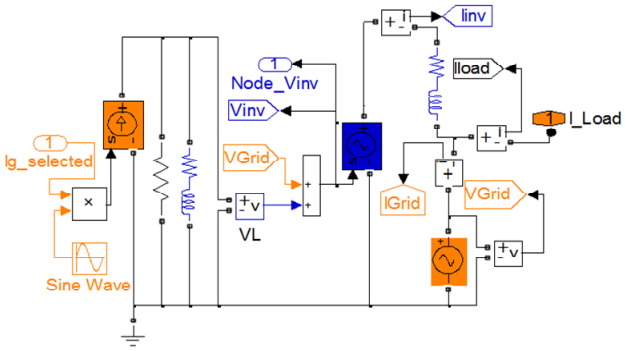

Fig. 5. Matlab schematic of PV grid connected inverter

Proposed algorithm. A major reason for grid data unavailability and transparency shortfall is data accessibility [14]. On the other hand, the input data needed by grid models or so-called grid data and their demands highly variant depending on the type of the grid model used. In this paper we focused only at the Load Curve Data required within day. Fig. 6,*a*,*b* confirms that energy demand has nearly stable during of both monthly and seasonal periods. Thus, in order to fulfilling the gaps of data accessibility, the monthly load curve, which represents the inputs data of algorithm is obtained by using 30 daily load curves. The proposed algorithm can be summarized in a diagram as indicated in Fig. 7.

The work of the algorithm consists of several steps.

The *first step* to determine the time corresponding to the PED, within winter season there is only one peak of energy demand named $T_{\max 2}$, but at season summer, there

is one off-peak hour between 2 on-peak hours demand, named, T_{min3}, T_{max1} and T_{max2} respectively. These peaks are calculated using algorithm shown in Fig. 8.

The *second step* is dedicated to find right time for charging the battery.

The *third step* consists to identify discharging time of battery according to the signal provided by the algorithm.

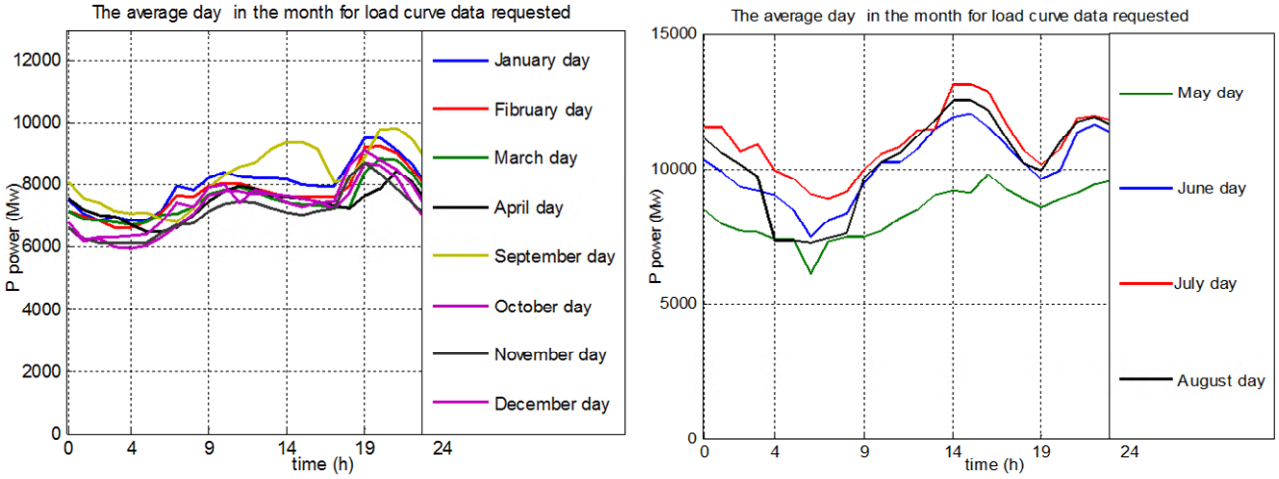

a *b*

Fig. 6. Daily load curve data

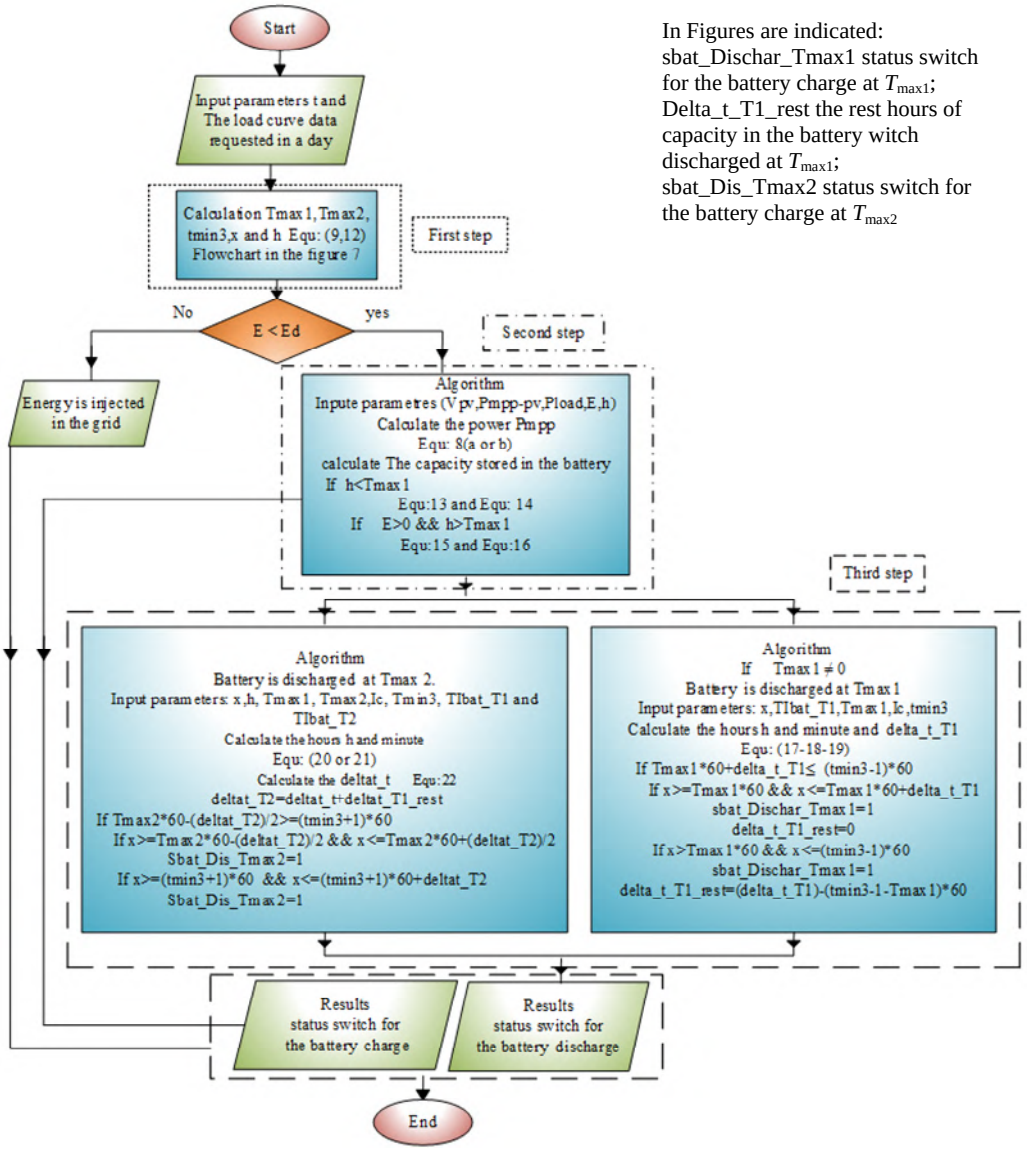

In Figures are indicated: sbat_Dischar_Tmax1 status switch for the battery charge at T_{max1}; Delta_t_T1_rest the rest hours of capacity in the battery witch discharged at T_{max1}; sbat_Dis_Tmax2 status switch for the battery charge at T_{max2}

Fig. 7. Diagram of different stages of the algorithm

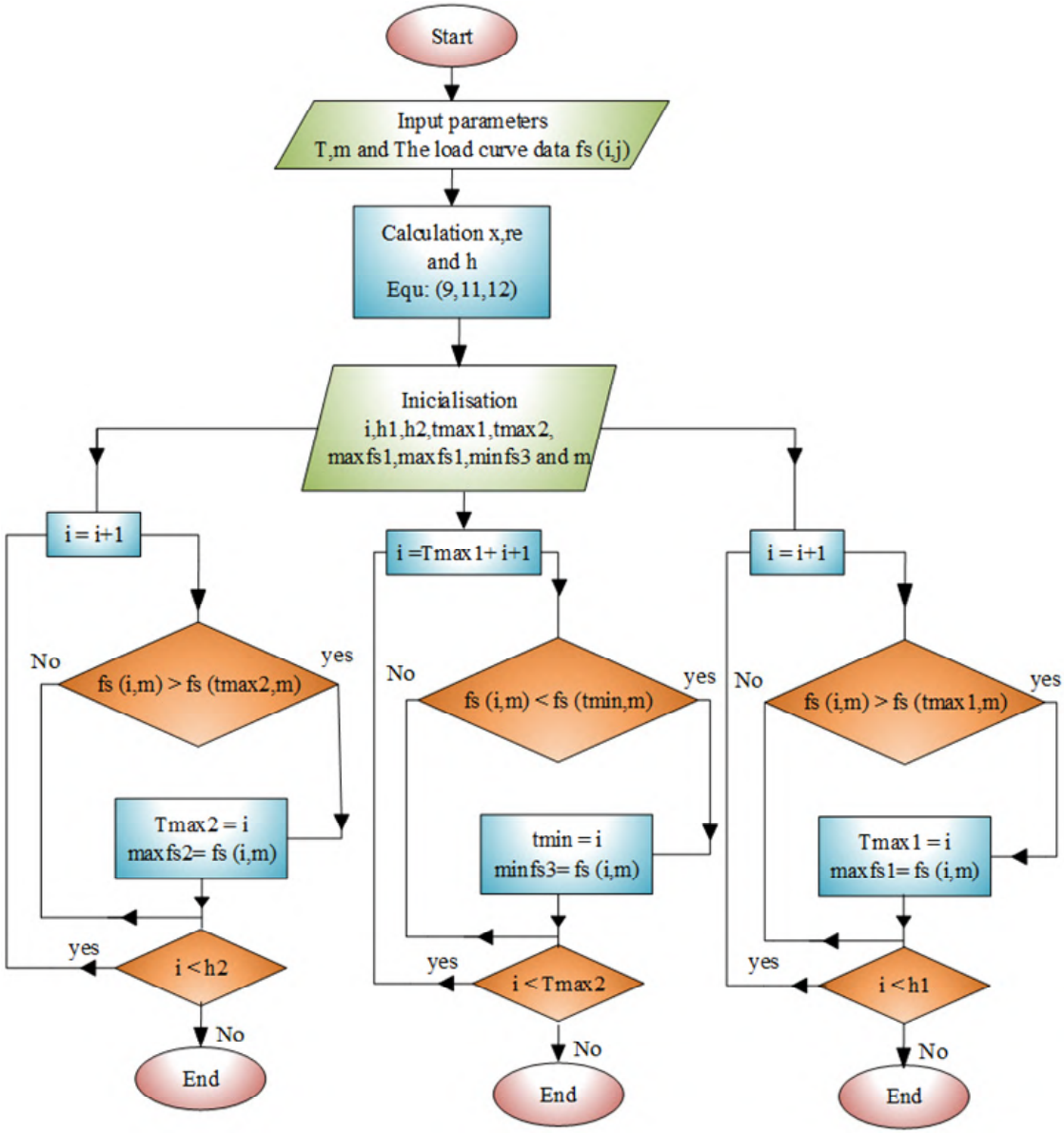

Fig. 8. Algorithm to define the time for T_{max1}, T_{max2} and T_{min3}

Based on the data acquisition system using in Algerian Renewable Energy Development Center (AREDC) can extract a profile of solar radiation during a day, which contains 1440 (24 h × 60 min) values of solar radiation, so that each minute in day represent a value of solar radiation as operation point. in other side, the simulation time required during 1440 operating points is T_{Smax}, in the same way we can determine simulation time in seconds that correspond of one value of solar radiation, (i.e., one operating point corresponding to a real single minute in day); thus, we can identify the real time in minutes X and hours h at any moment of simulation time. To this end, the proposed smart algorithm can easily managing the maximum and minimum peaks of energy, as well as staring time of charging and discharging batteries.

Follow calculate the power that will be stored in the batteries:

$$\begin{aligned} \Delta P &= P_{m\,pp\_pv} - P_{load} \quad \text{if} \quad P_{m\,pp\_pv} > P_{load} \;\; (a); \\ \Delta P &= P_{m\,pp\_pv} \qquad\quad \text{if} \quad P_{m\,pp\_pv} < P_{load} \;\; (b); \end{aligned} \tag{8}$$

$$X = \varepsilon \cdot t, \tag{9}$$

where t is time of simulation; $P_{m\,pp\_pv}$ is the maximum power generated by the PV generator

$$\varepsilon = \frac{X_{\max}}{T_{S\max}}; \tag{10}$$

$$re = rem\,(X, 60), \tag{11}$$

where *rem* indicates of remainder after division; $T_{S\max}$ is the maximum simulation time; $X_{\max}$ is the maximum operating minutes.

$$h = \frac{(X - re)}{60}. \tag{12}$$

Calculate the battery current $I_{battery\_T_1}$

$$I_{battery\_T_1} = \frac{\Delta P}{V_{PV}} \quad \text{if} \quad h < T_{\max 1}. \tag{13}$$

Calculate the total battery current before T_{max1}

$$I_{Ibat\_T_1} = coef \times \sum I_{battery\_T_1}, \text{ A·h.} \tag{14}$$

Calculate the battery current $I_{battery\_T_2}$

$$I_{battery\_T\,2} = \frac{\Delta P}{V_{PV}} \quad \text{if} \quad h > T_{\max 1}. \tag{15}$$

Calculate the total battery current after $T_{\max 1}$

$$I_{Ibat\_T\,2} = coef \cdot \sum I_{battery\_T_2}\ , \text{A·h}. \tag{16}$$

Calculate the hours of capacity in the battery before $T_{\max 1}$ that will be discharged by the value of current I_c

$$\text{hours} = \text{floor}\left|\frac{T_{Ibat\_T1}}{I_c}\right|; \tag{17}$$

$$\text{minute} = \text{floor}\left|\left(\frac{T_{Ibat\_T1}}{I_c} - hours\right)\cdot 60\right|, \tag{18}$$

where term *floor* () denotes the nearest integer less than or equal to hours or minutes.

Calculating Δt_T_1 is the time of battery discharge

$$\Delta t\_T_1 = \text{hours}\cdot 60 + \text{minute}. \tag{19}$$

Calculate the hours of capacity in the battery after $T_{\max 1}$ that will be discharged by the value of current I_c

$$\begin{aligned}
&\text{hours} = \text{floor}\left|\frac{T_{Ibat_T\,2}}{I_c}\right| \quad \text{if} \quad T_{\max 1} \neq 0;\\
&\text{minute} = \text{floor}\left|\left(\frac{T_{Ibat_T\,2}}{I_c} - hour\right)\cdot 60\right| \quad \text{if} \quad T_{\max 1} \neq 0;
\end{aligned} \tag{20}$$

$$\begin{aligned}
&\text{hours} = \text{floor}\left|\frac{T_{Ibat_T1} + T_{Ibat_T\,2}}{I_c}\right| \quad \text{if} \quad T_{\max 1} = 0\\
&\text{minute} = \text{floor}\left|\left(\frac{T_{Ibat_T1} + T_{Ibat_T\,2}}{I_c} - hour\right)\cdot 60\right| \quad \text{if} \quad T_{\max 1} = 0
\end{aligned} \tag{21}$$

Calculating Δt_T_2 is the time of battery discharge

$$\Delta t\_T_2 = \text{hours}\cdot 60 + \text{minute}. \tag{22}$$

Results and discussion.

PED emerges as a phenomenon which epitomizes the relevance of social practices which lead us to our understanding of the dynamics of energy demand is the position that the timing of energy demand is determined. It has been defined of PED times by using the smart algorithm, through the data base as shown in Fig. 4, which represents the energy demand curve for days for months of the year. For example, in January, we find that $T_{\max 2}$ = 19 h, $T_{\min 3}$ = 16 h, and in June we find that $T_{\max 1}$ = 14 h, $T_{\max 2}$ = 22 h and $T_{\min 3}$ = 19 h.

Simulation results for typical days, sunny and cloudy in the summer and winter, respectively. The value I_c which represents the value of current when the battery is discharged is choosed in a proportional to the current I_{pv} produced by the PV generator when the solar radiation E is equal to the threshold E_d, in order to maintain the same size of electrical wires. As for the choice the threshold of solar radiation E_d, it is related to the storage capacity of the batteries, taking into account the cost, but in this study it was an experimental direct choice.

Simulation results by using the data of a day in the summer. Based on the daily load curve data for energy-consumption pattern illustrated in Fig. 6 and the weather conditions, we obtained the results presented in the Fig. 9 and Fig. 11, in which illustrates the different energy flow scenarios produced by the PV generator, over time periods determined and with different quantities, according to the solar radiation profile and the value of the energy stored in the batteries shown in Fig. 10 and Fig. 12.

Simulation results by using the data of a cloudy day in the winter. From Fig. 9 *Period 1* it can be seen that before 06:52 AM, the value of the current I_g is equal to 0, which means that the photovoltaic generator (PVG) does not produce any energy due to the unavailability of sunlight; during this period the local load is totally supplied from public electric network, so $I_g = 0$.

Period 2 within the interval time 06:52 am − 11:00 am, the PVG charges battery by current I_b, and supply the local load by energy, so $I_g = I_{pv} - I_b = I_{load}$.

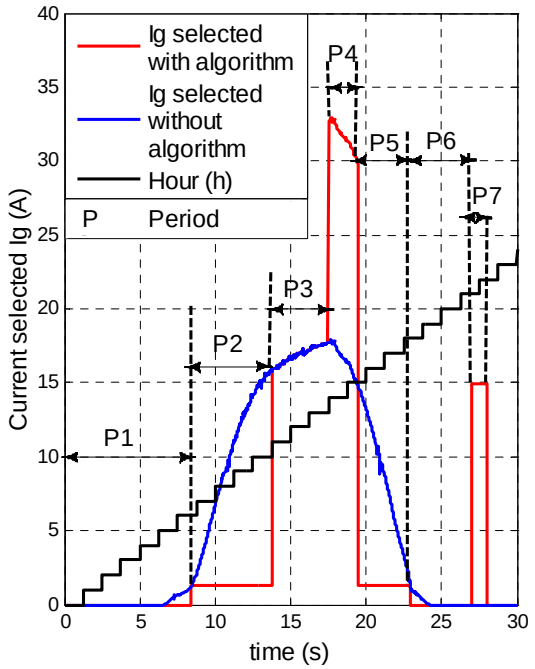

Fig. 9. Simulation shape of injected current I_g

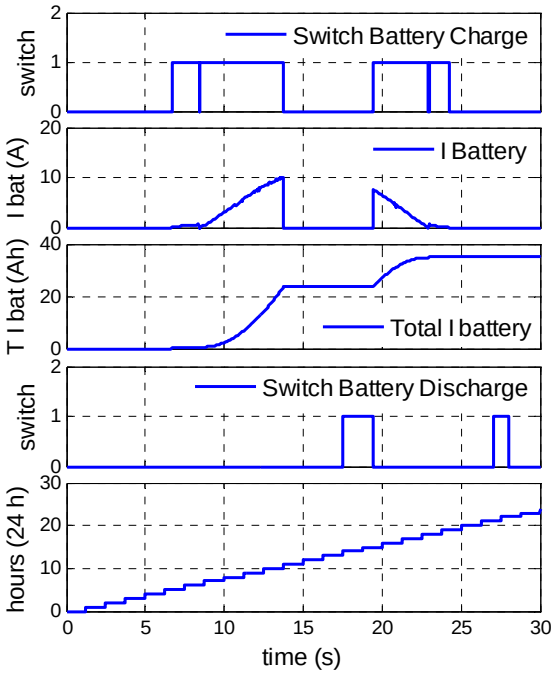

Fig. 10. Switch of control for simulation current of battery

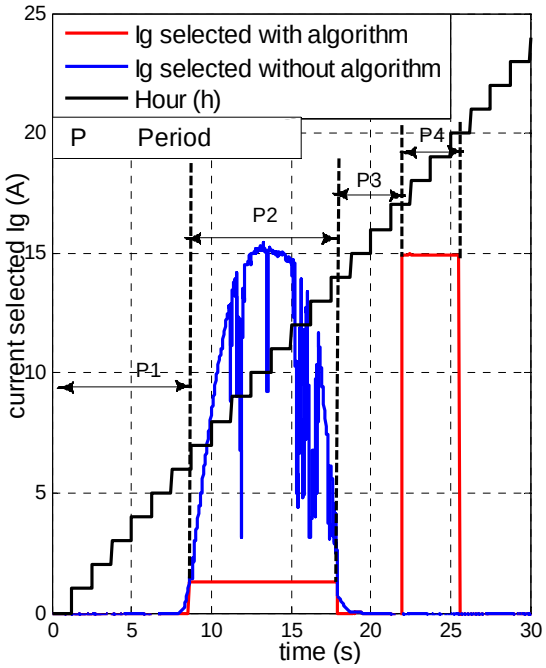

Fig. 11. Simulation shape of injected current I_g

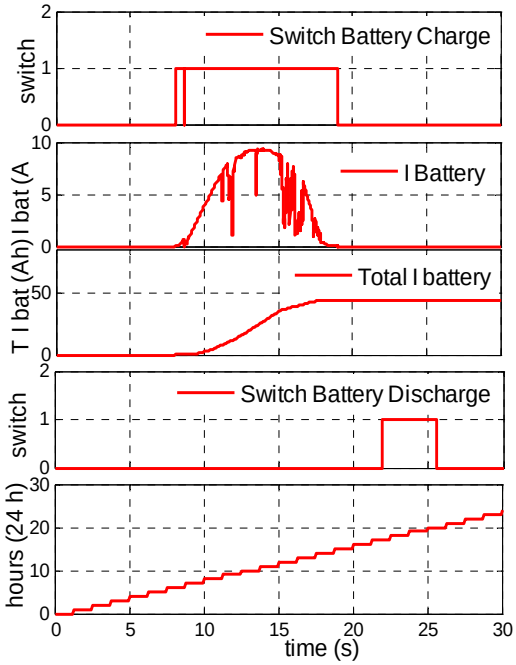

Fig. 12. Switch of control for simulation current of battery

Period 3 during 11:00 AM to 14:00 the local load is covered by PVG and the excess energy is injected into the network, because the solar radiation exceeds his threshold E_d. In addition, herein the battery is focused only to store intermittent energy causing from the weather conditions, or the solar radiation is inferior to his threshold, so $I_g = I_{pv}$.

Period 4 in the time domain of from 14:00 to 15:47, the PVG feeds the local load and contributes with battery to inject energy into the electrical network in coinciding with the time T_{max1}, the conjunction of PV systems with batteries enables as additional increase energy, so $I_g = I_{pv} + I_b$.

Period 5 within the interval time between 15:47 to 18:21, the PVG is charging a battery and the local load feed also, where $I_g = I_{pv} – I_b = I_{load}$.

Period 6 the time interval between 18:21 to 21:13, the PVG doesn't generate electricity, due to the total absence of sunlight, so in this case the local charge is feed from the public network, so $I_g = I_{pv} = 0$.

Period 7 in the last case, between 21:13 to 22:47, the battery are discharged into the public network in conjunction with T_{max2} time, so the current $I_g = I_b$.

Figure 11 shows that over the course of the day, period 2 through 07:00 to 14:15 all the intermittent energy produced by the PVG is stored in the battery without resorting to feeding the grid with this fluctuating energy. In the end, this strategy was able to supply the main grid with energy during the peak, within a specified time interval period 4 between 17:30 to 20:20, which lead to facilitate the monitoring of the network's stability.

Conclusions.

In this paper, a new management scheme based on a system behavioral approach is proposed with a novel power flow management strategy to grid-connected PV system smart scheme, based on the real load curve data.

It is shown that the demand for energy is relatively stable within a month, which allowed us to understand the dynamics of energy demand and we developed a novel strategy to facilitate the communication between the distributor of electricity dispatcher and the producer of energy generated by solar panels, so that the defect existing in this type of generator is corrected.

The proposed strategy describes how to exploit the power produced from PV generator based on determining the solar radiation threshold that is relied upon in specifying the energy path, either directly injected into the network or stored in order to inject later as per schedule given by algorithm.

This study not only allowed us to anticipate and estimate the amount of energy that will be injected into the network, but also to define the appropriate schedule for injection, supplying the network with energy at the peak energy demand times, in avoiding to supply intermittent power into network even under bad weather conditions. On the light of the obtained results, it would be very helpful and facile to control the stability dispatch in power networks. More importantly, the proposed strategy reduces the negativity of the intermittent nature of solar-energy, which encourages widespread investment in solar power generators.

Acknowledgements.

We gratefully acknowledge the support of the Renewable Energy Development Center (www.cder.dz) at Algeria. This work was supported fully by the University of Ferhat Abbas, Setif-1.

Conflict of interests. The authors declare no conflicts of interest.

REFERENCES

1. Polzin F., Egli F., Steffen B., Schmidt T.S. How do policies mobilize private finance for renewable energy? – A systematic review with an investor perspective. *Applied Energy*, 2019, vol. 236, pp. 1249-1268. doi: https://doi.org/10.1016/j.apenergy.2018.11.098.

2. Ivanova D., Barrett J., Wiedenhofer D., Macura B., Callaghan M., Creutzig F. Quantifying the potential for climate

change mitigation of consumption options. *Environmental Research Letters*, 2020, vol. 15, no. 9, p. 093001. doi: https://doi.org/10.1088/1748-9326/ab8589.
3. Kenneth A.P., Folly K. Voltage rise issue with high penetration of grid connected PV. *Conference Paper of 19th World Congress, International Federation of Automatic Control (IFAC, 2014)*, Cape Town, South Africa. August 24-29, 2014, vol. 19, no. 3. doi: 10.13140/2.1.2274.2406.
4. Ascencio-Vásquez J., Brecl K., Topič M. Methodology of Köppen-Geiger-Photovoltaic climate classification and implications to worldwide mapping of PV system performance. *Solar Energy*, 2019, vol. 191, pp. 672-685. doi: https://doi.org/10.1016/j.solener.2019.08.072.
5. Sampath Kumar D., Gandhi O., Rodríguez-Gallegos C.D., Srinivasan D. Review of power system impacts at high PV penetration Part II: Potential solutions and the way forward. *Solar Energy*, 2020, vol. 210, pp. 202-221. doi: https://doi.org/10.1016/j.solener.2020.08.047.
6. Gielen D., Boshell F., Saygin D., Bazilian M.D., Wagner N., Gorini R. The role of renewable energy in the global energy transformation. *Energy Strategy Reviews*, 2019, vol. 24, pp. 38-50. doi: https://doi.org/10.1016/j.esr.2019.01.006.
7. Benabdallah I., Oun A., Cherif A. Grid Connected PV Plant based on Smart Grid Control and Monitoring. *International Journal of Advanced Computer Science and Applications*, 2017, vol. 8, no. 6, pp. 299-306. doi: https://doi.org/10.14569/ijacsa.2017.080639.
8. Guidara I., Souissi A., Chaabene M. Novel configuration and optimum energy flow management of a grid-connected photovoltaic battery installation. *Computers & Electrical Engineering*, 2020, vol. 85, p. 106677. doi: https://doi.org/10.1016/j.compeleceng.2020.106677.
9. Ariyaratna P., Muttaqi K.M., Sutanto D. A novel control strategy to mitigate slow and fast fluctuations of the voltage profile at common coupling Point of rooftop solar PV unit with an integrated hybrid energy storage system. *Journal of Energy Storage*, 2018, vol. 20, pp. 409-417. doi: https://doi.org/10.1016/j.est.2018.10.016.
10. Bagalini V., Zhao B.Y., Wang R.Z., Desideri U. Solar PV-Battery-Electric Grid-Based Energy System for Residential Applications: System Configuration and Viability. *Research*, 2019, vol. 2019, pp. 1-17. doi: https://doi.org/10.34133/2019/3838603.
11. Ru Y., Kleissl J., Martinez S. Exact sizing of battery capacity for photovoltaic systems. *European Journal of Control*, 2014, vol. 20, no. 1, pp. 24-37. doi: https://doi.org/10.1016/j.ejcon.2013.08.002.
12. Vinod, Kumar R., Singh S.K. Solar photovoltaic modeling and simulation: As a renewable energy solution. *Energy Reports*, 2018, vol. 4, pp. 701-712. doi: https://doi.org/10.1016/j.egyr.2018.09.008.
13. Slama F., Chouder A., Radjeai H. Simulation of Photovoltaic generator Connected To a Grid. *Mediterranean Journal of Modeling and Simulation*, 2014, no. 1, pp. 25-33. Available at: https://hal.archives-ouvertes.fr/hal-01293445/document (accessed on 22 June 2020).
14. Medjroubi W., Müller U.P., Scharf M., Matke C., Kleinhans D. Open Data in Power Grid Modelling: New Approaches Towards Transparent Grid Models. *Energy Reports*, 2017, vol. 3, pp. 14-21. doi: https://doi.org/10.1016/j.egyr.2016.12.001.

Received 01.11.2020
Accepted 14.12.2020
Published 25.02.2021

Fateh Slama[1], *Ph.D. Student*,
Hamoud Radjeai[1], *Professor*,
Souhil Mouassa[2], *Doctor of Engineering*,
Aissa Chouder[3], *Professor*,
[1] Department of Electrical Engineering,
Ferhat Abbas University of Setif 1, Algeria,
El Bez Campus, Setif 19000, Algeria,
e-mail: slama.fateh@univ-setif.dz, hradjeai@univ-setif.dz
[2] Department of Electrical Engineering,
University of Jaén,
23700 EPS Linares, Jaén, Spain
e-mail: souhil.mouassa@univ-bouira.dz
[3] Department of Electrical Engineering,
Mohamed Boudiaf University of M'Sila,
PB 166 M'sila 28000, Algeria,
e-mail: aissa.chouder@univ-msila.dz

How to cite this article:
Slama F., Radjeai H., Mouassa S., Chouder A. New algorithm for energy dispatch scheduling of grid-connected solar photovoltaic system with battery storage system. *Electrical Engineering & Electromechanics*, 2021, no. 1, pp. 27-34. **doi: 10.20998/2074-272X.2021.1.05.**

UDC 621.327.7 **doi: 10.20998/2074-272X.2021.1.06**

K.V. Korytchenko, O.V. Shypul, D. Samoilenko, I.S. Varshamova, A.A. Lisniak, S.V. Harbuz, K.M. Ostapov

NUMERICAL SIMULATION OF GAP LENGTH INFLUENCE ON ENERGY DEPOSITION IN SPARK DISCHARGE

*The **aim** of the work is to study the influence of the length of the spark gap on energy input into the discharge channel during its gas-dynamic expansion. **Methodology**. The research is carried out by numerical modeling of the process of spark discharge development at variable values of the discharge gap length and at invariable other discharge conditions. The length of the gap was set in the range from 1 mm to 20 mm. The study was conducted using a numerical model of spark development, which takes into account the processes of nonstationary gas-dynamic expansion of the spark channel, the transient process in the electric circuit, nonequilibrium chemical processes, gas ionization, heat transfer and electrons thermal conductivity. The simulation was performed in atmospheric pressure nitrogen. The calculation was performed for various parameters of the RLC circuit, such as capacitance, inductance, resistance and voltage across the capacitor. **Results.** The study evaluates the influence of the spark length on the discharge current, the resistance of the spark channel, the energy deposited in the spark channel, and the distribution of thermodynamic parameters of the gas during the development of the spark discharge. It is confirmed that increasing the length of the gap increases the resistance of the spark. The deviation from the linear relationship between the deposited energy or the radiated energy and the length of the spark gap is estimated. **Scientific novelty.** A linear relationship between the gap length and the deposited energy is revealed when the total energy is above tens of Joules. Deviations from the linear dependence were detected in the discharge circuit when the total energy is below one of Joules. **Practical value.** The research results allow predicting the effect of the spark gap length on the energy input into the discharge channel under conditions of a slight change in the discharge current. In the conditions of essential change of amplitude of discharge current it is expedient to apply numerical researches for specification of changes in the energy deposited into a spark discharge.* References 31, table 1, figures 13.

Key words: **spark discharge, energy deposition, gap length influence**.

***Метою** роботи є дослідження впливу довжини іскрового проміжку на введення енергії в розрядний канал під час його газодинамічного розширення. **Методика**. Дослідження здійснено шляхом чисельного моделювання процесу розвитку іскрового розряду за відмінних значень довжини розрядного проміжку та за незмінних інших умов розряду. Довжина проміжку задавалась в межах від 1 мм до 20 мм. Дослідження проведено з використанням чисельної моделі розвитку іскри, що враховує процеси нестаціонарного газодинамічного розширення іскрового каналу, перехідний процес в електричному колі, нерівноважні хімічні процесі, іонізацію газу, теплообмін випромінюванням та електронною теплопровідністю. Моделювання здійснювалось у азоті атмосферного тиску. Розрахунок проводився для різних параметрів RLC кола, таких як ємність, індуктивність, опір і напруга на ємності. **Результати**. В результаті дослідження оцінено вплив довжини іскрового на розрядний струм, опір іскрового каналу, енергію, що виділяється в іскровому каналі, та розподіл термодинамічних параметрів газу під час розвитку іскрового розряду. Підтверджено, що збільшення довжини проміжку збільшує опір іскри. Оцінено відхилення від лінійного співвідношення між енергією, що виділяється, або енергією, що випромінюється, та довжиною іскрового проміжку. **Наукова новизна**. У розрядному колі із накопиченою енергією понад десятки джоулів виявлено лінійну залежність між довжиною проміжку та енергією, що виділяється у ньому. У розрядному колі із накопиченою енергією до одного джоуля виявлено відхилення від лінійної залежності. **Практичне значення.** Результати досліджень дозволяють прогнозувати вплив довжини іскрового проміжку на введення енергії в розрядний канал в умовах незначної зміни розрядного струму. В умовах суттєвої зміни амплітуди розрядного струму доцільно застосовувати чисельні дослідження для уточнення змін в енергії, що вводиться в іскровий розряд.* Бібл. 31, табл. 1, рис. 13.

Ключові слова: **іскровий розряд, введення енергії, вплив довжини проміжку.**

Introduction. Spark discharge is used in various devices where the length of the spark gap can vary in a wide range. The variation of the spark gap length results in the change of the spark channel resistance and it affects the discharge current. Finally, a change in the length of the spark gap leads to a change in the energy deposited in the spark discharge.

Resistance of an electrical conductor of a uniform cross section and conductivity is directly proportional to a length of the conductor. Therefore, an increase in the length of the electrical load leads to a linear rise in energy released in the load when a discharge current is the same. If the resistance of the discharge circuit significantly exceeds the resistance of the load, a change in the length of the load practically does not affect the discharge current. Thus, in a first approximation, there is a linear relationship between the load length and the energy released in the load when the mentioned conditions take place. But the spark channel is an electrical conductor in which the cross section and conductivity change during the expansion of the spark channel. The discharge current determines the process of the spark channel expansion and, accordingly, affects the distribution of gas conductivity over the cross section of the spark channel. At the same time, the development of the discharge current depends on the resistance of the spark channel. As a result, the energy deposited into the spark channel deviates from a linear dependence on the spark gap length.

The study of the influence of the gap length on the deposited energy is important from a practical point of view. This is because spark energy affects the reliability of combustible mixtures ignition [1]. The energy of a spark discharge affects the detonation initiation process in

a detonation devises such as a pulse detonation engine and a pulse compression detonation gun [2-4]. The energy deposited into the spark channel has an impact on the period of the recovery of the dielectric strength of spark switches [5]. In nanoparticle generators, a change in the length of the discharge gap leads to a redistribution of the energy balance between the energy deposited in a gas-discharge channel and the energy loss at near-electrode regions [6]. This redistribution influences the efficiency of nanoparticle generation. The energy balance in the spark discharge also affects the energy efficiency of electrical discharge machining [7].

The energy deposition in a spark discharge with varied gap lengths was investigated experimentally in the work [8]. The authors measured the voltage across the spark gap with varied gap lengths to extract a voltage drop across the gas-discharge channel and a sum of cathode and anode voltage drops. So, it was assumed the voltage drop across the gas-discharge channel is directly proportional to the length of the spark gap. And the sum of cathode and anode voltage drops and electric field strength in the gas-discharge channel depend on a discharge time only. The voltage across the spark gap with varied gap lengths was measured at the different discharge time. Then the voltages were compared at the same discharge time to extract the voltage drop across the gas-discharge channel and the sum of cathode and anode voltage drops. Such comparisons were made at the different discharge time. Then the history of the voltage drop across the gas-discharge channel was found out. It allowed dividing the energy deposited in the spark gap into energy deposited in the spark channel and the energy deposited at the cathode and anode regions.

It has to note that an assumption of direct proportionality between the spark gap length and the energy deposited in the spark channel is correct if the discharge current does not change when the gap length is varied. But an increase in the spark gap length leads to a rise in the resistance of the discharge channel, and it decreases the discharge current, respectively. As a rule, the resistance of the spark channel is significantly lower than total impedance of the electric discharge circuit. Therefore, a change in spark resistance caused by a change in the gap length affects the discharge current slightly. Nevertheless, this effect occurs and it requires an evaluation.

An experimental study of the gap length influence on the energy deposition in a spark discharge was made in work [9]. The total energy of the spark discharge ranged from 25 to 45 mJ. The deposited energy was measured using a calorimetric technique. It was found out that an increase in the length of the discharge gap leads to growth in the energy deposited in the spark discharge. And it was evaluated that the increase in the deposited energy deviates from directly proportional dependence on the gap length. But measuring accuracy of the calorimetric technique did not allow updating the dependence of the deposited energy on the gap length.

The energy deposition in the spark discharge was investigated in works [2, 10] by damping factors comparison of a short circuit current with the discharge current when a gas-filled spark gap is used as a load. So, the resistance of the electrical circuit was calculated from a damping factor of a short circuit current. A series connection of the spark gap with the electrical circuit leads to an increase in a resistance of the discharge circuit, and it influences on the damping factor of discharge current. Thus, the resistance calculated from the damping factor when spark gap is connected equals the sum of the circuit resistance and an average spark resistance. It allowed evaluating the average spark resistance then. And the deposited energy was found out by integration of discharge power over time.

It should be noted that the method applied in works [2, 10] does not give acceptable accuracy of the deposited energy measurement. It is caused by a wide range of the spark resistance change during the spark discharge evolution. Therefore, this method is not reasonable to use for studying the effect of the gap length on the deposited energy. Moreover, this method does not allow extracting the energy deposited in the gas-discharge channel from the energy deposited in the spark gap.

A gas-dynamic stage of spark development starts with a process of plasma channel contraction. The contraction usually happens when the duration of spark discharges exceeds a few hundreds of nanoseconds [11, 12]. Due to a significant growth in current density in the forming channel, the thermal ionization of the gas takes place in the channel, the gas becomes highly ionized, and the gas state exceeds an equilibrium one. The further development of the spark channel is accompanied by its gas-dynamic expansion. When duration of a spark discharge is over one microsecond and more, energy deposited in a gas-filled spark gap during the breakdown stage is typically lower than energy deposited during the stage of the gas-dynamic expansion. And the energy deposition at the expansion stage depends on the discharge current where a discharge electrical circuit influences the discharge current. So, we have studied the effect of the length of the gap on a spark discharges development when the energy deposition in the spark channel depends on the parameters of the electrical circuit.

There is a plurality of numerical models of spark development which adequately predict the processes occurring in the spark channel [13-18]. We used a numerical model of the spark channel expansion which was previously tested in a wide energy range [19-23].

The **aim** of the work is to study the influence of the length of the spark gap on energy input into the discharge channel during its gas-dynamic expansion.

Numerical model of spark channel expansion. It was assumed in the developed model that the expansion of the spark channel is determined by the following processes: non-stationary gas-dynamic expansion of the spark channel, a transient process in the electrical discharge circuit, nonequilibrium chemical processes, ionization of gas, radiation heat transfer and electron thermal conductivity. The process of collisions of electrons with atoms and molecules outside the thermally ionized spark channel was neglected because the electric field strength in the spark discharge during its expansion decreases to 100-1000 V/cm and lower [8]. The electrical conductivity was evaluated for a region of thermally

ionized gas where the degree of gas dissociation is high. Gray body radiation theory was used to take into account the radiative heat transfer in the high temperature gas and to simulate energy radiated from the high temperature spark channel [24]. Spectral radiative heat transfer in the low temperature gas was neglected due low power density. The nonequilibrium vibrational excitation of the gas in the shock wave was not considered. Molecular thermal conductivity was not taken into account because a value of such conductivity is significantly smaller than values of electron and radiative heat conductivities. The diffusion of atoms and molecules was not taken into account due to the high rates of mass transfer of the gas in the expanding channel. The scope of the model was limited by the condition that the magnetic pressure created by the discharge current is much less than the gas pressure.

Within the framework of the considered assumptions, the simulation of spark expansion was carried out by the system of equations

$$\frac{\partial}{\partial t}\begin{bmatrix}\rho\\ \rho u\\ \rho\varepsilon+\dfrac{\rho u^2}{2}\end{bmatrix}+\frac{1}{r}\frac{\partial}{\partial r}\begin{bmatrix}r\rho u\\ r\left(p+\rho u^2\right)\\ r\left(u\left(\rho\varepsilon+\dfrac{\rho u^2}{2}+p\right)+k_T\dfrac{dT}{dr}\right)\end{bmatrix}=\begin{bmatrix}0\\ \dfrac{p}{r}\\ \sigma E^2-W_{em}\end{bmatrix}, \quad (1)$$

where ρ is the gas density; u is the velocity, p is the pressure, ε is the specific internal energy of the gas, k_T is the thermal conductivity, E is the electric field strength, σ is the electrical conductivity of the gas, W_{em} is the radiative loss, r is the radial coordinate, t is the time, T is the gas temperature.

The radiated energy was calculated using the expression

$$W_{em}=\sigma_{SB}T^4/l_R, \quad (2)$$

where σ_{SB} is the Stefan–Boltzmann constant, l_R is the Rosseland mean free path.

The heat conductivity coefficient was calculated using the expression

$$k_T=k_e+k_{rad}=2.65\frac{T^{2.5}}{\ln\Lambda}+5.33\sigma_{SB}T^3l_R, \quad (3)$$

where k_e is the electron heat conductivity coefficient, k_{rad} is the radiative heat conductivity coefficient, $\ln\Lambda$ is the Coulomb logarithm.

Transient electrical process was calculated by the equation

$$L\frac{di}{dt}+\left[R_c+R_{sp}\right]\cdot i+\frac{1}{C}\int_0^t idt=0, \quad (4)$$

where C is the capacitor capacitance, R_c is the resistance of a discharge circuit; L is the inductance of a discharge circuit, R_{sp} is resistance of the spark channel, i is a current.

Resistance R_{sp} was defined by the expression

$$R_{sp}=l_{sp}/\int_0^Y 2\pi r\sigma dr, \quad (5)$$

where l_{sp} is the discharge gap length (channel); Y is maximum radius of the simulation domain, σ is an electrical conductivity.

The conductivity was calculated by equation

$$\sigma=2.82\cdot10^{-4}\frac{n_e}{n_N\upsilon\sigma_{tr}+n_e\upsilon\sigma_{cul}}, \quad (6)$$

where n_e is electron number density; σ_{tr} is the transport cross-section of the elastic collisions of the electrons with the neutral plasma components; σ_{cul} is the Coulomb collision cross-section; n_N is the number density of neutral components; υ is a mean thermal velocity of electron.

The number density of neutral components was defined by equations of chemical reaction kinetics considering the reaction (Table 1) where forward rate constant k_f is expressed as

$$k_f=A_fT^{n_f}\exp\left(\frac{-E_{af}}{RT}\right). \quad (7)$$

Table 1

The coefficients of the rate constant of forward reaction and the activation energy [25]

Reaction	A_f	n_f	E_{af}
$N_2 + M \leftrightarrow N + N + M$	$8.508\cdot10^{25}$	–2.25	225

Remark. M denotes the third particle. The values are expressed in calories, moles, cm^3, and s.

The Saha equations with regard to the single and double ionization of gas with components of e, N, N^+, N^{++} was applied to calculate the electron density n_e when the gas temperature exceeds 8000 K. It was assumed that plasma in the channel is quasi neutral too. A difference between temperature of electrons and temperature of atoms was estimated in the next section to evaluate a correctness of the local thermodynamic equilibrium approximation application.

The gas pressure was calculated using the expression

$$p=kT\sum n_c, \quad (8)$$

where n_c is a number density of all components (e, N, N^+, N^{++}, N_2).

The simulation procedure is presented in Fig. 1.

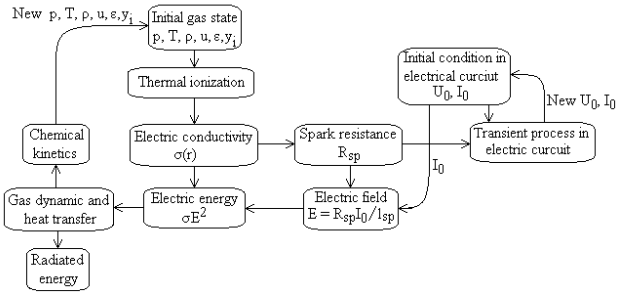

Fig. 1. Schematic of simulation procedure

Detail descriptions of the model and simulation procedure are presented in work [19].

The method of splitting by physical processes was applied to simulate gas-dynamic spark channel expansion combined with heat transfer and radiation, components concentration changing due to dissociation/association process, thermal gas ionization and transient process in electrical circuit.

The gradients of thermodynamic gas parameters are assumed to be absent for the discharge channel axis in a cylindrical symmetry. The computational area size was

prescribed in the manner of preventing disturbance from reaching the boundary. It is assumed that initial conditions have no gas dynamic perturbations in the entire computation region.

The model requires a circuit shorting to start simulating. The shorting of the discharge circuit occurs in a spark discharge as a result of the development of avalanche-spark or streamer-spark transition processes when the gap length is not extremely large. These processes are investigated, for example, in [5, 16]. As a result of these processes, a narrow channel with a radius of up to 0.1 mm is formed where a gas temperature of more than 10,000 K is reached, and the state of the gas approaches local thermodynamic equilibrium. Therefore, the energy was deposited into the channel of a small radius to rise the gas temperature from the initial one to 10,000 K. It is well known that when the capacitor discharge happens over the spark gap, the main part of the discharge energy is released during the high current pulses. Thus, the shorting energy was set in such a way that its value was significantly less than the total discharge energy. Therefore, a change in the conditions of the shorting energy deposition does not significantly influence the spark channel expansion because the further energy input into the spark is determined by the parameters of the discharge circuit. So, an energy was inputted initially in the simulated region with a radius of r_0 = 50 μm during a time of t = 10 ns to form a narrow current-conducting channel. This energy was 2.8 mJ.

Results and discussion. A spark discharge in series RLC-circuit with various circuit parameters was investigated. The first circuit had follow parameters where the damping factor was ζ = 0.38. A capacitance of C = 0.2 μF, an inductance of L = 500 nH, a resistance of R_c = 1.2 Ω were applied. The charge voltage was U_C = 3 kV. These circuit parameters correspond to the first simulation conditions. The second circuit had the following parameters where the damping factor was ζ = 0.11. A capacitance of C = 0.1 μF, an inductance of L = 2 μH, a resistance of R_c = 1 Ω were applied. The charge voltage was U_C = 30 kV. These circuit parameters correspond to the second simulation conditions. In both cases, a spark is ignited in molecular nitrogen with the initial gas temperature of T_0 = 300 K and the initial gas pressure of 0.1 MPa. A gap length was in a range from 1 mm to 20 mm.

The discharge currents at two electrical circuits with various spark gap lengths are shown in Fig. 2, 3. It is observed that an increase in the gap length led to a decrease in the amplitude of the discharge current at the both electrical circuits. But this effect is more pronounced at the first electrical circuit. So, the current amplitude at the first half cycle of the discharge decreased from 1111 A to 1010 A or by 10 % at the first circuit (Fig. 2) when the gap length is increased 3 times. Moreover, the current amplitude at the second half cycle of the discharge decreases by more than 45 %. The growth in the gap length to 6 mm caused a fall in the current amplitude at the first half cycle to 873 A or by 27 %.

The current amplitude at the first half cycle of the discharge decreased from 5669 A to 5471 A or by 3.65 % only when the gap length is increased 10 times at the second circuit (Fig. 3). Moreover, the current amplitude reduction did not exceed 6.5 % in the second half cycle of the discharge. The current amplitude at the first half cycle of the discharge did not exceed 5261 A by the gap length of 20 mm.

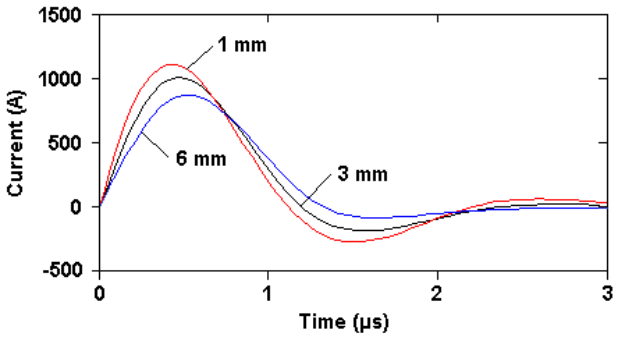

Fig. 2. The discharge current over time at the first electrical circuit with the gap length of 1 mm, 3 mm and 6 mm

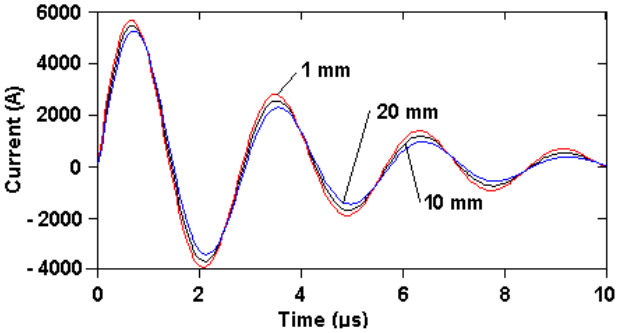

Fig. 3. The discharge current over time at the second circuit with a gap length of 1 mm, 10 mm and 20 mm

The dependences of the spark channel resistance on the discharge time at two electrical circuits with the various spark gap lengths are shown in Fig. 4, 5. In both cases the increased length of the discharge gap led to a rise in the resistance of the spark channel. The minimum value of the spark resistance in particular increases from 59 mΩ to 196 mΩ or 3.3 times at the first circuit (Fig. 4) when the gap length is enlarged three times. A six-fold increase in the length caused the minimum value rise to 449 mΩ or 7.6 times.

The minimum value of the spark resistance rises from 6.45 mΩ to 69 mΩ or 10.7 times at the second circuit (Fig. 5) when the gap length is enlarged ten times. And the minimum value grows to 147 mΩ or 22.8 times when the twenty-fold gap increase happens.

Thus, it was simulated that the minimum value of the spark resistance is nearly in direct proportion to the gap length.

The study of the gap length influence on the electric field strength in the spark channel at the calculated cases is presented in the Fig. 6, 7.

It is observed at the both circuits that a decrease in the field strength happens in 0.2–0.3 μs from the spark expansion start and the strength reduces to 1000 V/cm and lower. The effect of the gap length on the field strength is more pronounced at the first circuit (Fig. 6) than it effects at the second circuit (Fig. 7).

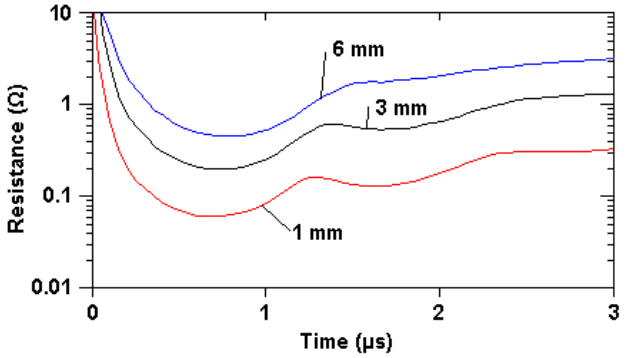

Fig. 4. The spark channel resistance over time at the first circuit with a gap length of 1 mm, 3 mm and 6 mm

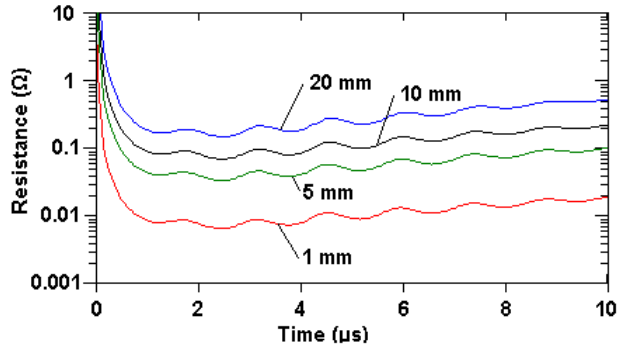

Fig. 5. The spark channel resistance over time at the second circuit with a gap length of 1 mm, 5 mm, 10 mm and 20 mm

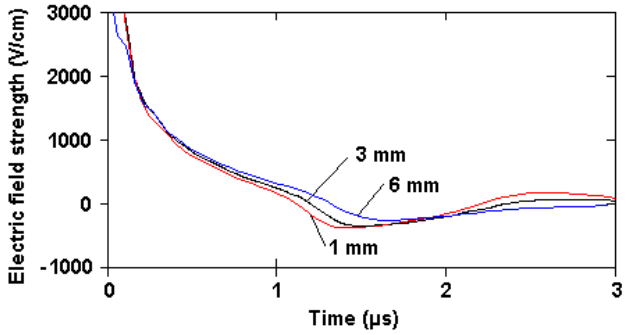

Fig. 6. The electric field strength over time at the first circuit with a gap length of 1 mm, 3 mm and 6 mm

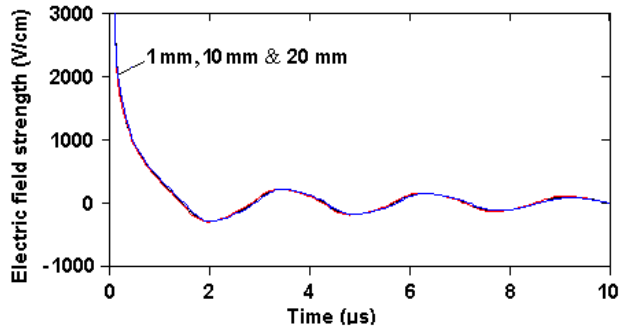

Fig. 7. The electric field strength over time at the second circuit with a gap length of 1 mm, 10 mm and 20 mm

The energy deposited in the spark channel over time at the calculated circuits with the various gap lengths is shown in Fig. 8, 9. We multiplied data of the deposited energy with a gap length of 1 mm by a number which equaled a ration of the gap growth to find out the effect of the gap length on the deposited energy. It is observed that the deposited energy increases when the gap length rises. Pulses of the discharge current cause an increase in the deposited energy. A main energy deposition happens during the first half cycle of the discharge. It is explained by a high discharge current and a high spark resistance during this period of the discharge development. The deviation of the energy growth from the directly proportional dependence on the gap length is observed at the both circuits (Fig. 8, 9). So, the three-fold increase in the deposited energy at the first circuit with the gap length of 1 mm differs by 11 % from the deposited energy at the case when the gap length was 3 mm (Fig. 8). Such an energy difference grows by 29 % when the gap length exceeds 6 mm. It should be noted that the Joule energy deposited in the resistance is directly proportional to the square of the discharge current. Therefore, it was previously expected that when the spark gap is increased from 1 mm to 6 mm at the first circuit, the deposited energy will decrease $1.27 \times 1.27 \approx 1.6$ times relative to 0.478 J (see Fig. 8) due to a decrease in the discharge current 1.27 times (see Fig. 2). So, the expected deposited energy was 0.298 J. But it was simulated that the deposited energy equals 0.371 J when the gap length is 6 mm. It occurs because a decrease in the discharge current causes an increase in the spark resistance that partially compensates for the drop in the deposited energy. For instance, when the gap length at the first circuit is increased 6 times, the minimum spark resistance increases not 6 times, but 7.6 times.

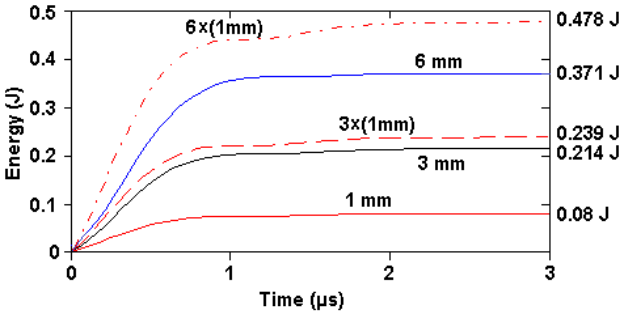

Fig. 8. The energy deposited in the spark channel over time at the first circuit with a gap length of 1 mm, 3 mm and 6 mm. The dotted line denotes the three-fold increase in the deposited energy at the first circuit with the gap length of 1 mm. The dot-and-dash line denotes the six-fold increase

The ten-fold increase in the deposited energy in the second circuit with the gap length of 1 mm differs by 6 % only from the deposited energy at the case when the gap length was 10 mm (Fig. 9). The deviation of the energy growth from the directly proportional dependence on the gap length at the first half cycle of the discharge did not exceed 3.6 % when the gap length was 10 mm. The difference in the deposited energy exceeds 13.2 % when the gap length equals 20 mm.

According to the simulation results we think that the energy deposited into the spark channel is directly proportional to the length of the spark gap as the first approximation. But when the minimum resistance of the spark channel and the resistance of the discharge circuit have the same order of magnitude and the damping factor is high, it is necessary to specify the deposited energy growth due to the gap length increase. A difference in the

discharge current can be used as a sign to specify the deposited energy.

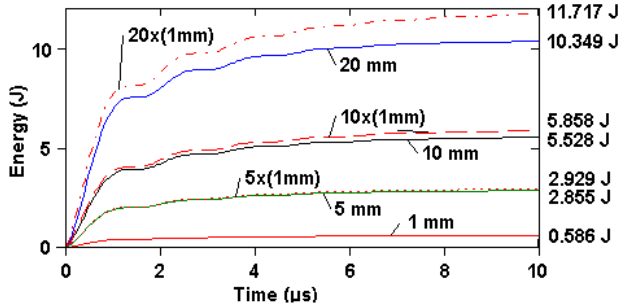

Fig. 9. The energy deposited in the spark channel over time at the second circuit with a gap length of 1 mm, 5 mm, 10 mm and 20 mm. The dashed line denotes the five-fold increase in the deposited energy at the second circuit with the gap length of 1 mm. The dotted line denotes the ten-fold increase, and the dot-and-dash line denotes the twenty-fold increase

Although extensive research has been carried out where the length of the discharge gap has been variable [6, 26], there is a problem to compare the calculated results with the experimental data. The reason for this is that a change in the gap length under constant gas pressure leads to a change in breakdown voltage. The increased breakdown voltage requires to rise the charge voltage of the discharge capacitor and, accordingly, to increase the total discharge energy. And growth in the total energy is accompanied by an increase in the energy deposited into the spark discharge. As a result, there are difficulties to separate the effect of the capacitor charge voltage from the effect of the gap length on the deposited energy.

Therefore, it was carried out a comparison of the calculated results with the results of experimental studies [9, 27], where the breakdown voltage did not change when the gap length is variable due to a regulation of the gas pressure p in the discharge medium.

It was assumed that the following condition take place

$$U_{br} = \text{const}, \quad \text{if} \quad p \cdot l_{sp} = \text{const}, \tag{9}$$

where U_{br} is the breakdown voltage.

The results of experimental studies [9, 27] confirm that an increase in the length of the spark gap leads to a rise in the energy deposited into the gap. It is also confirmed that the change in the deposited energy deviates from a directly proportional dependence on the factor of change in the length of the gap. For example, it was found out in [9] that the thermal energy is 7 mJ at the experimental circuit when the gas pressure is 2 bar and the gap length is 1 mm. The thermal energy is about 12.5 mJ at such a circuit when the pressure is 1 bar and the length is 2 mm. Thus, there is a 1.78-fold increase in the deposited energy in the case of a two-fold increase in the length of the spark gap and a decrease in the pressure of the gas-discharge medium by a factor of two. To separate the effect of pressure from the effect of the gap length on the deposited energy, we use the data from [23], where it was found out that a 2-fold increase in gas pressure leads to an increase in the deposited energy by 10 %. So, we have that a decrease in gas pressure from 2 bar to 1 bar by the gap length of 1 mm would lead to a decrease in the deposited energy from 7 J to 6.3 mJ. As a result, we have that a two-fold increase in the gap length led to a 1.98-fold increase in the deposited energy.

The results of an experimental study of the effect of the gap length and the gas pressure on the realized energy are also presented in [27]. It should be noted that the total energy deposited into the discharge gap consists of the sum of the energy realized into the gas discharge channel and the energy released in the near electrode regions. The results of [27] allow us to separate these energy components. In particular, the energy released in the near-electrode regions corresponds to the total deposited energy when the spark gap length is about zero. According to the results of experimental studies, a close-to-linear relationship was found out between the gap length and the deposited energy. For example, it was measured [27] that the total deposited energy is 2.3 J at the investigated circuit with a spark gap of 1 mm and gas pressure of 1 bar. The following energy balance happens. The energy of 1.8 J is released in the near-electrode region, and the energy of 0.5 J is deposited in the spark channel. The total deposited energy equals 4 J at such a circuit when the gap length is 10 mm and the pressure is 0.1 bar where energy of 1.4 J is released in the near-electrode region, and energy of 2.6 J is released in the spark channel. According to the results of [23], an increase in pressure by a factor of 10 leads to an increase in the deposited energy by 70 %. It follows that a decrease in pressure from 1 bar to 0.1 bar over a spark gap of 1 mm would lead to a decrease in the deposited energy from 0.5 J to 0.29 J.

Thus, an increase in the length of the gap by a factor of 10 led to an increase in the deposited energy 8.96 times. We have that the influence of the gap length, revealed by the results of numerical studies, is in satisfactory correlation with the experimental data.

Distribution of pressure, temperature and gas density along the radial coordinates at different time allow to evaluate an influence of the spark gap length on the discharge channel expansion (Fig. 10, 11).

There is a slight deviation of thermodynamic parameters with a change in the length of the spark gap at the first circuit (Fig. 10). This effect is caused by a reduction in the spark energy deposited per a unit of the gap length.

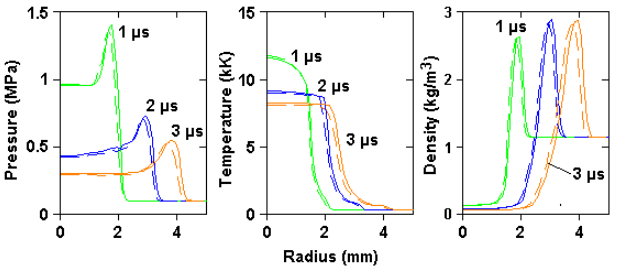

Fig. 10. Distribution of pressure, temperature and gas density along the radial coordinates at time of 1 μs, 2 μs and 3 μs at the first circuit with a gap length of 1 mm (full lines) and 3 mm (dotted lines)

Negligible deviation of thermodynamic parameters was observed at the second circuit. Thus, it was difficult to show the difference in the Fig. 11.

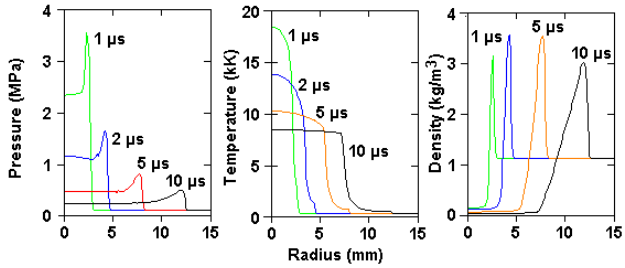

Fig. 11. Distribution of pressure, temperature and gas density along the radial coordinates at time of 1 μs, 2 μs and 3 μs at the second circuit with a gap length of 1 mm and 10 mm

The simulated results of the spark evolution at the both considered cases correspond to the experimental data in general. So, the shock wave starts separating from the current conductive region (high-temperature region) in about 1 μs from the spark expansion start. Also, the growth of the total energy of the discharge, which occurs during transition from the first to the second circuit, leads to an increase in the intensity of the generated shock wave. This qualitative comparison and the previous verification of the model give reason to consider that the obtained results are reliable.

Due to the visible difference in the temperature distribution at the first circuit, the effect of the gap length on the energy radiated by the spark discharge was estimated for this case. The results of the radiated energy versus time for the gap length of 1 mm, 3 mm and 6 mm are presented in Fig. 12.

It is observed that growth of the gap length leads to a rise in the radiated energy. A three-fold increase in the radiated energy at the first circuit with a gap length of 1 mm differs from the radiated energy at such a circuit with a length of 3 mm by 13 % (Fig. 12). Thus, we have a similar tendency of influence of the gap length on the radiated energy. But the influence on the radiated energy is slightly intensive than the influence on the deposited energy.

We should separately discuss the possible effect of changing the length of the discharge gap on the cathode and anode voltage drop and, accordingly, on the energy released in the spark. There are two contradicting results on the magnitude of the voltage drop in the near electrode regions in the spark discharge.

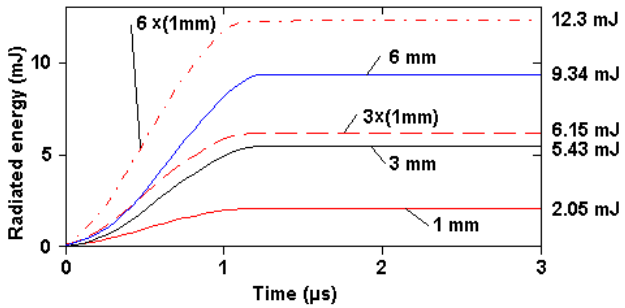

Fig. 12. Dependence of energy radiated by the spark discharge on time at the first circuit with a gap length of 1 mm and 3 mm. The dotted line denotes three-fold increasing radiated energy when the gap length was 1 mm. The dot-and-dash line denotes the six-fold increase

According to the data of [28], the near-electrode voltage drop does not depend on the discharge current that happens in the stationary arc discharge. And the voltage drop is about several volts. Since the voltage drop across the spark channel, as a rule, is several times higher than the mentioned near-electrode voltage drop, the influence of this factor on the balance of energy release in the spark can be negligible in this case. According to the experimental data of [29], the voltage drop in the near electrode regions changes during the spark evolution. And this voltage is comparable in magnitude with the voltage drop across the spark channel. It was assumed in [23] that an increased voltage drop in the near electrode regions is caused by an increased current density in the spark discharge. Since a change in the length of the discharge gap leads to a change in the discharge current and current density, the influence of the change in the voltage drop in the near electrode regions on the balance of energy release in the spark discharge can influence more strongly in this case. Therefore, this issue requires a separate study.

It has to discuss a local thermo-equilibrium approximation application to a region where gas temperature is above 8000 K. We use a two-temperature plasma model to evaluate a difference between temperature of electrons and temperature of atoms [30]. We assumed that the temperature of electrons is quasi-steady and plasma is neutral. The atomic gas was considered. The double ionization of gas was neglected. The follow systems of equations were solved [30, 31]:

$$n_e = \left[6.06 \cdot 10^{21} n_N \frac{Z_i}{Z_a} T_e^{1.5} \exp\left(-\frac{E_i}{kT_e} \right) \right]^{0.5}, \quad (10)$$

$$\frac{e^2 E^2}{m_e \nu_m^2} = \frac{3}{2} \delta k \left(T_e - T_i \right), \quad (11)$$

$$p = n_N k T_i + n_e k \left(T_e + T_i \right), \quad (12)$$

$$\nu_m = \left(\sigma_{tr} n_N + \sigma_{cul} n_e \right) \cdot \upsilon, \quad (13)$$

$$\upsilon = 6.71 \cdot 10^7 \cdot \sqrt{T_e}, \quad (14)$$

$$\sigma_{cul} = \frac{2.87 \cdot 10^{-14} \ln \Lambda}{T_e^2}, \quad (15)$$

$$\ln \Lambda = 7.47 + \frac{3}{2} \log\left(T_e \right) + \frac{1}{2} \log\left(n_e \right), \quad (16)$$

where T_e is temperature of electrons; T_i is temperature of atoms; Z_a and Z_i are partition functions; E_i is the ionization potential; e is electron charge; m_e is electron mass; ν_m is the effective collision frequency for momentum transfer; δ is a fraction of energy transfer by a single collision of electron with atom ($\delta = 2m_e/m_a$, where m_a is a mass of atom); $\ln\Lambda$ is the Coulomb logarithm.

The system of equation (10) – (16) can be solved when the gas pressure and the electric field strength are known. The growth in the strength of the electric field causes the rise in the temperature difference that follows from equation (11). Thus, we use data of the strength histories (Fig. 6, 7) by local maximums of the strength curves.

It was found out that when p = 1 MPa, E = 300 V/cm and T_i = 10…13 kK, the temperature difference was varied in the range from 0.5 % to 5.5 % (Fig. 13,*a*). This condition corresponds to the first circuit at time of 0.7…1 μs.

The temperature difference growth when the temperature of atoms decreases. So, it was found out that when p = 0.3 MPa, E = 150 V/cm and T_i = 8…9 kK, the temperature difference was varied in the range from 11 % to 19 % (Fig. 13,*b*). This condition corresponds to the first circuit at time of 2.5…3 μs. But this difference cannot significantly influence on the simulated result because the main energy deposition stopped at about 1 μs (Fig. 8).

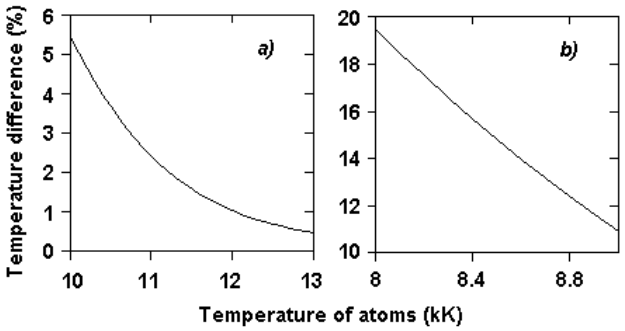

Fig. 13. Dependence of the temperature difference on the temperature of atoms when: *a)* p = 1 MPa, E = 300 V/cm and *b)* p = 0.3 MPa, E = 150 V/cm

The similar tendency for the temperature difference charge happens at the second circuit. Taking into account the low value of the temperature difference, it allows us to assume that the local thermo-equilibrium approximation can be used in the numerical model.

Conclusions.

It was confirmed by the numerical study that the increase in the length of the discharge gap leads to growth in energy deposited into the spark discharge, a decrease in the amplitude of the discharge current and an increase in the resistance of the spark channel. But the change in the amplitude of the discharge current caused by the gap length variation depends on the discharge circuit parameters. We think the effect of the gap length on the discharge current enhances in case of a rise in the damping factor. So, it was observed that when the damping factor equaled ζ = 0.38 at the simulated discharge circuit, three-hold increase in the gap length caused the decline in the current amplitude by 10 % at the first half cycle of the discharge. But when the damping factor equaled ζ = 0.11, ten-hold increase in the gap length caused the decline in the current amplitude by 3.65 % only. The effect of the gap length on the electric field strength was more visible by the increased damping factor too. It was observed insignificant effect of the gap length on the spark channel expansion. It was found out that the minimum spark resistance, the deposited energy into the spark channel and the radiated energy are practically directly proportional to the spark gap length. But deviation from the direct proportionality rises when the minimum resistance of the spark channel and the resistance of the discharge circuit have the same order of magnitude and the damping factor is high. It was found out that the influence of the spark gap variation on the radiated energy is slightly intensive than the influence on the deposited energy.

Conflict of interests. The authors declare no conflicts of interest.

REFERENCES

1. Essmann S., Markus D., Grosshans H., Maas U. Experimental investigation of the stochastic early flame propagation after ignition by a low-energy electrical discharge. *Combustion and Flame*, 2020, vol. 211, pp. 44-53. doi: https://doi.org/10.1016/j.combustflame.2019.09.021.

2. Kamenskihs V., Ng H.D., Lee J.H.S. Measurement of critical energy for direct initiation of spherical detonations in stoichiometric high-pressure H2–O2 mixtures. *Combustion and Flame*, 2010, vol. 157, issue 9, pp. 1795-1799. doi: https://doi.org/10.1016/j.combustflame.2010.02.014.

3. Korytchenko K., Krivosheyev P., Dubinin D., Lisniak A., Afanasenko K., Harbuz S., Buskin O., Nikorchuk A., Tsebriuk I. Experimental research into the influence of two-spark ignition on the deflagration to detonation transition process in a detonation tube. *Eastern-European Journal of Enterprise Technologies*, 2019, vol. 4, no. 5 (100), pp. 26-31. doi: https://doi.org/10.15587/1729-4061.2019.175333.

4. Zhang B., Bai C. Critical energy of direct detonation initiation in gaseous fuel-oxygen mixtures. *Safety Science*, 2013, vol. 53, pp. 153-159. doi: https://doi.org/10.1016/j.ssci.2012.09.013.

5. Zhang J., Markosyan A.H., Seeger M., Veldhuizen E.M., Heesch E.J.M., Ebert U. Numerical and experimental investigation of dielectric recovery in supercritical N2. *Plasma Sources Science and Technology*. 2015, vol. 24, no. 2, pp. 025008. doi: https://doi.org/10.1088/0963-0252/24/2/025008.

6. Palomares J.M., Kohut A., Galbács G., Engeln R., Geretovszky Zs. A time-resolved imaging and electrical study on a high current atmospheric pressure spark discharge. *Journal of Applied Physics*. 2015, vol. 118, no. 23, pp. 233305. doi: https://doi.org/10.1063/1.4937729.

7. Gostimirovic M., Kovac P., Sekulic M., Skoric B. Influence of discharge energy on machining characteristics in EDM. *Journal of Mechanical Science and Technology*, 2012, vol. 26, no. 1, pp. 173-179. doi: https://doi.org/10.1007/s12206-011-0922-x.

8. Abramson I.S., Gegechkori N.M. Oscillographic research of spark discharge. *Journal of Experimental and Theoretical Physics*, 1951, vol. 21, no. 4, pp. 484-492.

9. Benito Parejo C., Michalski Q., Sotton J., Bellenoue M., Strozzi C. Characterization of Spark Ignition Energy Transfer by Optical and Non-Optical Diagnostics. *8th European Combustion Meeting*, 2017, ECM2017.0198.

10. Knystautas R., Lee J.H. On the effective energy for direct initiation of gaseous detonations. *Combustion and flame*, 1976, vol. 27, pp. 221-230. doi: https://doi.org/10.1016/0010-2180(76)90025-0.

11. Minesi N., Stepanyan S., Mariotto P., Stancu G-D., Laux C. On the arc transition mechanism in nanosecond air discharges, *AIAA Scitech 2019 Forum*, 2019, 2019-0463. doi: https://doi.org/10.2514/6.2019-0463.

12. Gegechkori N.M. Experimental studies of spark discharge channel. *Journal of Experimental and Theoretical Physics*, 1951, vol. 21, no. 4, pp. 493-506.

13. Tanaka Y., Michishita T., Uesugi Y. Hydrodynamic chemical non-equilibrium model of a pulsed arc discharge in dry air at atmospheric pressure. *Plasma Sources Science and Technology*, 2005, vol. 14, no. 1, pp. 134-154. doi: https://doi.org/10.1088/0963-0252/14/1/016.

14. Tanaka Y., Sakuta T. Modelling of a pulsed discharge in N_2 gas at atmospheric pressure, *Journal of Physics D: Applied Physics*, 1999, vol. 32, no. 24, pp. 3199-3207. doi: https://doi.org/10.1088/0022-3727/32/24/316.

15. Janda M., Machala Z., Niklová A., Martišovitš V. The streamer-to-spark transition in a transient spark: a dc-driven nanosecond-pulsed discharge in atmospheric air. *Plasma Sources Science and Technology*, 2012, vol. 21, no. 4, p. 045006. doi: https://doi.org/10.1088/0963-0252/21/4/045006.

16. Marode E., Bastien F., Bakker M. A model of the streamer-induced spark formation based on neutral dynamics. *Journal of Applied Physics*, 1979, vol. 50, no. 1, p. 140-146. doi: https://doi.org/10.1063/1.325697.
17. Paxton A., Gardner R., Baker L. Lightning return stroke. A numerical calculation of the optical radiation. *Physics of Fluids*, 1986, vol. 29, no. 8, p. 2736. doi: https://doi.org/10.1063/1.865514.
18. Shneider M. Turbulent decay of after-spark channels. *Physics of Plasmas*, 2006, vol. 13, no. 7, p. 073501, doi: https://doi.org/10.1063/1.2218492.
19. Korytchenko K., Essmann S., Markus D., Maas U., Poklonskii Ye. Numerical and Experimental Investigation of the Channel Expansion of a Low-Energy Spark in the Air. *Combustion Science and Technology*, 2019, vol. 191, no. 12, pp. 2136-2161. doi: https://doi.org/10.1080/00102202.2018.1548441.
20. Korytchenko K., Markov V., Polyakov I., Slepuzhnikov E., Meleshchenko R. Validation of the numerical model of a spark channel expansion in a low-energy atmospheric pressure discharge. *Problems of Atomic Science and Technology*, 2018, vol. 4, pp. 144-146.
21. Korytchenko K., Poklonskiy E., Vinnikov D., Kudin D. Numerical simulation of gas-dynamic stage of spark discharge in oxygen. *Problems of Atomic Science and Technology*, 2013, vol. 4, pp. 155-160.
22. Korytchenko K.V., Poklonskii E.V., Krivosheev P.N. Model of the spark discharge initiation of detonation in a mixture of hydrogen with oxygen. *Russian Journal of Physical Chemistry B*, 2014, vol. 8, no. 5, pp. 692-700. doi: https://doi.org/10.1134/S1990793114050169.
23. Korytchenko K.V., Tomashevskiy R.S., Varshamova I.S., Meshkov D.V., Samoilenko D. Numerical investigation of energy deposition in spark discharge in adiabatically and isothermally compressed nitrogen. *Japanese Journal of Applied Physics*, 2020, vol. 59, no. SH, p. SHHC04. doi: https://doi.org/10.35848/1347-4065/ab72cc.
24. Zel'dovich Y.B., Raizer Yu. *Physics of shock waves and high-temperature hydrodynamic phenomena*. Dover Publications, Inc., Mineola, NY, 2002, 896 p.
25. Petersen E.L., Hanson R.K. Reduced kinetics mechanisms for ram accelerator combustion. *Journal of Propulsion and power*, 1999, vol. 15, no. 4, pp. 591-600. doi: https://doi.org/10.2514/2.5468.
26. Belmouss M. Effect of electrode geometry on high energy spark discharges in air. *Thesis, Purdue University West Lafayette*, Indiana, 2015, 556.
27. Li X., Liu X., Zeng F., Yang H., Zhang Q. Study on Resistance and Energy Deposition of Spark Channel Under the Oscillatory Current Pulse. *IEEE Transactions on Plasma Science*, 2014, vol. 42, no. 9, pp. 2259-2265. doi: https://doi.org/10.1109/tps.2014.2331346.
28. Hemmi R., Yokomizu Y., Matsumura T. Anode-fall and cathode-fall voltages of air arc in atmosphere between silver electrodes. *Journal of Physics D: Applied Physics*, 2003, vol. 36, no. 9, pp. 1097-1106. doi: https://doi.org/10.1088/0022-3727/36/9/307.
29. Abramson I.S., Gegechkori N.M. Oscillographic research of spark discharge. *Journal of Experimental and Theoretical Physics*, 1951, vol. 21, no. 4, pp. 484-492.
30. Donskoi A.V., Goldfarb V.M., Klubnikin V.S., Dresvin S.V., Eckert H.U., Cheron T. *Physics and technology of low-temperature plasmas*. Iowa State University Press, 1977. 471 p.
31. Raizer Yu. *Gas discharge physics*. Spinger-Verlag, Germany, 1991. 460 p.

Received 06.11.2020
Accepted 11.12.2020
Published 25.02.2021

K.V. Korytchenko[1], *Doctor of Technical Science, Professor,*
O.V. Shypul[2], *Ph.D., Associate Professor,*
D. Samoilenko[3], *Dr Hab. Inż.,*
I.S. Varshamova[1], *Senior Lecturer,*
A.A. Lisniak[4], *Ph.D., Associate Professor,*
S.V. Harbuz[4], *Ph.D.,*
K.M. Ostapov[4], *Ph.D.,*
[1] National Technical University «Kharkiv Polytechnic Institute», 2, Kyrpychova Str., Kharkiv, 61002, Ukraine,
e-mail: korytchenko_kv@ukr.net, varshamova.i.s@gmail.com
[2] National Aerospace University «Kharkiv Aviation Institute», 17, Chkalov Str., Kharkiv, Ukraine, 61070,
e-mail: o.shipul@khai.edu
[3] Warsaw University of Technology,
Pl. Politechniki 1, 00-661 Warsaw, Poland,
e-mail: dmytro.samoilenko@pw.edu.pl
[4] National University of Civil Defense of Ukraine,
94, Chernyshevska Str., Kharkiv, 61023, Ukraine,
e-mail: ptarr@nuczu.edu.ua, sgarbuz65@gmail.com, ostapovk_90@ukr.net

How to cite this article:
Korytchenko K.V., Shypul O.V., Samoilenko D., Varshamova I.S., Lisniak A.A., Harbuz S.V., Ostapov K.M. Numerical simulation of gap length influence on energy deposition in spark discharge. *Electrical Engineering & Electromechanics*, 2021, no. 1, pp. 35-43. **doi: 10.20998/2074-272X.2021.1.06.**

UDC 621.319 **doi: 10.20998/2074-272X.2021.1.07**

G.V. Bezprozvannych, I.A. Kostiukov, O.A. Pushkar

SYNTHESIS OF CONSTRUCTIVE-TECHNOLOGICAL DECISIONS OF REGULATION OF WORKING CAPACITANCE OF CABLES OF INDUSTRIAL NETWORKS

Introduction. *Over the past 10 years, the number of industrial networks has more than doubled. At the physical level, all industrial technology networks are based on twisted pair.* ***Purpose.*** *Synthesis of constructive-technological decisions of regulation of electric capacitance of the insulated conductor at a stage of manufacturing of twisted pair of cables of industrial networks.* ***Methodology.*** *The method of secondary charges to determine the capacitance of the insulated conductor by varying the thickness of the solid and foamed polyethylene insulation.* ***Practical value.*** *Effective regulation is provided on the basis of the obtained dependencies of the effective dielectric constant, the tangent of the dielectric loss angle and the capacitance of the insulated conductor on the degree of foaming and the thickness of the protective film of two-layer insulation. At a degree of porosity of 40 %, the dielectric constant decreases by 25 %, the tangent of the dielectric loss angle – by 33 %, the electrical capacitance of the insulated conductor – by 20 %.* References 18, tables 3, figures 5.

Key words: **industrial networks, twisted pair, insulated conductor, foaming, insulation thickness, effective dielectric constant, electrical capacitance.**

Доведено більшу чутливість регулювання технологічного процесу виготовлення ізольованого провідника витої пари при охолодженні у воді в порівнянні з повітряним. При зміненні товщини ізоляції в 4 рази електрична ємність ізольованого провідника змінюється більше, ніж в 2 рази, та на 5 % при знаходженні у воді та повітрі відповідно. Ефективне регулювання забезпечується на підставі отриманих залежностей ефективної діелектричної проникності, тангенсу кута діелектричних втрат та ємності ізольованого провідника від ступеню спінення та товщини захисної плівки двошарової ізоляції. При ступені пористості 40 % діелектрична проникність зменшується на 25 %, тангенс кута діелектричних втрат – на 33 %, електрична ємність ізольованого провідника – на 20 %. Бібл. 18, табл. 3. рис. 5.

Ключові слова: **промислові мережі, вита пара, ізольований провідник, спінення, товщина ізоляції, ефективна діелектрична проникність, електрична ємність.**

Доказано большую чувствительность регулирования технологического процесса изготовления изолированного проводника витой пары при охлаждении в воде по сравнению с воздушным. При изменении толщины изоляции в 4 раза электрическая емкость изолированного проводника меняется более чем в 2 раза, и на 5 % при нахождении в воде и воздухе соответственно. Эффективное регулирование обеспечивается на основании полученных зависимостей эффективной диэлектрической проницаемости, тангенса угла диэлектрических потерь и емкости изолированного проводника от степени вспенивания и толщины защитной пленки двухслойной изоляции. При степени пористости 40 % диэлектрическая проницаемость уменьшается на 25 %, тангенс угла диэлектрических потерь – на 33 %, электрическая емкость изолированного проводника – на 20 %. Библ. 18, табл. 3, рис. 5.

Ключевые слова: **промышленные сети, витая пара, изолированный проводник, вспенивание, толщина изоляции, эффективная диэлектрическая проницаемость, электрическая емкость.**

Introduction. The rapid growth of digital technologies has prompted cable manufacturers in Ukraine to introduce new technologies and types of cables, in particular, based on twisted pairs of different categories, with an appropriate set of transmission parameters, both for structured cable systems and for security systems – video surveillance, fire and security alarm system [1-6]. At the same time, each industrial enterprise to ensure the competitiveness of manufactured products contributes to the automation of both individual technological processes and production as a whole. For this purpose it is necessary to enter all active and passive devices into a single information industrial-technological network, where the interaction between the devices takes place using software-logical communication protocols. Industrial networks usually do not go beyond a single enterprise. Over the past 10 years, the number of industrial networks has more than doubled [7]. By 2025, it is expected to grow by 280 % compared to 2010 [7]. At the physical level, all industrial-technological networks (FieldBus Profibus, LonWorks and others) are based on twisted pair or optical fiber, and solutions based on electrical cables are used to a greater extent (Table 1) [3, 4, 7].

Table 1

Characteristics of industrial networks

Type of industrial bus topology network	Signal transmission speed	Maximum signal transmission range, m
Profibus DP	9.6 kBit/s – 12 kBit/s	100 – 1200
Profibus PA	31.25 kBit/s	1900
Canopen	62.5 kBit/s – 1 MBit/s	30 – 1000
DEviceNet	125 – 500 kBit/s	100 – 500

With the advent of Ethernet and the Internet for industrial networks they began to apply the same classification as for information, structured, local area networks (Table 2). The industrial Ethernet market is growing at a rate of 51 % per year [7]. As the network is modernized, which involves the transition from obsolete fieldbus to Industrial Ethernet, communication cable infrastructure becomes the basis for connection to the communications of the industrial enterprise.

Existing Industrial Ethernet physical level technologies have a limit on the distance to which the signal is transmitted – no more than 100 m.

Due to the fact that process automation applications require distances of 1 km and even more in combination with reliable field devices suitable for use in zone 0 applications (intrinsically safe), a new approach to the implementation of Ethernet physical level technology was needed. Adopted new standard 10BASE-T1L of physical level of Industrial Ethernet (IEEE 802.3cg-2019 (Table 2)) will radically change the field of process automation by significantly increasing the operational efficiency of the enterprise by organizing a highly reliable seamless (without the use of gateways) connection to Ethernet at the field level, which provides a variety of devices, including sensors and actuating mechanisms – actuators, programmable logic controllers [7]. The 10BASE-T1L Standard solves the problems that currently limit the use of Ethernet in the field in the area of process automation: insufficient bandwidth, relative complexity of cabling, limited data transmission range, which is directly related to cable bandwidth (constructive-technological solutions).

Table 2

International Standards and categories of twisted pair cables for Industrial Ethernet networks [7]

Year of adoption of the Standard	IEEE 802.3 Standard		Maximum signal transmission range, m	Signal transmission speed	Twisted pair cable bandwidth	Cable category according to the recommendations of ISO/IEC	Number of pairs
1999	IEEE 802.3ab	1000BASE-T	100	1 GBit/s	125 MHz	Category 5e	4
2006	IEEE 802.3an	10GBASE-T	55	10 GBit/s	250 MHz	Category 6	4
2006	IEEE 802.3an	10GBASE-T	100	10 GBit/s	500 MHz	Category 6	4
2006	IEEE 802.3an	10GBASE-T	100	10 GBit/s	600 MHz	Category 7	4
2006	IEEE 802.3an	10GBASE-T	100	10 GBit/s	1000 MHz	Category 7a	4
2015	IEEE 802.3 bw	100BASE-T1	15 m UTP	100 MBit/s	66 MHz	SPE	1
2016	IEEE 802.3 bp	1000BASE-T1	40 15 m UTP	1000 MBit/s	600 MHz	SPE	1
2019	IEEE 802.3 cg	10BASE-T1L 10BASE-T1S	1000 25 m UTP	10 MBit/s	20 MHz	SPE	1
2020	IEEE 802.3 ch	Multi-Gig	(15 m)	(2.5/5//10 GBit/s)	–	SPE	1

The 10BASE-T1L Standard supports two signal amplitude modes: 2.4 V for cable lengths up to 1000 m and 1 V at a shorter distance. The 1 V full amplitude mode means that this new physical-level technology can also be used in Ex-proof systems, following strict rules to limit maximum energy. Most importantly, the 10BASE-T1L Standard provides long-distance transmission thanks to two-wire technology with power supply and data on one cable in the form of twisted pair and belongs to the family of environments with single-pair Ethernet (SPE) (Table 2).

It should be noted that the enterprises of the cable industry of Ukraine do not produce cables for industrial networks. The suppliers of such cables to Ukraine for industrial automation and control are the world's leading companies, in particular, ABB, Siemens, Belden, Helucable [7].

The development of innovative cable products by Ukrainian enterprises requires solving the problem of synthesis of design and technological solutions to establish the production of cables for industrial networks with the appropriate set of electrical parameters.

The goal of the paper is the synthesis of constructive and technological solutions for regulating the electrical capacitance of an insulated conductor at the stage of manufacturing twisted pair cables of industrial networks.

Problem definition. The transmission range and bandwidth of signals in the cable depends on the design and technological solutions that determine the attenuation coefficient, which is determined by the active resistance of conductors R, inductance L, working capacitance C_p, active insulation conductivity G (dielectric loss tangent $tg\delta$) [8].

In the high-frequency range, the attenuation coefficient has two components: losses in the metal (conductor) α_m and losses in the dielectric (insulation) α_d

$$\alpha = 8.69 \cdot \left(\frac{R}{2}\sqrt{\frac{C_p}{L}} + \frac{G}{2}\sqrt{\frac{L}{C_p}} \right) =$$

$$= 8.69 \cdot \left(\frac{R}{2}\sqrt{\frac{C_p}{L}} + \frac{\omega C_p \, tg\delta}{2}\sqrt{\frac{L}{C_p}} \right) = \quad , (1)$$

$$= 8.69\sqrt{C_p}\left(\frac{R}{2}\sqrt{\frac{1}{L}} + \frac{\omega \, tg\delta}{2}\sqrt{L} \right) = \alpha_m + \alpha_d \, , dB/m,$$

where

$$\alpha_m = 8.69\sqrt{C_p}\,\frac{R}{2}\sqrt{\frac{1}{L}}, \quad \alpha_d = 8.69\sqrt{C_p}\cdot\frac{\omega \, tg\delta}{2}\sqrt{L} \; . (2)$$

The working capacitance of the twisted pair (Fig. 1), the conductors of which are twisted with the corresponding step h, determines the losses in the conductors and in the insulation (see (2)).

$$C_p = \chi \cdot \frac{\pi \cdot \varepsilon_0 \cdot \varepsilon}{\ln\left(\frac{a-r}{r} \cdot \psi \right)}, \quad F/m, \qquad (3)$$

where χ is the twist coefficient of pair conductors to reduce electromagnetic influences, ψ is the coefficient that takes into account the effect on the working capacitance of adjacent pairs and the metal screen, a is the distance between conductors determined by the radius r_1 of the conductor (1) and insulation thickness Δ_1 (2), ε is the dielectric constant of the insulation (Fig. 1).

The working capacitance of unshielded and shielded twisted pairs is determined based on the calculation of the electric field [9-13]. For example, in [11] the working capacitance of unshielded twisted pair is determined on the basis of the application of the method of conformal mappings and finite elements in the ELCUT environment. In [12, 13] the working capacitance and the influence of the thickness of the layers of three-layer polyethylene insulation on the working capacitance of the shielded twisted pair of category 7 were determined by the method of secondary charges.

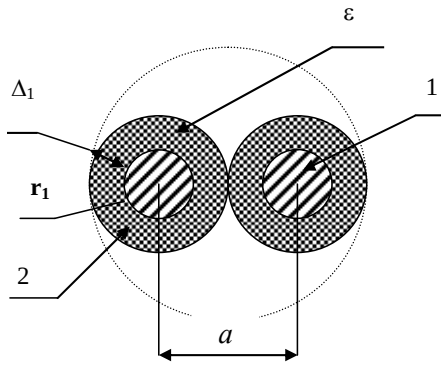

Fig. 1. Twisted pair design

At the technological stage of manufacturing an insulated conductor, as the main structural element of twisted pair, the electrical capacitance is measured. The conductor is a capacitor, one of the covers of which is a metal core of the wire, and the other one is water that cools after applying the insulation, which is in electrical contact with the tubular electrode, through which the controlled insulated conductor moves continuously. This method of control is implemented in the development of leading companies specializing in the production of control devices for the cable industry: Sikora, Zumbach (Table 3) [14, 15]. Electronic units of the measuring system are equipped with modern data ports for connection to display processors or to the main computer (local computer network) by means of industrial interfaces (cables) Profibus DP, Rs-232, -432, -485 [1].

Table 3

Technical characteristics of measuring systems of electric capacitance of cables at technological stage [14, 15]

Company	Device type	Range of diameters, mm	Range of capacitance values, pF/m	Accuracy, pF/m
Sikora	Capacitance 2010	0.5-10	0-300	±0.45
	Capacitance 2025	1-25	0-300	±0.45
Zumbach	CAPAC®	–	0-300 0-600 0-1800	±0.1 ±0.3 %

Continuous control of the electrical capacitance of the insulated conductor along its entire length allows to make timely decisions on the regulation of the capacitance at the technological stage of manufacture.

Influence of design decisions on the electrical capacitance of an insulated conductor. Based on the application of the method of secondary charges [12, 13], the electrical capacitance of the insulated conductor is determined by varying the thickness of solid and foamed polyethylene insulation, the environment in which the conductor is at the technological stage of manufacture.

Figure 2 shows the results of calculations of the electrical capacitance of an insulated conductor with constant diameter r_1 of the conductor and varying the thickness Δ_1 of solid insulation for two cases: when in air (curve 1) and in water (curve 2). The dielectric permittivity of the technical cooling water is assumed to be equal to 100 [13].

Figure 2,*a* shows the absolute values of capacitance, Fig. 2,*b* – relative values regarding the calculated capacitance in the case $r_1=\Delta_1$. At this scale, the capacitance calculations coincide for the three values of the conductor diameters $2r_1$ = 0.511; 0.57 and 0.64 mm. Curve 1 refers to the case of cooling the insulated conductor in air, curve 2 – in water.

When cooling in water, the electrical capacitance of the insulated conductor changes more than 2 times, with air cooling – no more than 5 % when varying the thickness of the solid insulation (compare curves 1 and 2, Fig. 2,*a*,*b*).

Increasing the insulation thickness by 50 % relative to the radius of the conductor (curve 2, Fig. 2,*a*,*b*) leads to a decrease in the capacitance of the insulated conductor by 20 %. Such a constructive solution causes growth of mass and dimensions of the twisted pair as a whole. A more effective design and technological solution is the use of foam insulation [12].

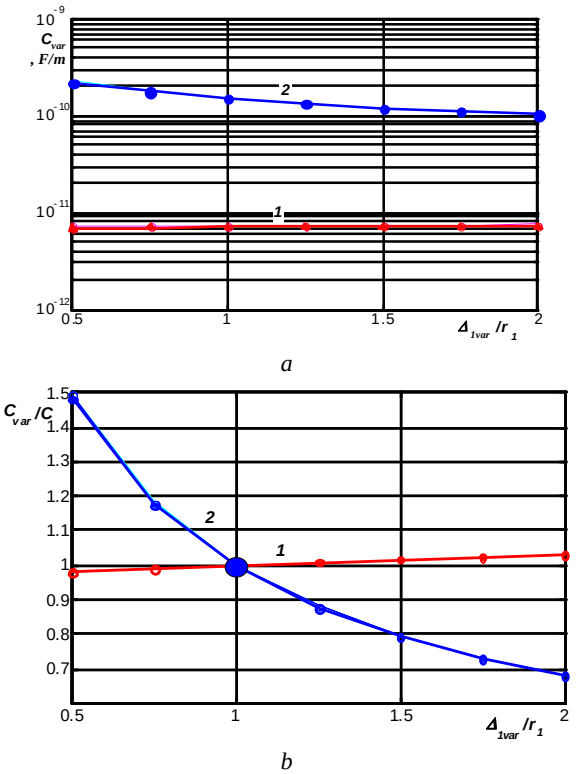

Fig. 2. Influence of solid insulation thickness on electrical capacitance of insulated conductor in air (curve 1) and water (curve 2)

Foaming insulation as an effective solution for capacitance regulation. Insulation foaming technology has recently become widely used, including in twisted pairs [12, 16-17]. The most well-known chemical foaming agent is azodicarbonamide, an exothermic chemical foaming agent. It releases a large amount of nitrogen gas into the polymer together with a smaller amount of carbon dioxide.

To calculate the effective dielectric permittivity of foam insulation, which is a statistical mixture (chaotic, disordered in space), the Lichtenecker formula [18] is used – the logarithmic law of mixing.

For a foamed mixture of two components of solid insulation based on polyethylene filled with a large number of small gas pores, the dielectric constant of which is equal to $\varepsilon = 1$, the effective dielectric permittivity ε_{foam} is determined by the dielectric permittivity of solid polyethylene ε_{PE} and the ratio of the density of foamed ρ_{foam} and solid ρ_{PE} insulation, respectively

$$\lg \varepsilon_{foam} = \frac{\rho_{foam}}{\rho_{PE}} \lg \varepsilon_{PE} . \qquad (4)$$

Figure 3 shows the dependence of the effective dielectric permittivity of foamed polyethylene insulation, the tangent of the angle of dielectric loss and the electrical capacitance of the insulated conductor on the value inverse to the degree of porosity $\frac{1}{p_{foam}} = \frac{\rho_{PE}}{\rho_{foam}}$.

At the degree of porosity of 40 % (the relative content of solid polyethylene is 60 % = Fig. 3), the dielectric permittivity of the mixture decreases in 2/1.6 = 1.25 times. Accordingly, the tangent of the dielectric loss angle decreases by 33 % and the electrical capacitance of the insulated conductor decreases by 20 %, which proves the effectiveness of the use of foam insulation.

The presence of a large number of pores in the solid polyethylene insulation requires a solution to protect the pores from moisture penetration during cable operation. The most attractive is the use of an additional continuous film on the surface of the foam insulation, which acts as a barrier to the penetration of moisture into the foam insulation [12] (Fig. 4).

The influence of the film thickness depending on the degree of porosity of the polyethylene insulation on the effective dielectric permittivity (*a*), the effective tangent of the dielectric loss angle (*b*) and the electrical capacitance (*c*) of the insulated conductor is presented in Fig. 5. Curve 1 in Fig. 5 corresponds to the solid polyethylene insulation, the thickness of which is equal to the radius of the conductor and remains unchanged when foamed Δ_{foam}. The step of the degree of foaming is equal to 0.05 (curve 11 corresponds to 50 % of the polyethylene content and 50 % of the gas pore content). The thickness of the solid protective film Δ_{solad} varies from 0.5 % to 60 % relative to the main insulation.

The use of an additional layer of solid film on the surface of the core to ensure the «rigidity» of the structure with a constant total thickness of insulation leads to an increase in the capacitance of three-layer insulation by no more than 5 % compared to two-layer insulation.

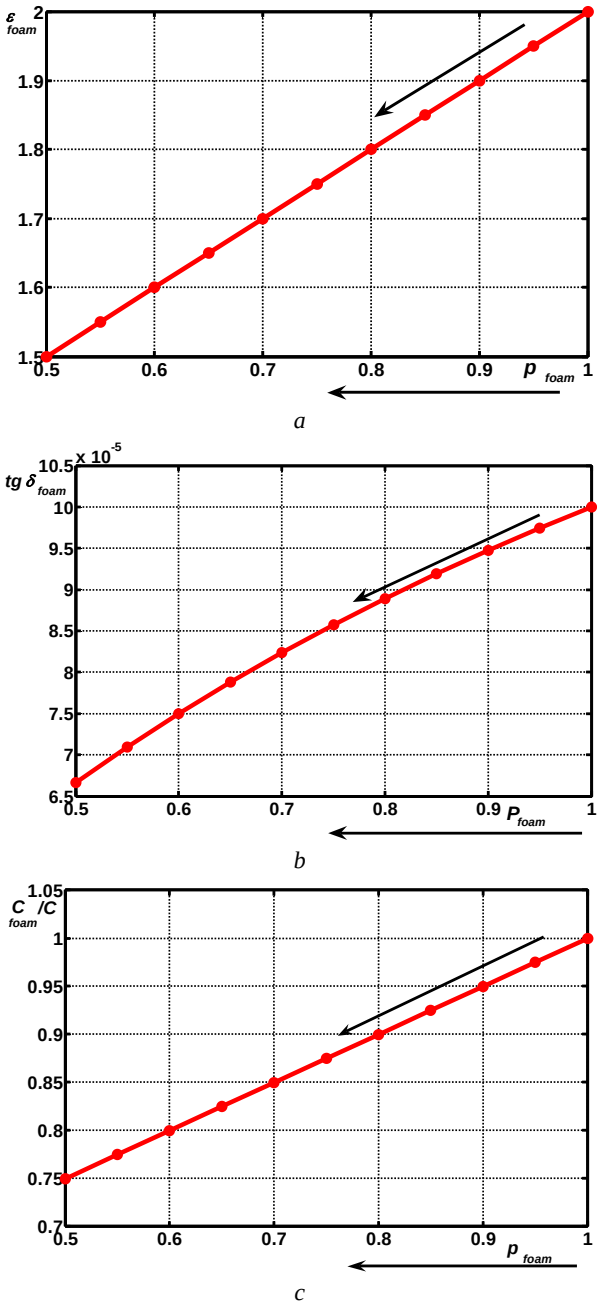

Fig. 3. The effect of the degree of porosity of polyethylene p_{foam} on the effective dielectric permittivity (*a*), effective dielectric loss tangent (*b*) and electric capacitance (*c*) of the insulated conductor

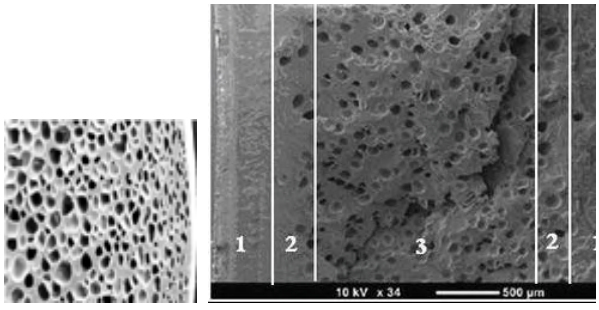

Fig. 4. Structure of foamed polyethylene insulation without protective film (*a*) and with protective polyethylene film (*b*): 1 – film, 2 – transition zone, 3 – proper foam insulation [16]

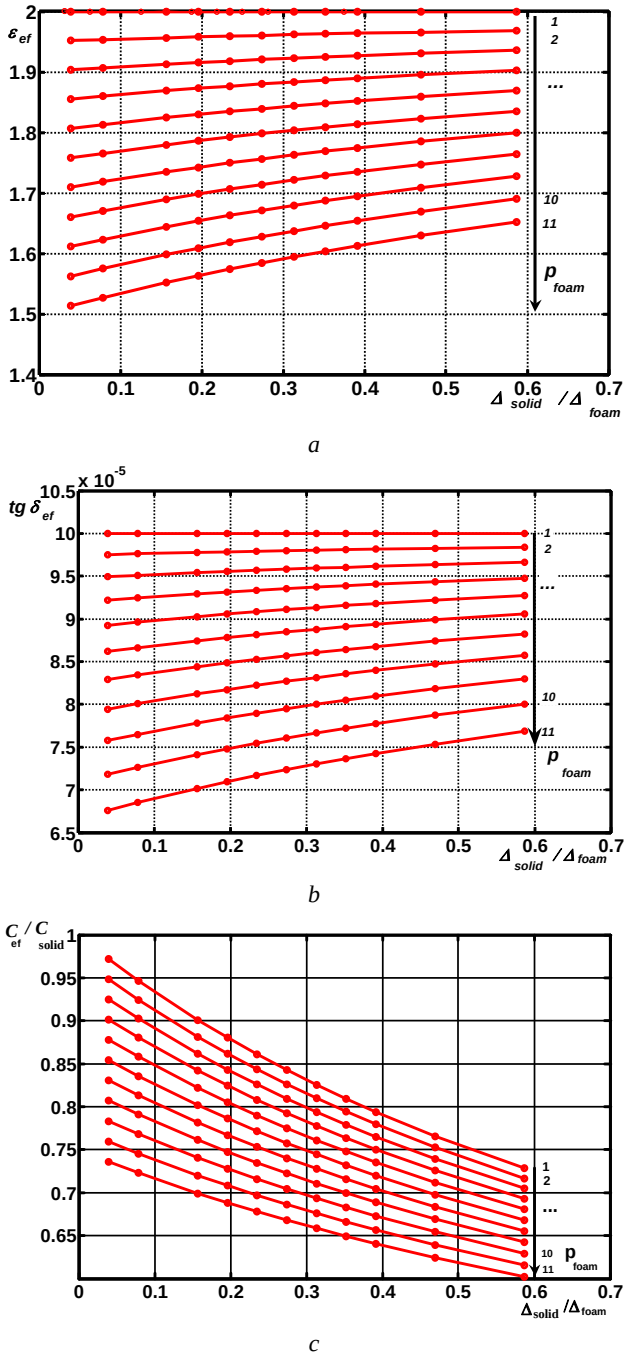

Fig. 5. 3D-diagram of the influence of the degree of porosity of polyethylene and the thickness of the protective solid polyethylene film on the electrophysical characteristics and electrical capacitance of the insulated conductor

Conclusions.

The location of the insulated conductor in the cooling water provides a high sensitivity to the settings of the technological process for regulation of the capacitance when varying the thickness of the insulation. When the insulation thickness changes 4 times relative to the diameter of the conductor, the electrical capacitance changes more than 2 times. When in the air – by 5 %.

For the first time, nomograms of effective dielectric permitivity, dielectric loss angle tangent and relative capacitance values depending on the degree of foaming of solid polyethylene insulation and protective film thickness are obtained, which allow to effectively regulate the electrical capacitance of twisted pair conductor insulation.

The methodology of synthesis of constructive-technological solutions for regulating the capacitance of twisted pair cables of industrial networks at the technological stage of manufacturing an insulated conductor is substantiated.

The developed technique can be used to adjust the technological process of manufacturing insulated conductors of cables for various purposes, including power ones.

Conflict of interests. The authors declare no conflicts of interest.

REFERENCES

1. Pigan R., Metter M. *Automating with PROFINET: Industrial Communication Based on Industrial Ethernet*. John Wiley & Sons Publ., 2015. 462 p.

2. Bezprozvannych G.V., Pushkar O.A. Increasing noise immunity of cables for fire protection systems. *Electrical Engineering & Electromechanics*, 2020, no. 4, pp. 54-58. doi: https://doi.org/10.20998/2074-272x.2020.4.07.

3. Belous A., Saladukha V. *High-Speed Digital System Design: Art, Science and Experience*. Springer Nature Publ., 2019. 933 p.

4. *International Standard ISO/IEC 11801. Information Technology – Generic cabling for customer premises. Part 2: Office premises*. 2017. 24 p.

5. Semenov A. Advanced Twisted Pair Cables for Distributed Local Area Networks in Intelligent Structure Systems. *IOP Conference Series: Materials Science and Engineering*, 2018, vol. 317, p. 012053. doi: https://doi.org/10.1088/1757-899x/317/1/012053.

6. Penttinen Jyrki T.J. *The Telecommunications Handbook: Engineering Guidelines for Fixed, Mobile and Satellite Systems*. John Wiley & Sons Publ., 2015. 1008 p.

7. *Sending all the right signals. White paper. Single pair Ethernet in the Industrial Field*. Belden, 2020. 8 p.

8. Bezprozvannych G.V., Ignatenko A.G. Optimization of the design of network cables by the attenuation coefficient in the tolerance zone of the geometric dimensions of the transmission parameters. *Electrical Engineering & Electromechanics*, 2004, no. 2. pp. 8-10. (Rus).

9. Iossel Yu.Ya., Kochanov E.S., Strunsky M.G. *Raschet elektricheskoi emkosti* [Calculation of electrical capacity]. Leningrad, Energoizdat Publ., 1981. 288 p. (Rus).

10. Levin B.M. Calculation of Electrical Parameters of Two-Wire Lines in Multiconductor Cables. *IEEE Transactions on Electromagnetic Compatibility*, 2008, vol. 50, no. 3, pp. 697-703. doi: https://doi.org/10.1109/temc.2008.927924.

11. Vishnyakov E.M., Khvostov D.V. Calculation of inter-wire inductance and capacitance of symmetric straight pairs by methods of conformal mappings and finite elements. *Cable-news*, 2007, no. 3 (13), pp. 30-36. (Rus).

12. Boyko AM, Bezprozvannych G.V. Justification of insulation thickness of twisted shielded pairs of structured cable systems. *Bulletin of NTU «KhPI»*, 2011, no. 3, pp. 21-35. (Ukr).

13. Bezprozvannych G.V. Comparative analysis of the transverse structure of unfilled and filled telephone cables based on capacity and dielectric dissipation measurement results. *Electrical Engineering & Electromechanics*, 2007, no. 5, pp. 61-66. (Rus).

14. Sikora Technology to Perfection / Capacitance 2000. Available at: https://sikora.net/en/products/capacitance2000/ (Accessed 14.09.2020).
15. Zumbach Electronics. CAPAC® / FFT / SRL – Overview. Available at: https://www.zumbach.com/ru/products/product-finder/capac-fft-srl/capac-overview.html (Accessed 14.09.2020).
16. Xu Z., Xue P., Zhu F., He J. Effects of formulations and processing parameters on foam morphologies in the direct extrusion foaming of polypropylene using a single-screw extruder. *Journal of Cellular Plastics*, 2005, vol. 41, no. 2, pp. 169-185. doi: https://doi.org/10.1177/0021955x05051740.
17. Pinto J., Notario B., Verdejo R., Dumon M., Costeux S., Rodriguez-Perez M.A. Molecular confinement of solid and gaseous phases of self-standing bulk nanoporous polymers inducing enhanced and unexpected physical properties. *Polymer*, 2017, vol. 113, pp. 27-33. doi: https://doi.org/10.1016/j.polymer.2017.02.046.
18. Palchykov O.O. Determination of the effective permittivity of a heterogeneous material. *Electrical Engineering & Electromechanics*, 2020, no. 2, pp. 59-63. doi: https://doi.org/10.20998/2074-272x.2020.2.09.

Received 10.11.2020
Accepted 06.12.2020
Published 25.02.2021

G.V. Bezprozvannych[1], *Doctor of Technical Science, Professor,*
I.A. Kostiukov[1], *Ph.D., Doctoral Student,*
O.A. Pushkar[2], *General Director, Graduate Student,*
[1] National Technical University «Kharkiv Polytechnic Institute»,
2, Kyrpychova Str., Kharkiv, 61002, Ukraine,
e-mail: bezprozvannych@kpi.kharkov.ua,
iakostiukow@gmail.com
[2] Company «Alay»,
95 A2, office 202, Otradny Ave., Kyiv, 03061, Ukraine,
e-mail: adm@alay.com.ua

How to cite this article:
Bezprozvannych G.V., Kostiukov I.A., Pushkar O.A. Synthesis of constructive-technological decisions of regulation of working capacitance of cables of industrial networks. *Electrical Engineering & Electromechanics*, 2021, no. 1, pp. 44-49. **doi: 10.20998/2074-272X.2021.1.07.**

UDC 621.3 **doi: 10.20998/2074-272X.2021.1.08**

N. Anwar, A. Hanif, M.U. Ali, A. Zafar

CHAOTIC-BASED PARTICLE SWARM OPTIMIZATION ALGORITHM FOR OPTIMAL PID TUNING IN AUTOMATIC VOLTAGE REGULATOR SYSTEMS

Introduction. *In an electrical power system, the output of the synchronous generators varies due to disturbances or sudden load changes. These variations in output severely affect power system stability and power quality. The synchronous generator is equipped with an automatic voltage regulator to maintain its terminal voltage at rated voltage. Several control techniques utilized to improve the response of the automatic voltage regulator system, however, proportional integral derivative (PID) controller is the most frequently used controller but its parameters require optimization.* ***Novelty.*** *In this paper, the chaotic sequence based on the logistic map is hybridized with particle swarm optimization to find the optimal parameters of the PID for the automatic voltage regulator system. The logistic map chaotic sequence-based initialization and global best selection enable the algorithm to escape from local minima stagnation and improve its convergence rate resulting in best optimal parameters.* ***Purpose.*** *The main objective of the proposed approach is to improve the transient response of the automatic voltage regulator system by minimizing the maximum overshoot, settling time, rise time, and peak time values of the terminal voltage, and eliminating the steady-state error.* ***Methods.*** *In the process of parameter tuning, the Chaotic particle swarm optimization technique was run several times through the proposed hybrid objective function, which accommodates the advantages of the two most commonly used objective functions with a minimum number of iterations, and an optimal PID gain value was found. The proposed algorithm is compared with current metaheuristic algorithms including conventional particle swarm optimization, improved kidney algorithm, and others.* ***Results.*** *For performance evaluation, the characteristics of the integral of time multiplied squared error and Zwe-Lee Gaing objective functions are combined. Furthermore, the time-domain analysis, frequency-domain analysis, and robustness analysis are carried out to show the better performance of the proposed algorithm. The result shows that automatic voltage regulator tuned with the chaotic particle swarm optimization based PID yield improvement in overshoot, settling time, and function value of 14.41 %, 37.91 %, 1.73 % over recently proposed IKA, and 43.55 %, 44.5 %, 16.67 % over conventional particle swarm optimization algorithms. The improvement in transient response further improves the automatic voltage regulator system stability for electrical power systems.* References 44, tables 4, figures 6.

Key words: **proportional integral derivative (PID) tuning, chaotic particle swarm optimization (CPSO), robustness analysis, automatic voltage regulator (AVR), transient response.**

Вступ. *В електроенергетичній системі потужність синхронних генераторів змінюється внаслідок збурень або різких змін навантаження. Ці зміни в потужності серйозно впливають на стабільність енергетичної системи та якість електроенергії. Синхронний генератор оснащений автоматичним регулятором напруги для підтримання напруги на його клемах на рівні номінальної напруги. Декілька методів управління використовуються для поліпшення реакції системи автоматичного регулятора напруги, однак пропорційний інтегральний похідний контролер (PID-контролер) є найбільш часто використовуваним контролером, але його параметри вимагають оптимізації.* ***Новизна.*** *У цій роботі хаотична послідовність, заснована на логістичній схемі, гібридизується за допомогою оптимізації рою частинок, щоб знайти оптимальні параметри PID для системи автоматичного регулятора напруги. Ініціалізація на основі хаотичної послідовності логістичної схеми та найкращий глобальний вибір дозволяють алгоритму вийти із локальної мінімальної стагнації та покращити швидкість збіжності, що дає найкращі оптимальні параметри.* ***Мета.*** *Основною метою запропонованого підходу є поліпшення перехідної реакції системи автоматичного регулятора напруги шляхом мінімізації максимального перевищення, часу встановлення, часу наростання та пікових значень напруги на клемах і усунення помилки у стаціонарного стані.* ***Методи.*** *У процесі настройки параметрів техніку оптимізації рою хаотичних частинок кілька разів пропускали через запропоновану гібридну цільову функцію, яка враховує переваги двох найбільш часто використовуваних цільових функцій з мінімальною кількістю ітерацій,і знайдено оптимальне значення коефіцієнту підсилення PID. Запропонований алгоритм порівнюється з сучасними метаевристичними алгоритмами, включаючи звичайну оптимізацію рою частинок, вдосконалений алгоритм нирок та інші.* ***Результати.*** *Для оцінки ефективності об'єднуються характеристики інтеграла у часі, помноженого на похибки у квадраті, та цільових функцій Цве-Лі Гейнга. Крім того, проводяться аналіз у часовій області, аналіз у частотної області та аналіз стійкості, щоб показати кращу ефективність запропонованого алгоритму. Результат показує, що автоматичний регулятор напруги, налаштований на хаотичну оптимізацію рою частинок, заснований на поліпшенні виходу PID в перевищеннях,часі налаштування та значенні функції перевищує на 14,41 %, 37,91 %, 1,73 % нещодавно запропонований нирковий алгоритм та на 43,55 %, 44,5 %, 16,67 % перевищує звичайні алгоритми оптимізації рою частинок. Поліпшення перехідної реакції ще більше покращує стабільність автоматичного регулятора напруги для систем електроенергетики.* Бібл. 44, табл. 4, рис. 6.

Ключові слова: **пропорційне регулювання інтегральної похідної, оптимізація хаотичного рою частинок, аналіз стійкості, автоматичний регулятор напруги, перехідна реакція.**

Introduction. The disturbances such as change in transmission line parameters, sudden load changes, fluctuation in the turbine output, etc., causes the synchronous generator to show an oscillatory performance around the equilibrium state [1]. Under such oscillations, the power system stability is greatly affected. To assure the power quality and to enhance the power network stability, excitation of synchronous generator is equipped with automatic voltage regulator (AVR) and power system stabilizer. AVR keeps the output voltage of synchronous generator at rated value. The transient response of AVR system extremely affects the stability of the power system [2].

A number of control methods were studied, such as predictive controls, fuzzy controls, and neural controls for process controls system. Despite much effort, proportional integral derivative (PID) controllers are the

main element of industrial controller systems and can be used in the form of embedded controller, distributed control system and programmable logic controller [3]. Overschee and Demoor stated 80 % of PID controllers are not tuned to optimal level in the industries. Furthermore, they reported that 30 % of the PID controllers operates in manual settings, whereas twenty 5 % work in the default settings [4]. Over the years, numerous techniques for tuning of PID parameters were proposed like traditional techniques including Ziegler/Nicole, Cohen/Kun, pole position and latest techniques (i.e., gains scheduling, minimum fluctuations and prediction) [5]. Some drawbacks of traditional control technique for PID controllers tuning are:

- inadequate dynamics of closed loop response;
- excessive rules for setting gains;
- mathematical complexity control design;
- difficulty in dealing with nonlinearities [6].

Therefore, in academia and industry, the tuning a PID controller is an interesting research topic.

Numerous techniques like artificial neural networks (ANN) and neural fuzzy systems were used for the tuning of PID-AVR parameters. However, these techniques require a quite large amount of data for training process [7]. On the other hand, metaheuristic optimization based tuning algorithms such as improve kidney-inspired algorithm (IKA) [8], particle swarm optimization (PSO) [9], biogeography-based optimization (BBO), local unimodal sampling algorithm (LUS) [10], artificial bee colony (ABC) algorithm [11], slap swarm algorithm (SSA) [12], artificial electric filed (AEF) [13], Harris hawks optimization (HHO) [14], sine cosine algorithm (SCA) [15], whale optimization algorithm (WOA) [16], etc., are applied for PID tuning in AVR system.

Many objective functions were proposed in literature as performance criteria for optimization of PID-AVR. The integral error is extensively used as an objective function, which is based on difference between reference and the system output. The frequently used integral functions include:

- integral absolute error (IAE);
- integral time absolute error (ITAE);
- integral squared error (ISE);
- integral time squared error (ITSE).

Minimizing the ISE and IAE provide relatively small overshoots with longer stabilization time. Alternatively, the ITSE and ITAE can overcome the limitations of the ISE and IAE, but they cannot guarantee the required stability [17]. In addition, Zwe-Lee Gaing (ZLG) defines the time step performance criterion by using a weighted factor with the parameters of time response [7].

A brief literature review of the tuning techniques applied on AVR systems over the past years is shown in Table 1, which encapsulates the performance indexes and analysis approaches used in the literature.

Genetic algorithm (GA), ABC, and PSO algorithms have tendency to solve numerous optimization problems, but affects with issues like memory capabilities, etc. Improved results might be obtained through other optimization methods, but they might have drawbacks such as initial convergence, local minimum congestion, difficulty in selecting control parameter, and increased computation time dependent on size of the studied system [18]. Also, there is no exact technique for finest parameters tuning of PID controller for AVR system. Therefore, studying novel heuristic optimization algorithms is an imperative and observable issue for researchers. Since metaheuristic algorithms have establish their place in efficiently solving numerous global optimization problem that can be applied to various scenarios, however the major problem faced by them is the premature convergence leads trapping in local optima [19]. Chaotic features diversify solution space, creating space to exploit and explore more space. Chaos phenomena can take place in a deterministic nonlinear dynamic system and is sensitive to initial conditions. Thus, chaotic movements within a certain range can travel all states without repetition. The easy implementation and its capability to escape from getting stuck in the local optima evolved in chaos based search algorithms [20]. Experimental studies argue for the benefit of using chaotic instead of random signals [21].

In this study, optimization of PID controller for AVR applications using the hybridization of chaotic initialization in particle swarm optimization (CPSO) is proposed. The combined ITSE and ZLG performance criterion is used. The ITSE-ZLG not only minimize the steps response characteristic that are settling time (t_s), peak time (t_p), rise time (t_r), overshoot (%MP), and steady state errors (e_{ss}), but also the average of time weighted absolute errors between the measured and rated voltage. The results obtained on the basis of the proposed technique are then compared with existing techniques algorithm in the literature. To show the supremacy of the proposed CPSO-PID approach, transient response analysis, frequency response analysis and pole-zero map under AVR system parameters changes are performed. At the end, the robustness analysis is performed.

Mathematical model of AVR. To maximize the power quality of system, AVR is crucial in maintaining the terminal output voltage of synchronous generator to predefined level through generator exciter control. Operation of AVR is dependent upon the difference between pre-defined voltage levels to variable terminal voltage level, which may arise due to disturbance in power network. Excitation mechanism serves the purpose to maintain the generator terminal voltages in case of system interruptions. Potential transformer measure's the voltage magnitude, afterwards rectified and compared with the reference. Error signal generated through this mechanism is amplified to control the field excitation, hence maintain the synchronous generator terminal voltage. Generation of reactive power increases/decreases to new stable equilibrium, maintaining the output voltage to defined rated value. Modelling of various parts of AVR system is given in the following equations:

$$G_{Amplifier}(s)=\frac{K_A}{1+s\cdot T_A};\qquad (1)$$
$$0.02\le T_A\le 0.1,\quad 10\le K_A\le 40;$$

$$G_{Exciter}(s)=\frac{K_E}{1+s\cdot T_E};\qquad (2)$$
$$0.4\le T_E\le 1,\quad 1\le K_E\le 10;$$

Table 1

Tuning method for automatic voltage regulator system

Reference	Proposed algorithm	Comparison	Performance indices						Analysis methods			
			IAE	ISE	ITAE	ITSE	ZLG	Other	Transient response	Pole Zero Map	Frequency response	Robustness
Ekinci et al. [8]	IKA	PSO, DE, ABC, LUS, PSA, BBO, GOA				+	+		+	+	+	+
Ekinci et al. [14]	HHO	BBO				+			+			+
Demirören et al. [13]	AEF	PSO, BBO				+			+			
Mosaad et al. [16]	WOA	BA, CSA, FPA, PSO, SCA, WWO			+				+			
Çelik et al. [22]	SOS	ABC, MOL, BBO			+			+	+	+	+	+
George et al. [23]	WCA	WOA, GA						+	+			
Çelik et al. [24]	SFS	ABC, MOL, LUS, WCO, GSA, BBO				+			+	+	+	+
Ekinci et al. [12]	SSA	ABC, ZN				+			+		+	
Odili et al. [25]	ABO	PSO, GA ACO, BFOA	+						+			
Bingul et al. [26]	CS	PSO, MOL, ABC, BF-GA, LUS			+	+		+	+	+	+	+
Hekimoglu et al. [15]	SCA	ZN, DE, ABC, BBO					+		+	+	+	+
Kansit et al [27]	PSOGSA	ZN, PSO, MOL			+				+			
Chatterjee et al. [28]	TLBO	GA, PSO, LUS, PSO, ABC			+	+	+		+	+	+	+
Guvenc et al. [29]	BBO	ABC, DEA, PSO				+			+	+	+	+
Sahib et al. [9]	PSO	ABC, DEA, GA, MOL, LUS			+				+	+	+	+
Mohantya et al. [10]	LUS	ABC, PSO, DE				+		+	+		+	+
Tang et al. [30]	CAS	PSO					+		+			
Gozde et al. [31]	ABC	PSO, DEA				+			+	+	+	+

In Table 1 the following abbreviation is used: IKA –improved kidney-inspired algorithm, SSA – slap swarm algorithm, SOS – symbiotic organisms search, SFS – stochastic fractal search, CAS – Chaotic ant swarm, ABO – African buffalo optimization, WWO – water wave optimization, TLBO – teaching learning based optimization, CS – cuckoo search, water wave optimization, PSO – particle swarm optimization, DE – differential evolution, ABC – ant bee colony, LUS – local unimodal sampling, PSA – pattern search algorithm, BBO – bio-geography-based optimization, GOA – grasshopper optimization algorithm, GA – genetic algorithm, MOL – many optimizing liaisons, ZN – ziegler-nichols, WCO – world cup optimization, GSA – gravitational search algorithm, WCA – water cycle algorithm , WOA – whale optimization algorithm, ACO – ant colony optimization, BFOA – bacterial foraging optimization Algorithm, CSA – crow search algorithm, BA – bat algorithm, FPA – flower pollination algorithm, SCA – sine cosine algorithm, BF-GA – hybrid genetic algorithm and bacterial foraging.

$$G_{Generator}(s)=\frac{K_G}{1+s\cdot T_G}; \quad (3)$$

$$1\le T_G\le 2,\quad 0.7\le K_G\le 1;$$

$$G_{Sensor}(s)=\frac{K_S}{1+s\cdot T_S}; \quad (4)$$

$$0.001\le T_S\le 0.06,\quad 1\le K_S\le 2;$$

where K_A, K_E, K_G and K_S are the amplifier, exciter, generator and sensor gains respectively, T_A, T_E, T_G and T_S are the amplifier, exciter, generator and sensor time constant respectively.

The linearized AVR transfer function system without PID is given as follows:

$$\frac{\Delta U(s)}{\Delta U_{ref}(s)}= \quad (5)$$

$$=\frac{K_A\cdot K_E\cdot K_G\cdot(1+s\cdot T_S)}{(1+s\cdot T_A)\cdot(1+s\cdot T_E)\cdot(1+s\cdot T_G)\cdot(1+s\cdot T_S)+K_A\cdot K_E\cdot K_G\cdot K_S}.$$

AVR system with PID controller. The PID controller consists of 3 main control actions/gains with respect to the error signal:

1) proportional (K_p) control;
2) integral (K_i) control;
3) derivative (K_d) control.

In industrial control processes, a constant gain PID controller has been extensively used. PID controller transfer function is given as

$$U_c(t) = K_p \Delta U_e(t) + K_i \int_0^t \Delta U_e(t) dt + K_d \left(d\Delta U_e(t) \right) / dt, \quad (6)$$

where U_c is the control signal; $\Delta U_e(s)$ is the error signal among reference $\Delta U_{ref}(s)$ and measured signal $\Delta U(s)$, and K_p, K_d and K_i are the control gains of proportional, derivative and integral term, respectively.

The closed loop AVR transfer function with PID is derived as

$$\frac{\Delta U(s)}{\Delta U_{ref}(s)} = \frac{K_A \cdot K_E \cdot K_G \cdot (1 + s \cdot T_S) \cdot \left(s^2 \cdot K_d + s \cdot K_p + K_i \right)}{A}, \quad (7)$$

where

$$A = s \cdot (1 + s \cdot T_A) \cdot (1 + s \cdot T_E) \cdot (1 + s \cdot T_G) \cdot (1 + s \cdot T_S) + K_A \cdot K_E \cdot K_G \cdot K_S \cdot \left(s^2 \cdot K_d + s \cdot K_p + K_i \right).$$

The challenge in PID tuning is to determine the optimum parameters to reduce the time domain characteristics like t_r, t_s, t_p and $\%M_p$. Therefore, optimization of PID tuning parameters is required using optimization methods.

PID parameters optimization for AVR system.

Particle Swarm Optimization (PSO) is a population based optimization algorithm inspired from social behaviors of bird flocking [9]. In this algorithm, population (known as particle) is initialized. In n-dimension given problem, N particles are travelling in the solution space. The $X_j(t) = (X_{j1}, X_{j2}, ..., X_{jm})$ denotes the location of the j-th particle at the i-th iteration and $X_{jm} \in [L_m, U_m]$, $1 \le m \le N$, where L_m and U_m represents the lower and upper bound having values [0.2 – 2] respectively. The $P_j = (P_{j1}, P_{j2}, ..., P_{jm})$ denotes the best position searched by the j-th particle known as P_{best}. Finally, the global best position achieved by the swarm is identified as global best G_{best} and represented as $P_g = (P_{g1}, P_{g2}, ..., P_{gm})$. The velocity vector at the i-th iteration is $v_j(t) = (v_{j1}, v_{j2}, ..., v_{jm})$. Finally, the updated velocity and position variables of the particle for succeeding iteration are obtained as

$$V_j(t+1) = W \cdot V_j(t) + r_1 \cdot C_1 \cdot \left(P_{best\,j}(t) - x_j(t) \right) + r_2 \cdot C_2 \cdot \left(G_{best\,j}(t) - x_j(t) \right), \quad (8)$$

$$x_j(t+1) = x_j(t) + V_j(t), \quad (9)$$

where the parameter C_1 and C_2 are acceleration coefficient, W is called inertia weight (i.e., set to 1 in the conventional PSO), r_1 and r_2 represents random number between [0, 1].

The PSO algorithm has several advantages including fast convergence, less complex computations unlike GA (e.g. coding/decoding, mutation and crossover), easy to compute and simple to implement [32]. But, PSO has drawbacks, such as easily stuck in local optima and decrease in the convergence rate in the later period of evolution [33].

Chaotic Particle Swarm Optimization (CPSO).

Generating random sequences with good uniformly is very important in the field of sampling, numerical analysis and metaheuristic optimization. The concept of using chaotic sequence instead of random sequence have been emerged in research fields using chaotic neural network (CNN) [34] and chaos optimization [35], etc. Chaos is a random movement of particles having characteristics of pseudo-randomness, ergodicity, and regularity determined through a deterministic equation [36]. A chaotic signal can cross every state in a certain search region in such a way that every state is visited only once. The diversity of random numbers generated by chaotic motion is better than the randomly generated values. Chaos search has a very special ability to improve the diversity of particle in search space that helps the optimization algorithm to escape from stucking in local optima [37]. Therefore, using chaotic sequences in evolutionary algorithms is a promising approach to obtain high quality solutions. Different kinds of chaos maps have been used in literature [38].

In this paper, to improve the searching performance and to escape from trapping into local minima, chaos dynamics is integrated into the PSO. The conventional PSO algorithm faces up to premature convergence because information can be exchanged between particles quickly and the particles are getting near to each other rapidly, especially in case of problems with multiple local optima. Thus, the dispersion of particles decreases in the search space and it is difficult to escape from local optima [39]. In order to increase a population's diversity in conventional PSO, chaos sequences were used to initialize the particles' population and velocity. In this paper, chaotic sequence is generated using the logistic equation [40]. The process of initializing using logistic chaotic map is defined through the subsequent equation [41]:

$$Cx_j^{(i+1)} = 4 \cdot Cx_j^{(i)} \cdot \left(1 - Cx_j^{(i+1)} \right), \quad j = 1, 2, ..., m, \quad (10)$$

where Cx_j is the j-th chaotic variable and i denotes the number of iteration.

The procedure of chaotic search using logistic map is as follows [42].

Step 1: Setting $i = 0$ and maps the decision variables x_j^i to chaotic variable $Cx_j^{(i)}$ positioned in the interval (0, 1) using below equation

$$Cx_j^{(i)} = \frac{x_j^{(i)} - x_{\min,\,j}}{x_{\max,\,j} - x_{\min,\,j}}, \quad j = 1, 2, 3, ..., n. \quad (11)$$

Step 2: Calculating the chaotic variable $Cx_j^{(i+1)}$ for the succeeding iteration using logistic map equation according to $Cx_j^{(i)}$.

Step 3: Adapting the chaotic variable $Cx_j^{(i+1)}$ to decision variable $x_j^{(i+1)}$ using below equation

$$x_j^{(i+1)} = x_{\min,\,j} + Cx_j^{(i+1)} \cdot \left(x_{\max,\,j} - x_{\min,\,j}\right), \quad j = 1, 2, 3, \ldots, n. \tag{12}$$

Step 4: Calculating the new solution with decision variable $x_j^{(i+1)}$.

Step 5: If the new solution is superior to the previous decision variable or predefines maximum number of iterations is reached, take the new solution as the new result of chaos search else, let $i = i + 1$ and go back to Step 2.

Another improvement in conventional PSO lies in using the adaptive parameters (W, C_1, C_2) instead of constant values using the following equations

$$W = W_i - \frac{W_i - W_f}{MaxGen} \cdot Gen, \quad \left(W_i > W_f\right); \tag{13}$$

$$C_1 = C_{1i} - \frac{C_{1i} - C_{1f}}{MaxGen} \cdot Gen, \quad \left(C_{1i} > C_{1f}\right); \tag{14}$$

$$C_2 = C_{2i} - \frac{C_{2i} - C_{2f}}{MaxGen} \cdot Gen, \quad \left(C_{2i} > C_{2f}\right); \tag{15}$$

$C_{1i} = 2$, $C_{1f} = 1$, $C_{2i} = 2$, $C_{2f} = 1$, $W_i = 0.9$ and $W_f = 0.4$, where *Gen* is the current generation of the swarm, *MaxGen* is the maximum evolutionary generation, the indexes *i* and *f* denotes initial and final, respectively.

Fig. 1 shows the flow chart of CPSO.

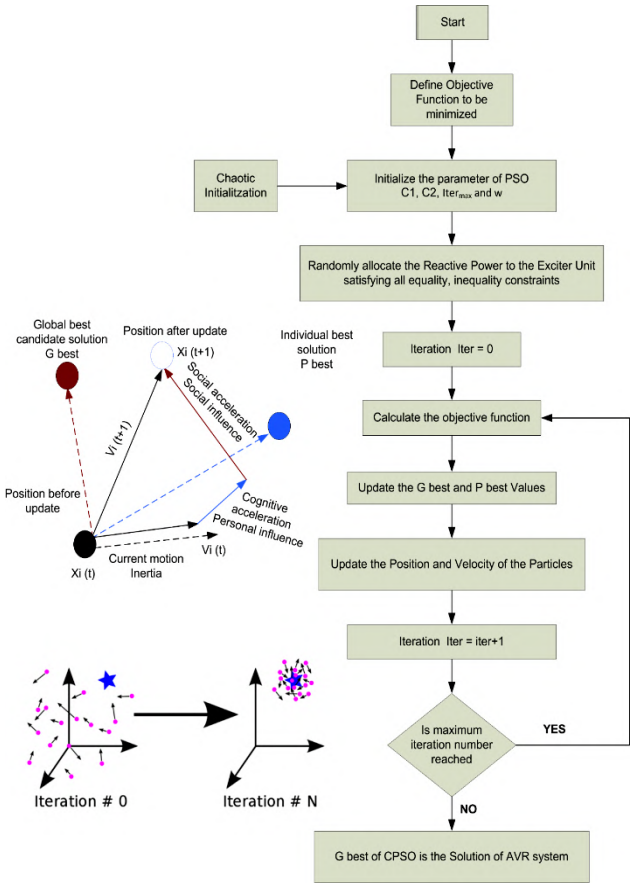

Fig. 1. Flow chart chaotic particle swarm optimization

Performance evaluation criterion. Several performance criterions were proposed in the literature to examine the performance of the AVR system [43]. The most of the criterions were associated with improvement in time domain parameters such as $\%M_p$, e_{SS}, t_r and t_S of the step response [44]. The frequently used criterions for the performance evaluation of AVR system are

1) Integral absolute error (*IAE*):

$$IAE = \int_0^{t_{sim}} \left|\Delta U_t(t)\right| dt; \tag{16}$$

2) Integral squared error (*ISE*):

$$ISE = \int_0^{t_{sim}} \left(\Delta U_t(t)\right)^2 dt; \tag{17}$$

3) Integral time weighted absolute error (*ITAE*):

$$ITAE = \int_0^{t_{sim}} t \cdot \left|\Delta U_t(t)\right| dt; \tag{18}$$

4) Integral time weighted squared error (*ITSE*)

$$ITSE = \int_0^{t_{sim}} t \cdot \left(\Delta U_t(t)\right)^2 dt; \tag{19}$$

5) Zwe-Lee Gaing (ZLG):

$$ZLG = \left(1 - e^{-\beta}\right) \cdot \left(M_p - e_{ss}\right) + e^{-\beta} \cdot \left(t_s - t_r\right), \tag{20}$$

where $\Delta U_t(t)$ is the difference between steady state value and its present terminal voltage; t_{sim} is the simulation time duration; β is the weighted factor and its values ranges between [0.5 – 1.5].

In the abovementioned criterions, ITSE and ZLG are frequently reported and resulted in improved results. ITSE resulted in high overshoot, whereas ZLG increase the rise and peak time. In this study, combined ITSE and ZLG are used [19]

$$J = ITSE + \alpha \cdot ZLG, \tag{21}$$

where α is the weighting factor to balance the *ITSE* and *ZLG* performance criterions and its values ranges between [30 – 50].

The above criterion can be changed in to optimization problem with constrained as

$$\min J\left\{ITSE, \%M_p, e_{ss}, t_s, t_r\right\};$$
$$\text{subject to} \begin{cases} 0.2 \le K_p \le 2; \\ 0.2 \le K_i \le 2; \\ 0.2 \le K_d \le 2. \end{cases} \tag{22}$$

The optimal values of free parameters ($ITSE^*$, $\%M_p^*$, e_{SS}^*, t_s^* and t_r^*) are estimated using CPSO. Fig. 2 shows the complete implementation of CPSO for AVR.

Simulation result and discussion. The different analyses were performed including convergence, pole zero map, robustness etc. to show the improved performance of CPSO-AVR. Furthermore, the voltage response analysis is also carried out by considering different cases. All the analysis were done using MATLAB/Simulink (2018 Version) on an Intel i3, processor 1.90 GHz with a RAM 4.00 GB. The population size and maximum iteration for the analysis were chosen as 30. Subsequent sections show the important results after analysis.

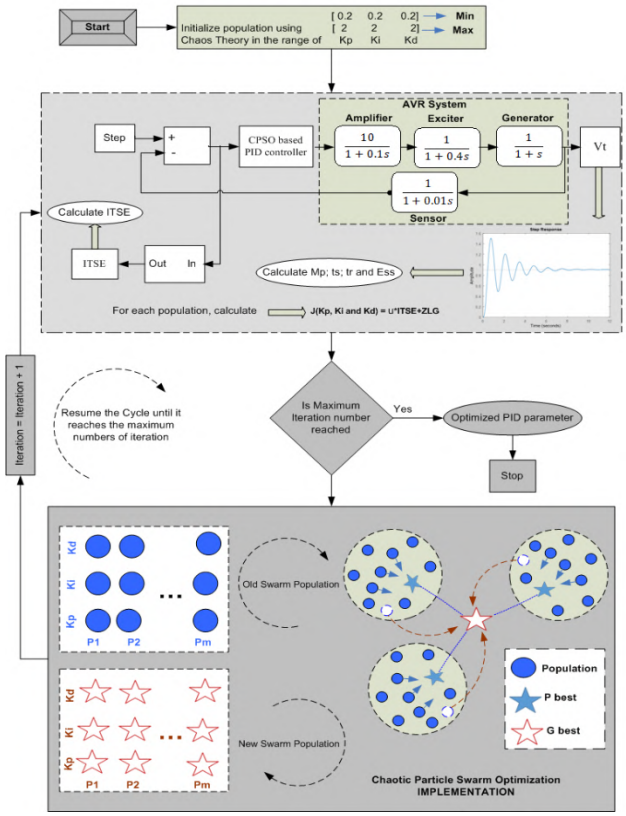

Fig. 2. Chaotic particle swarm optimization implementation

Convergence profile. The convergence curve of PSO and CPSO is shown in Fig. 3. The CPSO algorithm converges to optimized values only in 5 iterations as compared to PSO. Optimized value of PID gains obtained using CPSO were

K_p = 1.0535, K_i = 1.0112 and K_d = 0.3752.

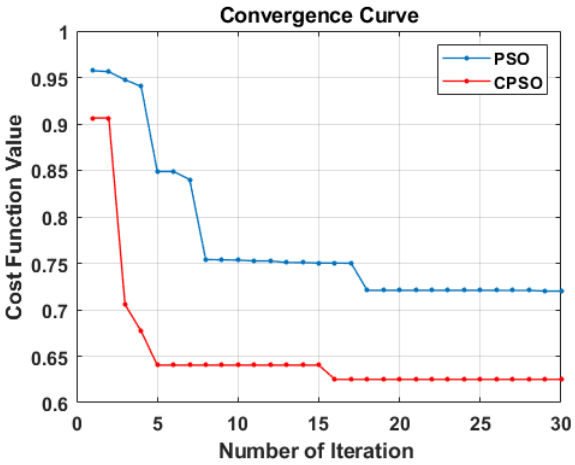

Fig. 3. Convergence curve

Equation (23) shows the overall transfer function of AVR system obtained with these optimized values

$$PID_{optim} = \frac{\Delta U_t(s)}{\Delta U_{ref}(s)} = \tag{23}$$

$$= \frac{0.0599s^3 + 6.103s^2 + 10.53s + 10.09}{0.0004s^5 + 0.0454s^4 + 0.55s^3 + 7.509s^2 + 11.43 \cdot s + 10.09}$$

Comparative analysis with different algorithms. Comparison of obtained results using CPSO with other optimization algorithms were done to show the effectiveness and supremacy of the CPSO technique. The other algorithms used to optimize the PID parameter for AVR system include IKA, PSO, BBO, LUS, ABC, SSA, AEF and HHO. In order to evaluate the performance, the time domain characteristics $\%M_p$, e_{SS}, t_r and t_S of the transient response as well as value of the criterion were compared. The comparative analysis of CPSO-PID with other meta-heuristic techniques is tabulated in Table 2. The percentage improvement of CPSO over other optimization algorithms is also reported in Table 2. It is important to note here that PID controller tuned with CPSO algorithm using the cost function given in Eq. (21) for AVR system will result in less oscillatory and stable response. Fig. 4 shows the simulation result of step response of AVR terminal voltage obtained from different algorithms. It is noted that the CPSO yields better results as compared to other algorithm.

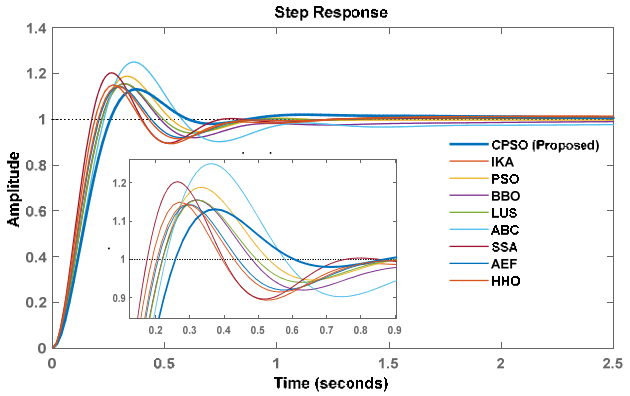

Fig. 4. Comparative analysis of step responses

Pole-Zero and frequency response Analysis. The pole-zero map helps to determine the system stability and provide the information about the position of closed-loop zeros, poles and their resultant damping ratio (DR). To check the stability of AVR, the analysis of pole-zeros and bode-plot were done with tuned controller parameters obtained using CPSO. From pole/zero analysis for CPSO-AVR, the closed loop poles are

$s_1 = -101$, $s_{2,3} = -4.94 \pm j8.65$, $s_{4,5} = -1.3 \pm j0.91$

as shown in Fig. 5 and the corresponding DR values are 1.00, 0.49 and 0.81, respectively.

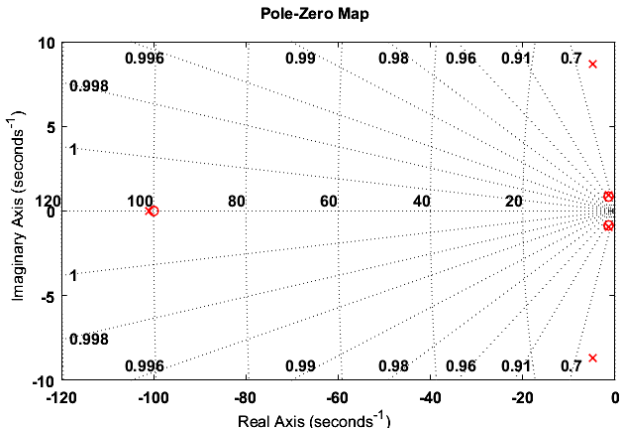

Fig. 5. Pole-zero analysis of chaotic particle swarm optimization based automatic voltage regulator

Table 2

Comparative analysis of chaotic particle swarm optimization-PID with other meta-heuristic algorithms

Controller type	PID parameters			Transient response parameters				Objective function			Improvement contributed by CPSO-PID		
	K_p	K_i	K_d	$\%M_p$	t_s, s	t_r, s	t_p, s	*ITSE*	*ZLG*	*ITSE+ZLG*	$\%M_p$	t_s, s	*ITSE+ZLG*
CPSO-PID (Proposed)	1.0535	1.0112	0.3752	13.11	0.564	0.1743	0.3732	0.0078	0.2299	0.6214	–	–	–
IKA-PID	1.0426	1.0093	0.599	15.00	0.753	0.128	0.328	0.0062	0.3246	0.6322	14.41	37.91	1.73
PSO-PID	1.3541	0.9266	0.4378	18.82	0.815	0.149	0.328	0.0072	0.3668	0.7250	43.55	44.50	16.67
BBO-PID	1.2464	0.5893	0.4596	15.52	1.446	0.149	0.317	0.0078	0.5774	0.9656	18.38	156.38	55.39
LUS-PID	1.2012	0.9096	0.4593	15.56	0.800	0.149	0.322	0.0064	0.3378	0.6577	18.68	41.84	5.84
ABC-PID	1.6524	0.4083	0.3654	25.01	3.094	0.156	0.360	0.0177	1.2430	2.1295	90.77	448.58	242.69
SSA-PID	1.3381	1.1204	0.6361	20.30	0.690	0.119	0.263	0.0056	0.3407	0.6203	54.84	22.34	0.25
AEF-PID	1.1062	0.9543	0.5178	14.30	0.7760	0.140	0.291	0.0060	0.3300	0.6302	9.07	37.58	1.41
HHO-PID	1.0887	0.9882	0.5361	14.42	0.7657	0.137	0.290	0.0060	0.3223	0.6227	9.99	35.76	0.20

Table 3 shows the values of peak-gain, phase margin, delay margin, and bandwidth for different algorithms using Bode analysis. The peak gain for CPSO-AVR is found as 0.79 dB (7.11 rad/s), whereas phase margin and delay margin are 95.8 and 0.178s (9.38 rad/s), respectively. Finally, the bandwidth is 12.267 as shown in Table 3. From the aforementioned analysis, the CPSO-AVR yielded stable and good frequency response as all closed loop poles were in the left half s-plan.

Robustness analysis. To evaluate the robustness of CPSO-AVR, time constant of exciter, amplifier, sensor and generator were varied between –50 % to +50 % as shown in Fig. 6. The results of transient response after the variations in AVR parameters are listed in Table 4. It is observed in Table 4 that the total deviation range for different values of parameters of AVR time constants are in acceptable range showing the robustness of AVR system with CPSO algorithm.

Table 3

Peak-gain, phase-margin (deg.), delay-margin and bandwidth of automatic voltage regulator system

Controller	Peak-gain	Phase-margin (deg.)	Delay-margin	Bandwidth
CPSO-PID (Proposed)	0.79 dB (7.11 rad/s)	95.8	0.178 s (9.38 rad/s)	12.267
IKA-PID	1.78 dB (10.6 rad/s)	76.7	0.095 s (14.0 rad/s)	16.785
PSO-PID	1.79 dB (8.29 rad/s)	79.3	0.121 s (11.5 rad/s)	13.915
BBO-PID	1.56 dB (8.65 rad/s)	81.6	0.112 s (11.7 rad/s)	14.284
LUS-PID	1.43 dB (8.59 rad/s)	83.2	0.126 s (11.6 rad/s)	14.208
ABC-PID	2.87 dB (7.52 rad/s)	69.4	0.111 s (10.9 rad/s)	12.880
SSA-PID	1.51 dB (9.7 rad/s)	80.8	0.11 s (12.9 rad/s)	15.624
AEF-PID	1.45 dB (9.45 rad/s)	81.8	0.114 s (12.5 rad/s)	15.286
HHO-PID	1.51 dB (9.7 rad/s)	80.8	0.11 s (12.9 rad/s)	15.624

Table 4

Robustness analysis of chaotic particle swarm optimization-PID for deviation in parameters of AVR system

Model parameter	Performance parameter	Rate of change (%)				Range of total deviation
		–50	–25	+25	+50	
T_A	Peak value (p.u.)	1.168	1.799	1.172	1.206	0.066
	t_s, s	0.2402	0.4793	1.3530	1.4793	1.620
	t_r, s	0.1601	0.1652	0.1846	0.1943	0.114
	t_p, s	0.3157	0.3445	0.4104	0.4285	0.148
T_E	Peak value (p.u.)	1.135	1.130	1.13	1.143	0.010
	t_s, s	0.6548	0.7419	1.5231	1.6749	1.969
	t_r, s	0.1155	0.1465	0.2006	0.2257	0.294
	t_p, s	0.2421	0.3011	0.4444	0.5156	0.381
T_G	Peak value (p.u.)	1.230	1.168	1.107	1.943	0.717
	t_s, s	1.0112	0.7536	1.8619	2.1511	2.814
	t_r, s	0.1059	0.1409	0.2076	0.2414	0.384
	t_p, s	0.2356	0.3002	0.4451	0.5341	0.431
T_S	Peak value (p.u.)	1.112	1.121	1.140	1.151	0.017
	t_s, s	0.5660	0.5652	1.1758	1.1977	1.123
	t_r, s	0.1791	0.1769	0.1724	0.1702	0.027
	t_p, s	0.3717	0.3813	0.3649	0.3760	0.021

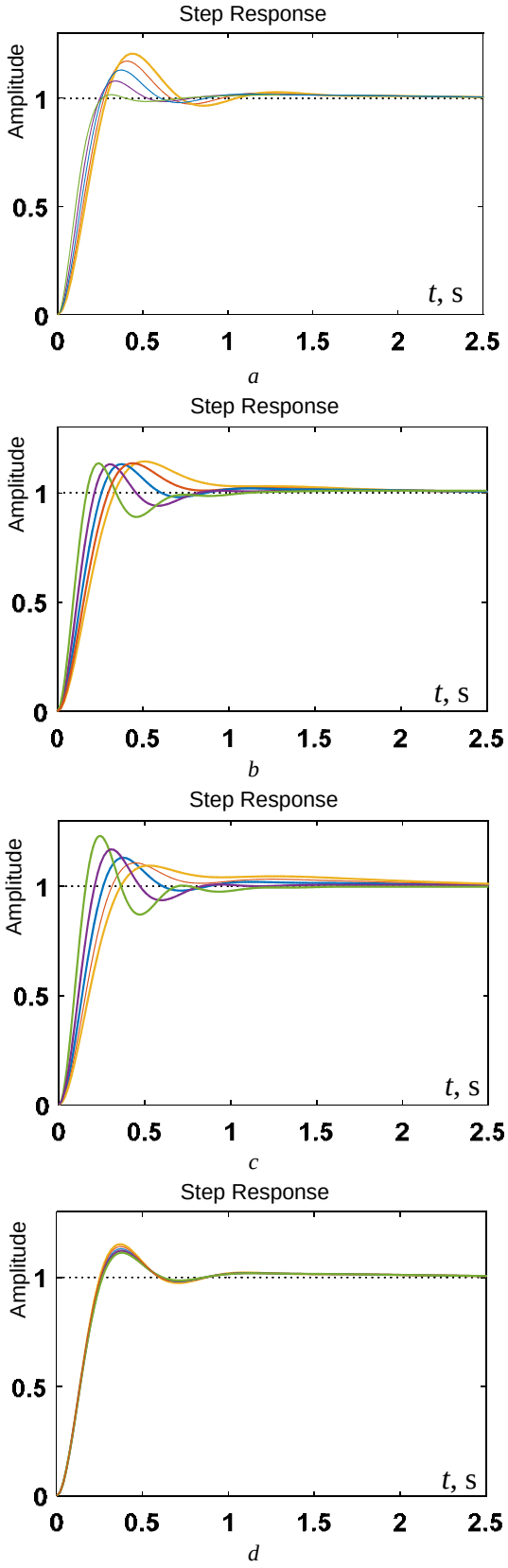

Fig. 6. Step response for variation between +50 to –50 in T_E (*a*), T_A (*b*), T_G (*c*), and T_S (*d*)

Conclusions.

In this paper, chaotic particle swarm optimization based proportional integral derivative (PID) controller was used for the optimal tuning of automatic voltage regulator system. The logistic map chaotic sequence-based initialization and global best selection enables the algorithm to escape from local minima stagnation and improve its convergence rate and resulting precision. In the process of parameter tuning, the chaotic particle swarm optimization technique was run several times through the proposed objective function, which accommodates the advantages of the two most commonly used objective functions with a minimum number of iterations, and an optimal PID gain value was found. Automatic voltage regulator system with chaotic particle swarm optimization based PID controller minimizes the performance criterion value to obtained optimized parameters of PID. Performance comparisons were performed with 8 optimization algorithms (improved kidney algorithm, particle swarm optimization, bio-geography based optimization, local unimodal sampling, artificial bee colony, slap swarm algorithm, artificial electric filed, and Harris hawks optimization) to demonstrate the usefulness of the chaotic particle swarm optimization based PID for automatic voltage regulator system.

The comparative analysis of results revealed that the proposed chaotic particle swarm optimization based PID controller based system showed an excellent transient response in terms of t_s, $\%M_p$ and performance criterion value. In addition, bode analysis, pole-zero and robustness analysis were done to show the system stability optimized by the chaotic particle swarm optimization algorithm. The analyses depict that the stability of automatic voltage regulator system is good and the proposed controller is less affected the possible variations in the parameters of the system. The proposed chaotic particle swarm optimization technique can be implemented to tune the controllers for the swing-up and stabilization for a pendulum-cart system.

Conflict of interests. The authors declare no conflicts of interest.

REFERENCES

1. Tu G., Li Y., Xiang J. Analysis, Control and Optimal Placement of Static Synchronous Compensator with/without Battery Energy Storage. *Energies*, 2019, vol. 12, no. 24, p. 4715. doi: https://doi.org/10.3390/en12244715.

2. Tang Y., Cui M., Hua C., Li L., Yang Y. Optimum design of fractional order PIλDμ controller for AVR system using chaotic ant swarm. *Expert Systems with Applications*, 2012, vol. 39, no. 8, pp. 6887-6896. doi: https://doi.org/10.1016/j.eswa.2012.01.007.

3. Kumar M.S., Mahadevan K. Removal of Moisture Content in Paper Machine Using Soft Computing Techniques. *Circuits and Systems*, 2016, vol. 07, no. 09, pp. 2542-2550. doi: https://doi.org/10.4236/cs.2016.79220.

4. Bahgaat N.K., Moustafa Hassan M.A. Swarm Intelligence PID Controller Tuning for AVR System. *Studies in Fuzziness and Soft Computing*, 2016, pp. 791-804. doi: https://doi.org/10.1007/978-3-319-30340-6_33.

5. Åström K.J., Hägglund T. Revisiting the Ziegler–Nichols step response method for PID control. *Journal of Process Control*, 2004, vol. 14, no. 6, pp. 635-650. doi: https://doi.org/10.1016/j.jprocont.2004.01.002.

6. Wojsznis W.K., Blevins T.L. Evaluating PID adaptive techniques for industrial implementation. *In Proceedings of the 2002 American Control Conference (IEEE Cat. No.CH37301)*, 2002, p. 1151. doi: https://doi.org/10.1109/acc.2002.1023174.

7. Gaing Z.-L. A Particle Swarm Optimization Approach for Optimum Design of PID Controller in AVR System. *IEEE*

Transactions on Energy Conversion, 2004, vol. 19, no. 2, pp. 384-391. doi: https://doi.org/10.1109/tec.2003.821821.
8. Ekinci S., Hekimoglu B. Improved Kidney-Inspired Algorithm Approach for Tuning of PID Controller in AVR System. *IEEE Access*, 2019, vol. 7, pp. 39935-39947. doi: https://doi.org/10.1109/access.2019.2906980.
9. Sahib M.A. A novel optimal PID plus second order derivative controller for AVR system. *Engineering Science and Technology, an International Journal*, 2015, vol. 18, no. 2, pp. 194-206. doi: https://doi.org/10.1016/j.jestch.2014.11.006.
10. Mohanty P.K., Sahu B.K., Panda S. Tuning and Assessment of Proportional–Integral–Derivative Controller for an Automatic Voltage Regulator System Employing Local Unimodal Sampling Algorithm. *Electric Power Components and Systems*, 2014, vol. 42, no. 9, pp. 959-969. doi: https://doi.org/10.1080/15325008.2014.903546.
11. Gozde H., Taplamacioglu M.C. Comparative performance analysis of artificial bee colony algorithm for automatic voltage regulator (AVR) system. *Journal of the Franklin Institute*, 2011, vol. 348, no. 8, pp. 1927-1946. doi: https://doi.org/10.1016/j.jfranklin.2011.05.012.
12. Ekinci S., Hekimoglu B., Kaya S. Tuning of PID Controller for AVR System Using Salp Swarm Algorithm. *2018 International Conference on Artificial Intelligence and Data Processing (IDAP)*, Sep. 2018. doi: https://doi.org/10.1109/idap.2018.8620809.
13. Demiroren A., Hekimoglu B., Ekinci S., Kaya S. Artificial Electric Field Algorithm for Determining Controller Parameters in AVR system. *2019 International Artificial Intelligence and Data Processing Symposium (IDAP)*, Sep. 2019. doi: https://doi.org/10.1109/idap.2019.8875972.
14. Ekinci S., Hekimoglu B., Eker E. Optimum Design of PID Controller in AVR System Using Harris Hawks Optimization. *2019 3rd International Symposium on Multidisciplinary Studies and Innovative Technologies (ISMSIT)*, Oct. 2019. doi: https://doi.org/10.1109/ismsit.2019.8932941.
15. Hekimoğlu B. Sine-cosine algorithm-based optimization for automatic voltage regulator system. *Transactions of the Institute of Measurement and Control*, 2018, vol. 41, no. 6, pp. 1761-1771. doi: https://doi.org/10.1177/0142331218811453.
16. Mosaad A.M., Attia M.A., Abdelaziz A.Y. Whale optimization algorithm to tune PID and PIDA controllers on AVR system. *Ain Shams Engineering Journal*, 2019, vol. 10, no. 4, pp. 755-767. doi: https://doi.org/10.1016/j.asej.2019.07.004.
17. Tavazoei M.S. Notes on integral performance indices in fractional-order control systems. *Journal of Process Control*, 2010, vol. 20, no. 3, pp. 285-291. doi: https://doi.org/10.1016/j.jprocont.2009.09.005.
18. Gozde H., Taplamacioglu M.C. Comparative performance analysis of artificial bee colony algorithm for automatic voltage regulator (AVR) system. *Journal of the Franklin Institute*, 2011, vol. 348, no. 8, pp. 1927-1946. doi: https://doi.org/10.1016/j.jfranklin.2011.05.012.
19. Aydiner E. Chaotic universe model. *Scientific Reports*, 2018, vol. 8, no. 1, p. 721. doi: https://doi.org/10.1038/s41598-017-18681-4.
20. Dos Santos Coelho L. Tuning of PID controller for an automatic regulator voltage system using chaotic optimization approach. *Chaos, Solitons & Fractals*, 2009, vol. 39, no. 4, pp. 1504-1514. doi: https://doi.org/10.1016/j.chaos.2007.06.018.
21. Abdullah A.H., Enayatifa R, Lee M. A Hybrid Genetic Algorithm and chaotic function model for image encryption. *Journal of Electronics and Communication*, 2012, vol. 66, pp. 806-816. doi: https://doi.org/10.1016/j.aeue.2012.01.015.
22. Çelik E., Rafet D. Performance enhancement of automatic voltage regulator by modified cost function and symbiotic organisms search algorithm. *Engineering Science and Technology, an International Journal*, 2018, vol. 21 no. 5, pp. 1104-1111. doi: https://doi.org/10.1016/j.jestch.2018.08.006.
23. George R.G., Hasanien H.M., Badr M.A., Elgendy M.A. A Comparative Study among Different Algorithms Investigating Optimum Design of PID Controller in Automatic Voltage Regulator. *2018 53rd International Universities Power Engineering Conference (UPEC)*, Glasgow, 2018, pp. 1-6. doi: https://doi.org/10.1109/UPEC.2018.8541870.
24. Çelik E. Incorporation of stochastic fractal search algorithm into efficient design of PID controller for an automatic voltage regulator system. *Neural Computing and Applications*, 2018, vol. 30, no. 6, pp. 1991-2002. doi: https://doi.org/10.1007/s00521-017-3335-7.
25. Odili J.B., Mohmad Kahar M.N., Noraziah A. Parameters-tuning of PID controller for automatic voltage regulators using the African buffalo optimization. *PLoS One*, 2017, vol. 12, no. 4, p. e0175901. doi: https://doi.org/10.1371/journal.pone.0175901.
26. Bingul Z., Karahan O. A novel performance criterion approach to optimum design of PID controller using cuckoo search algorithm for AVR system. *Journal of the Franklin Institute*, 2018, vol. 355, no. 13, pp. 5534-5559. doi: https://doi.org/10.1016/j.jfranklin.2018.05.056.
27. Kansit S., Assawinchaichote W. Optimization of PID controller based on PSOGSA for an automatic voltage regulator system. *Procedia Computer Science*, 2016, vol. 86, pp. 87-90. doi: https://doi.org/10.1016/j.procs.2016.05.022.
28. Chatterjee S., Mukherjee V. PID controller for automatic voltage regulator using teaching–learning based optimization technique. *International Journal of Electrical Power & Energy Systems*, 2016, vol. 77, pp. 418-429. doi: https://doi.org/10.1016/j.ijepes.2015.11.010.
29. Guvenc U., Yigit T., Isik A.H, , Akkaya I. Performance analysis of biogeography-based optimization for automatic voltage regulator system. *Turkish Journal of Electrical Engineering and Computer Sciences*, 2016, vol. 24, no. 3, pp. 1150-1162. doi: https://doi.org/10.3906/elk-1311-111.
30. Tang Y., Cui M., Hua C., Li L., Yang Y. Optimum design of fractional order PIλDμ controller for AVR system using chaotic ant swarm. *Expert Systems with Applications*, 2012, vol. 39, no. 8, pp. 6887-6896. doi: https://doi.org/10.1016/j.eswa.2012.01.007.
31. Gozde H., Taplamacıoğlu M.C. Comparative performance analysis of artificial bee colony algorithm for automatic voltage regulator (AVR) system. *Journal of the Franklin Institute*, 2011, vol. 348, no. 8, pp. 1927-1946. doi: https://doi.org/10.1016/j.jfranklin.2011.05.012.
32. Taherkhani M., Safabakhsh R. A novel stability-based adaptive inertia weight for particle swarm optimization. *Applied Soft Computing*, 2016, vol. 38, pp. 281-295. doi: https://doi.org/10.1016/j.asoc.2015.10.004.
33. Cao L., Xu L., Goodman E.D. A guiding evolutionary algorithm with greedy strategy for global optimization problems. *Computational Intelligence and Neuroscience*, 2016. doi: https://doi.org/10.1155/2016/2565809.
34. Liu Z., Murakami T., Kawamura S., Yoshida H. Parallel Implementation of Chaos Neural Networks for an Embedded GPU. *2019 IEEE 10th International Conference on Awareness Science and Technology (iCAST)*, Morioka, Japan, 2019, pp. 1-6. doi: https://doi.org/10.1109/ICAwST.2019.8923383.
35. Huang L., Ding S., Yu S., Wang J., Lu K. Chaos-enhanced Cuckoo search optimization algorithms for global optimization. *Applied Mathematical Modelling*, 2016, vol. 40, no. 5, pp. 3860-3875. doi: https://doi.org/10.1016/j.apm.2015.10.052.
36. Wang X., Sun H. A chaotic image encryption algorithm based on improved Joseph traversal and cyclic shift function. *Optics & Laser Technology*, 2020, vol. 122, p. 105854. doi: https://doi.org/10.1016/j.optlastec.2019.105854.
37. Tubishat M., Idris N., Shuib L., Abushariah M.A.M., Mirjalili S. Improved Salp Swarm Algorithm based on opposition based learning and novel local search algorithm for feature selection. *Expert Systems with Applications*, 2020, vol. 145, pp. 113122. doi: https://doi.org/10.1016/j.eswa.2019.113122.

38. Petrovic M., Vuković N., Mitić M., Miljković Z. Integration of process planning and scheduling using chaotic particle swarm optimization algorithm. *Expert Systems with Applications*, 2016, vol. 64, pp. 569-588. doi: https://doi.org/10.1016/j.eswa.2016.08.019.

39. Shadravan S., Naji H.R., Bardsiri V.K. The Sailfish Optimizer: A novel nature-inspired metaheuristic algorithm for solving constrained engineering optimization problems. *Engineering Applications of Artificial Intelligence*, 2019, vol. 80, pp. 20-34. doi: https://doi.org/10.1016/j.engappai.2019.01.001.

40. Luo Y., Yu J., Lai W., Liu L. A novel chaotic image encryption algorithm based on improved baker map and logistic map. *Multimedia Tools and Applications*, 2019, vol. 78, no. 15, pp. 22023-22043. doi: https://doi.org/10.1007/s11042-019-7453-3.

41. Sato Y., Son D.T., Lamb J.S.W., Rasmussen M. Dynamical characterization of stochastic bifurcations in a random logistic map. *ArXiv*, 2018, pp. 1811-03994. Available at: https://arxiv.org/pdf/1811.03994.pdf (accessed on 11 May 2020).

42. Liu B., Wang L., Jin Y.-H., Tang F., Huang D.-X. Improved particle swarm optimization combined with chaos. *Chaos, Solitons & Fractals.* 2005, vol. 25, no. 5, pp. 1261-1271. doi: https://doi.org/10.1016/j.chaos.2004.11.095.

43. Kumar A., Kumar V. A novel interval type-2 fractional order fuzzy PID controller: design, performance evaluation, and its optimal time domain tuning. *ISA Transactions*, 2017, vol. 68, pp. 251-275. doi: https://doi.org/10.1016/j.isatra.2017.03.022.

44. Zheng W., Luo Y., Wang X., Pi Y., Chen Y. Fractional order PIλDμ controller design for satisfying time and frequency domain specifications simultaneously. *ISA Transactions*, 2017, vol. 68, pp. 212-222. doi: https://doi.org/10.1016/j.isatra.2017.02.016.

Received 26.10.2020
Accepted 16.11.2020
Published 25.02.2021

Naveed Anwar[1], *M.S.*,
Amir Hanif[1], *Ph.D.*,
Muhammad Umair Ali[2], *Ph.D.*,
Amad Zafar[2], *Ph.D.*,
[1] Department of Electrical Engineering,
University of Wah,
Wah Cantt, Pakistan,
e-mail: naveed.anwar@wecuw.edu.pk,
dr.aamirhanif@wecuw.edu.pk.
[2] Department of Electrical Engineering,
University of Lahore, Islamabad Campus,
Islamabad, Pakistan,
e-mail: umairali.m99@gmail.com,
amad.zafar@ee.uol.edu.pk

How to cite this article:
Anwar N., Hanif A., Ali M.U., Zafar A. Chaotic-based particle swarm optimization algorithm for optimal PID tuning in automatic voltage regulator systems. *Electrical Engineering & Electromechanics*, 2021, no. 1, pp. 50-59. **doi: 10.20998/2074-272X.2021.1.08.**

UDC 621.3 **doi: 10.20998/2074-272X.2021.1.09**

B. Ayachi, T. Boukra, N. Mezhoud

MULTI-OBJECTIVE OPTIMAL POWER FLOW CONSIDERING THE MULTI-TERMINAL DIRECT CURRENT

Introduction. *In recent years, transmission systems comprise more direct current structures; their effects on alternating current power system may become significant and important. Also, multi-terminal direct current is favorable to the integration of large wind and solar power plants with a very beneficial ecological effect. The* ***novelty*** *of the proposed work consists in the effects of the aforementioned modern devices on transient stability, thus turn out to be an interesting research issue. In our view, they constitute a new challenge and an additional complexity for studying the dynamic behavior of modern electrical systems.* ***Purpose.*** *We sought a resolution to the problem of the transient stability constrained optimal power flow in the alternating current / direct current meshed networks. Convergence to security optimal power flow has been globally achieved.* ***Methods.*** *The solution of the problem was carried out in MATLAB environment, by an iterative combinatorial approach between optimized power flow computation and dynamic simulation.* ***Results.*** *A new transient stability constrained optimal power flow approach considering multi-terminal direct current systems can improve the transient stability after a contingency occurrence and operate the system economically within the system physical bounds.* ***Practical value.*** *The effectiveness and robustness of the proposed method is tested on the modified IEEE 14-bus test system with multi-objective optimization problem that reflect active power generation cost minimization and stability of the networks. It should be mentioned that active power losses are small in meshed networks relative to the standard network. The meshed networks led to a gain up to 46,214 % from the base case.* References 24, table 3, figures 11.
Key words: **transient stability constrained optimal power flow, multi-terminal direct current.**

Вступ. *В останні роки системи передачі електроенергії включають в себе більше структур постійного струму; їх вплив на енергосистему змінного струму може стати значним і важливим. Крім того, багатотермінальний постійний струм є сприятливим для інтеграції великих вітрових та сонячних електростанцій з дуже позитивним екологічним ефектом.* ***Новизна*** *запропонованої роботи полягає у впливі вищезазначених сучасних пристроїв на перехідну стабільність, що виявляється цікавим питанням для дослідження. На наш погляд, вони становлять нову проблему та додаткову складність для вивчення динамічної поведінки сучасних електричних систем.* ***Мета****. Ми шукали розв'язання задачі перехідної стабільності, обмеженої оптимальним потоком потужності в мережах змінного/постійного струму. Збіжність для забезпечення оптимального потоку енергії була глобально досягнута.* ***Методи****. Розв'язання задачі було здійснено в середовищі MATLAB за допомогою ітеративного комбінаторного підходу між оптимізованим обчисленням потоку потужності та динамічним моделюванням.* ***Результати****. Новий підхід, що обмежує перехідну стабільність, з урахуванням багатотермінальних систем постійного струму може покращити перехідну стабільність після виникнення непередбачених ситуацій та економічно експлуатувати систему у фізичних межах системи.* ***Практичне значення.*** *Ефективність та надійність запропонованого методу перевіряється на модифікованій тестовій 14-шинній системі IEEE з використанням багатоцільової задачі оптимізації, яка відображає мінімізацію витрат на активну генерацію електроенергії та стабільність мереж.* Бібл. 24, табл. 3, рис. 11.
Ключові слова: **перехідна стабільність, обмежена оптимальним потоком потужності, багатотермінальний постійний струм.**

Introduction. In a competitive economic environment that has placed the need for reconciliation of economic and transitional stability conditions, the cost of losing synchronism by transient instability is exceptionally high and of significant importance. For this reason, the traditional optimal power flow (OPF) approach has been extended to take into account the transient stability constraints of the system, giving a new transient stability constrained optimal power flow (TSC-OPF) approach [1]. The TSC-OPF procedures are classified in either global or sequential approaches [2, 3]. The global TSC-OPF approaches are reported in [4-7]. The sequential TSC-OPF approaches perform a standard OPF analysis to assess an optimal operating point [1]. A transient stability analysis is then carried out independently from the optimization process to check if the optimum point is transiently stable, so that the time domain simulation-related set of differential algebraic equations is not embedded in the traditional OPF problem [2, 8-10]. In recent decades, various optimization approaches have been proposed [11]. Among them, those dedicated to solve the multi-objective TSC-OPF problems where different goals and different constraints have been taken into account [12-14].

A proposed network topology in [15-18] has been used in our work for simulations propose. The meshed topology is of great interest for our proposed methodology.

This paper is organized as follows: first part concerns modelling AC/DC power system. In the second part, the TSC-OPF problem has been formulated. In the third part, the experimental results and conclusions are presented.

AC/DC power system modelling. A generalized AC/DC system of Fig. 1 consists of three parts.

1. AC grid. We present here the expressions for active and reactive power injections. Reader may refer to [19] for more details:

$$P_{gi}^{AC} = \sum_{j=1}^{n} \left|V_i^{AC}\right| \cdot \left|V_j^{AC}\right| \cdot \left(G_{ij}\cos\delta_{ij} + B_{ij}\sin\delta_{ij}\right); \quad (1)$$

$$Q_{gi}^{AC} = \sum_{j=1}^{n} \left|V_i^{AC}\right| \cdot \left|V_j^{AC}\right| \cdot \left(G_{ij} \sin \delta_{ij} - B_{ij} \cos \delta_{ij}\right), \quad (2)$$

where P_{gi}^{AC}, Q_{gi}^{AC} are active and reactive power generations at bus i respectively; V_i^{AC}, V_j^{AC} are nodal voltage values at buses i and j respectively; δ_{ij} is angle voltage of unit i and j; G_{ij} is the conductance; B_{ij} is the susceptance; n is the total number of generators.

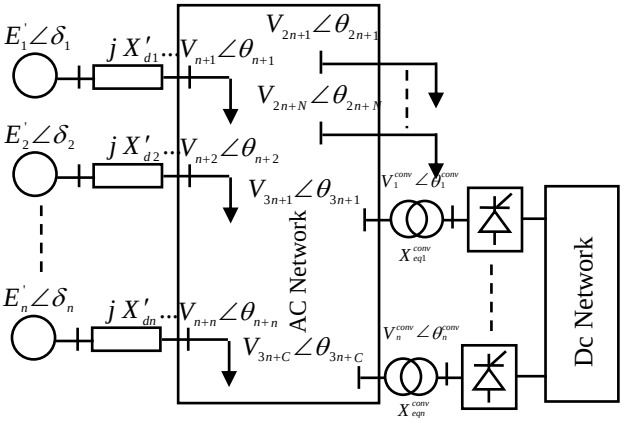

Fig. 1. Model for combined AC and DC grid

2. HVDC converters. Assuming a lossless converter model. The active power of the AC side converter coincides with that of the DC side:

$$P_c^{AC} = P_c^{DC}. \quad (3)$$

An HVDC converter station was modeled as a voltage source with variable value V^{conv} and angle θ^{conv} connected to an AC bus via a reactance X_{eq}^{conv}. By varying the voltage source, it is possible to produce the desired active and reactive power flow from the DC to the AC network or vice versa

$$P_i^{DC} = \frac{V_i^{AC} \cdot V_i^{conv}}{X_{eq}^{conv}} \sin\left(\theta_i^{AC} - \theta_i^{conv}\right); \quad (4)$$

$$Q_i^{DC} = \frac{V_i^{2,AC}}{X_{eq}^{conv}} - \frac{V_i^{AC} \cdot V_i^{conv}}{X_{eq}^{conv}} \cos\left(\theta_i^{AC} - \theta_i^{conv}\right). \quad (5)$$

3. DC grid. The power flows over the DC lines can be calculated as follows:

$$P_{ij}^{DC} = \frac{V_i^{DC} - V_j^{DC}}{R_{ij}}. \quad (6)$$

Problem statement and formulation. The theory of TSC-OPF is an extension of the standard OPF problem to include supplementary constraints for imaginable credible contingencies cases. In a standard form, the OPF problem is defined as in [20-22]:

$$\min\ f(x,u), \quad (7)$$

subject to

$$h(x,u) = 0; \quad (8)$$

$$g(x,u) \le 0. \quad (9)$$

where x is a vector of state variables; u is a vector of control variables; h, g are functions; $f(x, u)$ is an objective function.

In general, the intention is to minimize the objective function with the solution satisfying a number of equality and inequality constraints. But the TSC-OPF problem can be mathematically considered as a standard OPF with other inequality dynamic constraints forced by the rotor angles of generators during the transient period in study for a given set of contingencies.

1. Objective function. The objective functions f of TSC-OPF is minimization of fuel cost for all generators:

$$f = \min \sum_{i=1}^{n_g} \left(a_i + b_i \cdot P_{gi} + c_i \cdot P_{gi}^2\right), \quad (10)$$

where n_g is number of generators; a_i, b_i, c_i, are cost coefficients of unit i; P_{gi} is an active power generations by unit i.

2. Equality constraints. The equality constraints $h(x, u)$ are the sets of the load flow equations that govern the power system:

$$P_{gi}^{AC} + P_i^{DC} - P_{di} = 0; \quad (11)$$

$$Q_{gi}^{AC} + Q_i^{DC} - Q_{di} = 0, \quad (12)$$

where P_{di}, Q_{di} are active and reactive power loads by unit i respectively.

3. Inequality constraints (standard OPF). The inequality constraints $g(x, u)$ are the set of constraints that represent the system operational and security bounds like the limits on the following:

$$P_{AC,gi}^{\min} \le P_{gi} \le P_{AC,gi}^{\max}; \text{ where } i = 1,..., n_g; \quad (13)$$

$$Q_{AC,gi}^{\min} \le Q_{gi} \le Q_{AC,gi}^{\max}; \text{ where } i = 1,..., n_g; \quad (14)$$

$$V_{AC,i}^{\min} \le V_i \le V_{AC,i}^{\max};\ \ i = 1,....., n_b; \quad (15)$$

$$\theta_i^{\min} \le \theta_i \le \theta_i^{\max};\ \ i = 1,....., n_b; \quad (16)$$

$$T_i^{\min} \le T_i \le T_i^{\max};\ \ i = 1,....., n_T, \quad (17)$$

where $P_{AC,gi}^{\min}, P_{AC,gi}^{\max}$ and $Q_{AC,gi}^{\min}, Q_{AC,gi}^{\max}$ are the lower and upper limits of active and reactive power generation at bus i of AC network respectively; Q_{gi} is reactive power generations at bus i; $V_{AC,i}^{\min}, V_{AC,i}^{\max}$ are the lower and upper limits of voltage value at buses i; V_i is voltage value at buses i; n_b is total number of buses; $\theta_i^{\min}, \theta_i^{\max}$ are the lower and upper limits of angle voltage; θ_i is the angle voltage of unit i; $T_i^{\min}, T_i^{\max}$ are the lower and upper limits of transformers tap settings; T_i is transformers tap settings of unit i; n_T is total number of transformers.

4. Inequality constraints (transient stability). The transient stability problem in power system is defined by a differential algebraic equation, which can be solved by time domain simulation. The swing equation for i^{th} generators is:

$$\frac{d\omega_i}{dt} = \frac{\omega_i}{M_i}\left[\left(P_{mi} - P_{ei}\right) - D\left(\omega_s - \omega_i\right)\right]; \quad (18)$$

$$\frac{d\delta_i}{dt} = \omega_i - \omega_s;\ \text{where}\ \ i = 1,....., n_g \quad (19)$$

$$\frac{dE'_{di}}{dt} = \frac{1}{T'_{qi0}}\left[-E'_{di} + (X_{qi} - X'_{qi}) i_{qi}\right]; \quad (20)$$

$$\frac{dE'_{qi}}{dt} = \frac{1}{T'_{di0}}\left[E_{fdi} - E'_{qi} - (X_{di} - X'_{di})i_{di}\right]; \quad (21)$$

$$\frac{dE_{fdi}}{dt} = \frac{1}{T_{Ai}}\left[-E_{fdi} + K_{Ai}(V_{refi} - V_t)\right]; \quad (22)$$

$$\frac{d\omega_i}{dt} = \frac{\omega_i}{M_i}\left[(P_{mi} - P_{ei}) - D(\omega_s - \omega_i)\right]; \quad (23)$$

$$\frac{d\delta_i}{dt} = \omega_i - \omega_s, \text{ where } i = 1,.....,n_g, \quad (24)$$

where P_{mi} is the mechanical input generator by unit i; P_{ei} is the electrical output generator by unit i; M_i is the moment of inertia of i^{th} generator; ω_i is the angular speed of the rotating synchronous reference frame of unit i; ω_s is the angular speed of the generator rotor of unit i; δ_i is rotor angle of unit i; D is the generators damping torque coefficient; E'_{di}, E'_{qi} are the internal transient voltage of generator of unit i; E_{fdi} is the excitation voltage of generator of unit i; i_{di}, i_{qi} are d-axis and q-axis courant of generator of unit i; T'_{d0i}, T'_{q0i} are the d-open circuit and q-open circuit transient time constants of generator of unit i; X'_{di}, X'_{qi} are the d-transient reactance and q-transient reactance of generator of unit i; X_{di}, X_{qi} are the d-synchronous reactance and q-synchronous reactance of generator of unit i; V_{refi} is voltage reference of generator of unit i.

The inequality constraints of transient stability are formulated as:

$$\left|\delta_i - \delta_{COI}\right| \le \delta_{\max}; \quad (25)$$

$$\delta_{COI} = \frac{\sum_{i=1}^{n_g} M_i \delta_i}{\sum_{i=1}^{n_g} M_i}, \quad (26)$$

where δ_i is the rotor angle of unit i; δ_{COI} is the position angle of centre of inertia (COI – centre of inertia); $\delta_{\max}$ is the maximum allowable rotor angle deviation

The selection of $\delta_{\max}$ is frequently based on experiment operation. It was generally limited to 100° to allow network having sufficient stability margin [23, 24].

5. Inequality constraints (multi-terminal direct current – MTDC). The last constraint limits the variance of the all DC nodes have their minimal and maximal voltage angle limits, in which the equipment can operate safely.

$$\theta^{\min}_{DC,j} \le \theta_{DC,j} \le \theta^{\max}_{DC,j}; \text{ where } j = 1,.....,n_{b'}; \quad (27)$$

$$P^{\min}_{DC,j} \le P_{DC,j} \le P^{\max}_{DC,j}; \text{ where } j = 1,.....,n_{b'}, \quad (28)$$

where $P^{\min}_{DC,j}, P^{\max}_{DC,j}$ are the lower and upper limits of active power generation at bus j of DC buses; $P_{DC,j}$ is the active power generation at bus j of DC buses; $\theta^{\min}_{DC,j}, \theta^{\max}_{DC,j}$ are the lower and upper limits of angle voltage of DC buses; $\theta_{DC,j}$ is the angle voltage of DC buses; $n_{b'}$ is the total number of DC buses.

Simulation results and discussion. In this paper, the MTDC system presented for the simulation with integrated offshore wind farm is shown in Fig. 2. This system is a modified version of the IEEE 14-bus test system. A meshed DC grid including an additional generator has been added, that connects to the AC system to various buses through voltage source converters (VSC). The bus and line parameters were given in the [24]. All the simulations were performed on source codes developed in MATLAB environment running on an Intel Core i5 2.67GHz CPU and 3GB RAM.

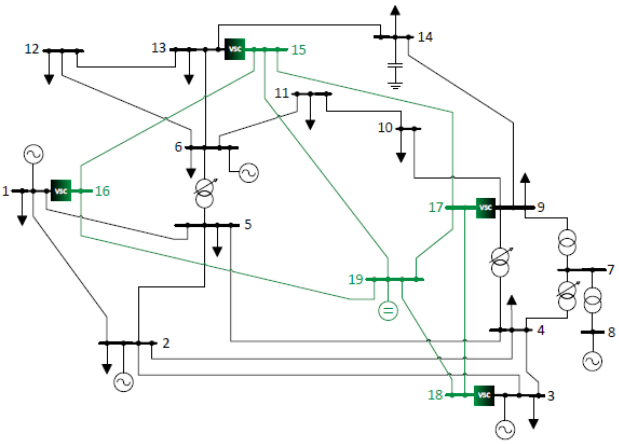

Fig. 2. Modified IEEE 14-bus

The fault priority list was given in Table 1. The top 4 faults in critical clearing time (CCT) are considered.

According to Table 1 and Fig. 3, it is evident that the most unfavorable case is the three-phase fault (3φ). However, it should be noted that there are, for certain types of connection, cases where other types of fault are more damaging. The best known of these faults are:

- single line to ground fault (SLG), when the generator neutral is connected to ground directly or through low impedance;
- single line to ground fault, when the transformer is connected in Y-Δ with neutral grounded.

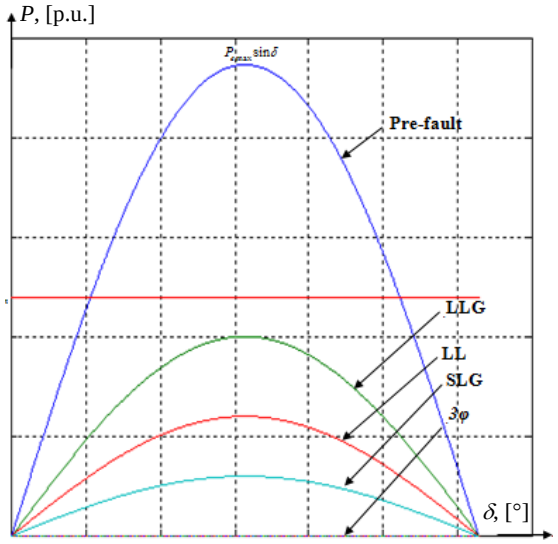

Fig. 3. Power injected by the generator, depending on the type of fault (LLG is double line to ground fault; LL is line to line faults; SLG is single line to ground fault; 3φ is three-phase fault)

Table 1

Priority list of fault for IEEE 14 bus system

Cases	Faults		Line	CCT(s)
	3φ	SLG		
1	1		1-2	0.33
2	1		1-5	0.36
3		1	1-2	0.38
4	2		1-2	0.40

The severity criteria considered in this study is the critical clearing time (CCT). This study was performed according to the 2 different faults (three-phase fault and single line to ground).

In this section, the modified IEEE 14-bus system has been used to illustrate the effectiveness of the proposed method. There are 5 cases to be discussed here, each with 2 scenarios:

- Case 1 is the standard power flow (PF);
- Case 2 is the standard OPF without transient stability constraints;
- Case 3 is OPF with transient stability constraints;
- Case 4 when IEEE 14-bus is modified, with added MTDC and without transient stability constraints;
- Case 5 using a new configuration of network with transient stability constraints.

The results are given in Table 2.

Table 2

Optimization results for IEEE 14 bus system

	Case 1		Case 2		Case 3		Case 4		Case 5	
	3φ fault	SLG fault	3φ fault	SLG fault	3φ fault	SLG fault	3φ fault	SLG fault	3φ fault	SLG fault
P_{g1}, MW	232		194.41		186.63	174.97	146.41		137.63	120.06
P_{g2}, MW	40		36.74		37.03	37.44	25.61		34.34	39.61
P_{g3}, MW	0		28.61		31.53	35.41	0		0	0.07
P_{g6}, MW	0		0		0	1.28	0		0	8.82
P_{g8}, MW	0		8.52		12.44	17.58	0		0	3.23
P_{g19}, MW	–		–		–	–	100		100	100
Fuel cost ($/h)	–		8080.77		8084.20	8102.18	5526.65		5549.29	5691.48
CCT (s)	0.33	0.38	0.51	0.45	0.57	0.47	0.28	0.37	0.31	0.39
Losses (MW)	–		9.277		8.610	7.674	1.417		1.370	1.187

First, simulation results were presented with standard PF (case 1). With this generation, it was found that system transient stability was lost following the three-phase fault disturbance at bus 1 (cleared by tripping line 1-2 at 0.33 s), and was lost following single line to ground fault at bus 1 (cleared by tripping line 1-2 at 0.38 s) respectively. Visibly the system can't operate under this mode.

The second simulation (case 2), was the standard OPF without transient stability constraints; the objective function (fuel cost) reached 8080.77 $/h. But with this generation, it was found that system transient stability was lost following the fault disturbance at bus 1, as shown in Fig. 4, 5, respectively. Visibly the system can't operate under this mode because security of the network is always violated.

Case 3, scenario 1 (3φ fault), the active power of generator 1 is reduced from 194.41 MW to 186.63 MW, while those of generators 2, 3 and 8 were increased from 36.74 MW, 28.61 MW and 8.52 MW (case 2) to 37.44 MW, 31.53 MW and 12.44 MW (case 3) respectively. A fuel cost was increased from 8080.77 $/h (case 2) to 8084.20 $/h (case 3) as shown in Table 2 and Fig. 6. A consequence of satisfying the transient stability constraints is the increasing in fuel cost only by 0.042 %.

For scenario 2 (SLG fault), the active power of generator 1 is reduced from 194.41 MW to 174.97 MW. While those of generators 2, 3, 6 and 8 were increased from 36.74 MW, 28.61 MW, 0 MW and 08.52 MW to 37.44 MW, 35.41 MW, 1.28 MW and 17.58 MW (case 3) respectively. The fuel cost was increased from 8080.77 $/h (case 2) to 8102.18 $/h (case 3) as shown in Table 2 and Fig. 7. A consequence of satisfying the transient stability constraints is the increasing in fuel cost only by 0.246 %.

From Fig. 6, 7, the use of transient stability constraints in terms of OPF solution gives better results and ensures system transient stability following the fault disturbances.

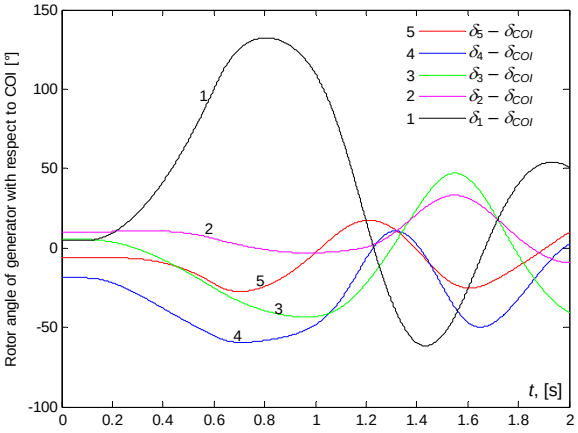

Fig. 4. Response of rotor angle (case 2, OPF), 3φ fault

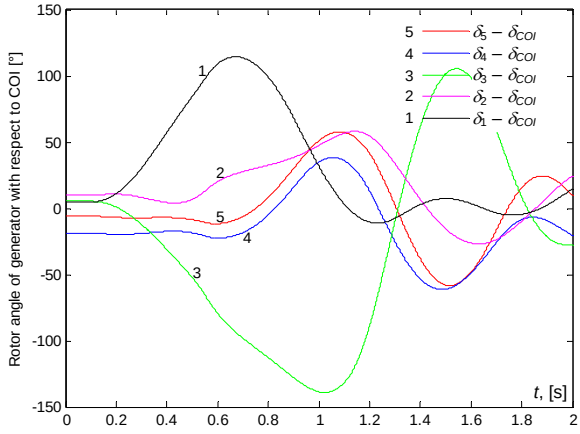

Fig. 5. Response of rotor angle (case 2, OPF), SLG fault

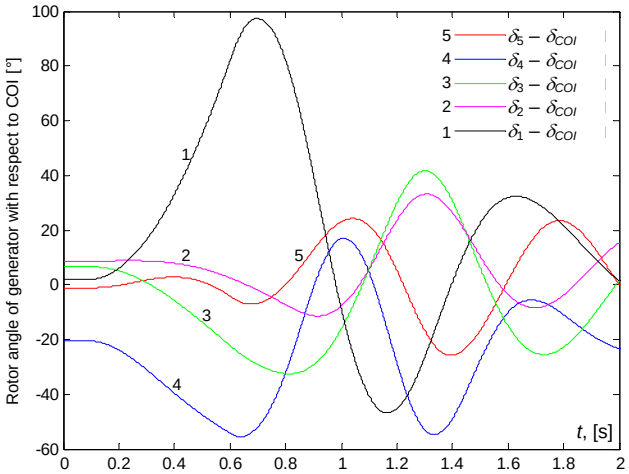

Fig. 6. Response of rotor angle (case 3, TSC-OPF), 3φ fault

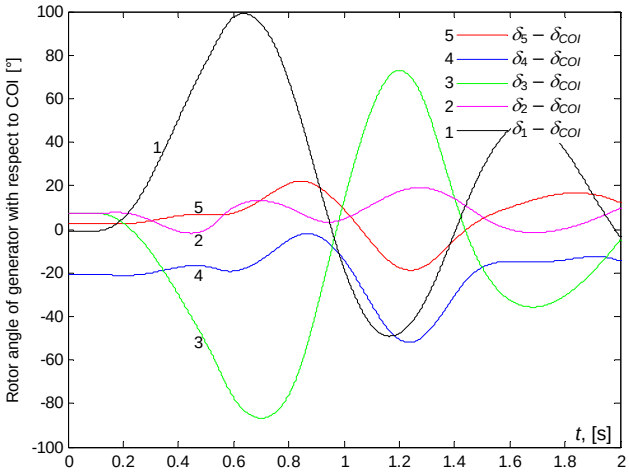

Fig. 7. Response of rotor angle (case 3, TSC-OPF), SLG fault

Cases 4 and 5 the network is modified, and at the present the total loads is 295 MW (new load at bus 1, active power 11.6 MW) and a new generator is present on the DC bus (bus 19). The solution of cases 4 and 5, with and without transient stability constraints is given in Table 2.

The fourth simulation (case 4), the fuel cost was reduced to 5526.66 $/h. But with this generation, it was found that system transient stability was lost following the fault disturbance at bus 1, as shown in Fig. 8, 9, respectively. Visibly the system can't operating under this mode because security of the network was violated.

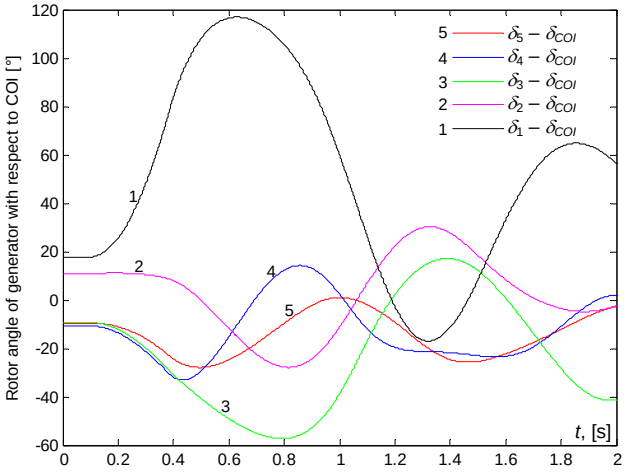

Fig. 8. Response of rotor angle (case 4, OPF, MTDC), 3φ fault

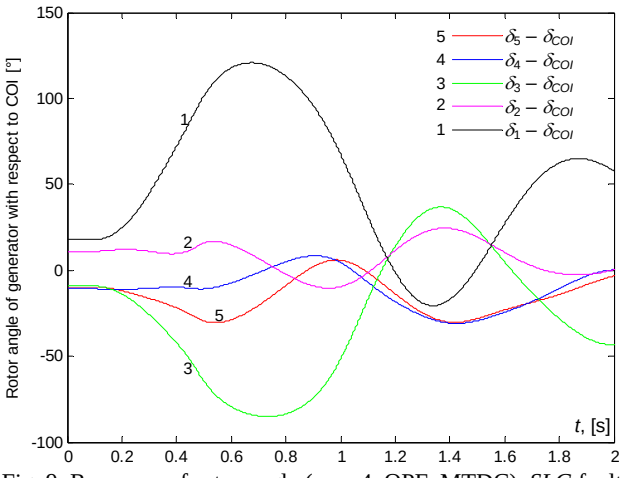

Fig. 9. Response of rotor angle (case 4, OPF, MTDC), *SLG* fault

In case 5, scenario 1 (3φ fault), in order to retain the transient stability limits, the active power of generator 1 was reduced from 146.41 MW to 137.63 MW, while that of generator 2 was increased to 34.34 MW. The fuel cost was increased from 5526.66 $/h to 5549.29 $/h as shown in Table 1 and Fig. 8. A consequence of satisfying the transient stability constraints was the increase in fuel cost by 0.409 %.

For last scenario (SLG fault), the active power of generator 1 is reduced to 120.06 MW. While those of generators 2, 3, 6 and 8 were increased to 39.61 MW, 0.07 MW, 8.82 MW and 3.23 MW, respectively. A consequence of satisfying the transient stability constraints was the increase in fuel cost by 2.982 %.

From Fig. 10, 11 it was obvious that the use of TSC in OPF solution gives better results and guarantees transient stability following the fault.

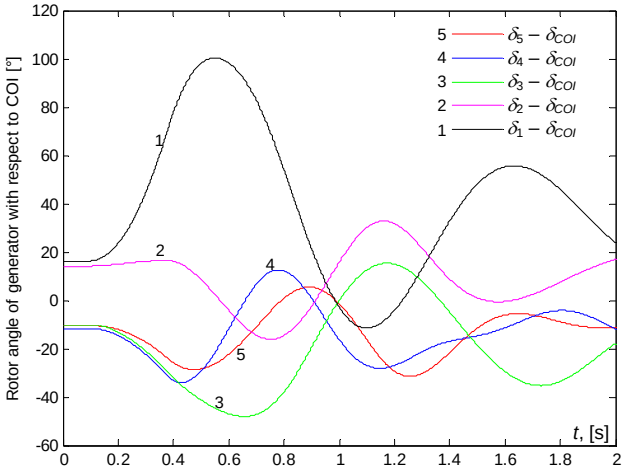

Fig. 10. Response of rotor angle (case 5, TSC-OPF, MTDC), 3φ fault

For the best compromise solution, we must maintain a balance between stability and economy. The solution obtained enhances the transient stability of the system at the best acceptable cost. Generally, in this situation, the cost is marginally higher as the economy is sacrificed for the improvement of transient stability. In case of lower cost solution, more emphasis is given to economy of the system and this solution is unable to improve the global transient stability of the network. For minimum cost

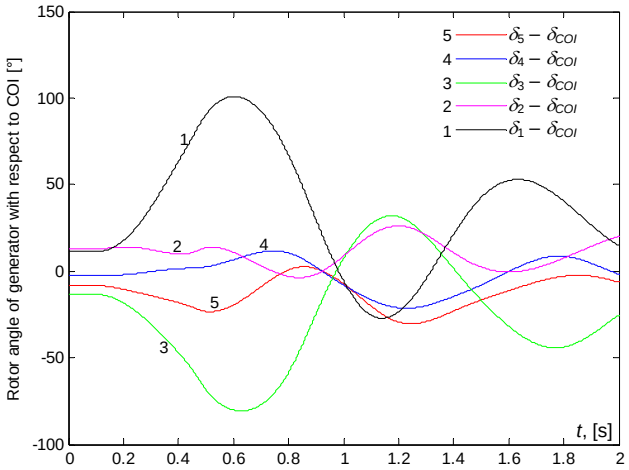

Fig. 11. Response of rotor angle (case 5, TSC-OPF, MTDC), SLG fault

case 4, the CCT for the fault at bus 1 cleared by tripping line 1-2 becomes 0.28 s whereas it was 0.33 s for three-phase fault and 0.37 s to 0.38 s for base case for single line to ground fault, as shown in Table 3.

Table 3

CCT comparison

	3φ fault	SLG fault
Case 1	0.33	0.38
Case 2	0.51	0.45
Case 3	0.57	0.47
Case 4	0.28	0.37
Case 5	0.31	0.39

Finally, the solution sought for the problem of the transient stability constrained optimal power flow, in the last case, compared to all the previous solutions that maximize the transient stability index, has the highest cost as more focus is placed on optimizing the system's transient efficiency. In the event of emergency situations, this approach can be extremely useful.

It should be mentioned that active power losses are small in mixed AC/DC networks relative to the standard AC network. The AC/DC networks led to a gain up to 46,214 % from the base case. This confirms the potential need for construction of solar or wind farms, considering their advantages.

Conclusions.

It is very likely that future transmission systems will contain more multi-terminal direct current links and the effects of such system on transient stability are yet to be determined. The increase of the future system has led to a growing complexity in the study of its problem and so presents new defy to power system stability. This paper suggests a new version of the multi-objective optimal power flow, taking into account the transient stability of the power system. Two goals were concurrently considered; minimizing the cost of the fuel and optimizing the system's transient stability margin at the point of fault clearance. Furthermore, this study was performed on the basis of two different faults namely three-phase fault and single line to ground fault.

Simulations were carried out in MATLAB environment, the transient stability of the system is compared with and without the presence of transient stability constraints. The use of transient stability constraints in terms of optimal power flow solution gives better results and also ensures system transient stability following the fault disturbance.

Conflict of interests. The authors declare no conflicts of interest.

REFERENCES

1. Pizano-Martinez A., Fuerte-Esquivel C.R., Zamora-Cardenas E.A., Lozano-Garcia J.M. Directional Derivative-Based Transient Stability-Constrained Optimal Power Flow. *IEEE Transactions on Power Systems*, 2017, vol. 32, no. 5, pp. 3415-3426. doi: https://doi.org/10.1109/tpwrs.2016.2633979.

2. Nguyen T.B., Pai M.A. Dynamic security-constrained rescheduling of power systems using trajectory sensitivities. *IEEE Transactions on Power Systems*, 2003, vol. 18, no. 2, pp. 848-854. doi: https://doi.org/10.1109/tpwrs.2003.811002.

3. Tu X., Dessaint L., Kamwa I. A global approach to transient stability constrained optimal power flow using a machine detailed model. *Canadian Journal of Electrical and Computer Engineering*, 2013, vol. 36, no. 1, pp. 32-41. doi: https://doi.org/10.1109/cjece.2013.6544470.

4. Gan D., Thomas R.J., Zimmerman R.D. Stability-constrained optimal power flow. *IEEE Transactions on Power Systems*, 2000, vol. 15, no. 2, pp. 535-540. doi: https://doi.org/10.1109/59.867137.

5. La Scala M., Trovato M., Antonelli C. On-line dynamic preventive control: an algorithm for transient security dispatch. *IEEE Transactions on Power Systems*, 1998, vol. 13, no. 2, pp. 601-610. doi: https://doi.org/10.1109/59.667388.

6. Pizano-Martinez A., Fuerte-Esquivel C.R., Ruiz-Vega D. Global Transient Stability-Constrained Optimal Power Flow Using an OMIB Reference Trajectory. *IEEE Transactions on Power Systems*, 2010, vol. 25, no. 1, pp. 392-403. doi: https://doi.org/10.1109/tpwrs.2009.2036494.

7. Zarate-Minano R., Van Cutsem T., Milano F., Conejo A.J. Securing Transient Stability Using Time-Domain Simulations Within an Optimal Power Flow. *IEEE Transactions on Power Systems*, 2010, vol. 25, no. 1, pp. 243-253. doi: https://doi.org/10.1109/tpwrs.2009.2030369.

8. Ruiz-Vega D., Pavella M. A comprehensive approach to transient stability control. I. Near optimal preventive control. *IEEE Transactions on Power Systems*, 2003, vol. 18, no. 4, pp. 1446-1453. doi: https://doi.org/10.1109/tpwrs.2003.818708.

9. Bettiol A.L., Wehenkel L., Pavella M. Transient stability-constrained maximum allowable transfer. *IEEE Transactions on Power Systems*, 1999, vol. 14, no. 2, pp. 654-659. doi: https://doi.org/10.1109/59.761894.

10. Pizano-Martinez A., Fuerte-Esquivel C.R., Ruiz-Vega D. A New Practical Approach to Transient Stability-Constrained Optimal Power Flow. *IEEE Transactions on Power Systems*, 2011, vol. 26, no. 3, pp. 1686-1696. doi: https://doi.org/10.1109/tpwrs.2010.2095045.

11. Ghasemi M., Ghavidel S., Ghanbarian M.M., Gharibzadeh M., Azizi Vahed A. Multi-objective optimal power flow considering the cost, emission, voltage deviation and power losses using multi-objective modified imperialist competitive algorithm. *Energy*, 2014, vol. 78, pp. 276-289. doi: https://doi.org/10.1016/j.energy.2014.10.007.

12. Yue Yuan, Kubokawa J., Sasaki H. A solution of optimal power flow with multicontingency transient stability constraints. *IEEE Transactions on Power Systems*, 2003, vol. 18, no. 3, pp. 1094-1102. doi: https://doi.org/10.1109/tpwrs.2003.814856.

13. Xu Y., Dong Z.Y., Meng K., Zhao J.H., Wong K.P. A Hybrid Method for Transient Stability-Constrained Optimal

Power Flow Computation. *IEEE Transactions on Power Systems*, 2012, vol. 27, no. 4, pp. 1769-1777. doi: https://doi.org/10.1109/tpwrs.2012.2190429.
14. Ye C.-J., Huang M.-X. Multi-Objective Optimal Power Flow Considering Transient Stability Based on Parallel NSGA-II. *IEEE Transactions on Power Systems*, 2015, vol. 30, no. 2, pp. 857-866. doi: https://doi.org/10.1109/tpwrs.2014.2339352.
15. Saplamidis V., Wiget R., Andersson G. Security constrained Optimal Power Flow for mixed AC and multi-terminal HVDC grids. *2015 IEEE Eindhoven PowerTech*, Eindhoven, 2015, pp. 1-6. doi: https://doi.org/10.1109/ptc.2015.7232616.
16. Wiget R., Vrakopoulou M., Andersson G. Probabilistic security constrained optimal power flow for a mixed HVAC and HVDC grid with stochastic infeed. *2014 Power Systems Computation Conference*, Wroclaw, 2014, pp. 1-7. doi: https://doi.org/10.1109/pscc.2014.7038408.
17. Wiget R., Iggland E., Andersson G. Security constrained optimal power flow for HVAC and HVDC grids. *2014 Power Systems Computation Conference*, Wroclaw, 2014, pp. 1-7. doi: https://doi.org/10.1109/pscc.2014.7038444.
18. Wiget R., Andersson G. Optimal power flow for combined AC and multi-terminal HVDC grids based on VSC converters. *2012 IEEE Power and Energy Society General Meeting*, San Diego, CA, 2012, pp. 1-8. doi: https://doi.org/10.1109/pesgm.2012.6345448.
19. Duong T., JianGang Y., Truong V. Improving the transient stability-constrained optimal power flow with Thyristor Controlled Series Compensators. *Russian Electrical Engineering*, 2014, vol. 85, no. 12, pp. 777-784. doi: https://doi.org/10.3103/s1068371214120165.
20. Acha E., Roncero-Sánchez P., Villa Jaén A., Castro L.M., Kazemtabrizi B. *VSC-FACTS-HVDC Analysis, Modelling and Simulation in Power Grids*. JohnWiley & Sons Ltd Publ., 2019. 404 p. doi: https://doi.org/10.1002/9781119190745.
21. Mukherjee A., Roy P.K., Mukherjee V. Transient stability constrained optimal power flow using oppositional krill herd algorithm. *International Journal of Electrical Power & Energy Systems*, 2016, vol. 83, pp. 283-297. doi: https://doi.org/10.1016/j.ijepes.2016.03.058.
22. Bilel A., Boukadoum A., Leulmi S., Boukra T. Improving the Transient Stability of the Mixed AC/DC Networks with FACTS. *Indonesian Journal of Electrical Engineering and Informatic*), 2018, vol. 6, no. 4, pp. 477-485. doi: https://doi.org/10.11591/ijeei.v6i4.473.
23. Abido M.A., Waqar Ahmed M. Multi-objective optimal power flow considering the system transient stability. *IET Generation, Transmission & Distribution*, 2016, vol. 10, no. 16, pp. 4213-4221. doi: https://doi.org/10.1049/iet-gtd.2016.1007.
24. Ayachi B. *Apport des FACTS intelligents à l'amélioration de la stabilité transitoire des réseaux électriques.* Doctoral thesis of 20 Aout 1955 Skikda University, 2019. Ref D012120003D. (Fra).

Received 04.11.2020
Accepted 11.12.2020
Published 25.02.2021

Bilel Ayachi[1], *Ph.D. of Power Engineering,*
Tahar Boukra[1], *Ph.D. of Power Engineering,*
Nabil Mezhoud [1], *Ph.D. of Power Engineering,*
[1] Electrotechnical Laboratory Skikda (LES),
Department of Electrical Engineering,
University 20 August 1955,
26 Road El Hadaiek 21000, Skikda, Algeria,
e-mail: b.ayachi@univ-skikda.dz,
boukratahar@hotmail.com,
mezhounab@yahoo.fr

How to cite this article:
Ayachi B., Boukra T., Mezhoud N. Multi-objective optimal power flow considering the multi-terminal direct current. *Electrical Engineering & Electromechanics*, 2021, no. 1, pp. 60-66. **doi: 10.20998/2074-272X.2021.1.09.**

UDC 621.3 **doi: 10.20998/2074-272X.2021.1.10**

K. Nebti, R. Lebied

FUZZY MAXIMUM POWER POINT TRACKING COMPARED TO SLIDING MODE TECHNIQUE FOR PHOTOVOLTAIC SYSTEMS BASED ON DC-DC BOOST CONVERTER

Aim. *This paper presents the amelioration of maximum power point tracking using fuzzy logic methods for photovoltaic system supplying a standalone system.* ***Method***. *The main role of the maximum power tracking is to force the system for working at the maximum point for each change of meteorological conditions. The classic technique Perturb and Observe is more attractive due to its simple and high efficiency. Sliding mode is a non-linear control technique; characterised by robustness against the parameters change or disturbances, it gives a good maximum power operation under different conditions such as changing solar radiation and photovoltaic cell temperature.* ***Novelty***. *Fuzzy logic tracking technique is treated. Fuzzy rules construction is based on Perturb and Observe behaviour when the appropriate disturbance step is produced in order to obtain a fast system with an acceptable precision. We use in our study 60 W photovoltaic panel associated to boost chopper converter in order to supply a standalone system.* ***Results***. *As show in results figures using fuzzy maximum power point tracking the ameliorate performances especially the very low oscillation rate (nearly 0.6 W), and very acceptable response time 0.1 s.* References 20, tables 1, figures 19.
Key words: **solar panel, maximum power point tracking, perturb and observe, sliding mode, Fuzzy logic.**

Мета. *У цій роботі представлено покращення відстеження точки максимальної потужності з використанням методів нечіткої логіки для фотоелектричної системи, що постачає електроенергію до автономної системи.* ***Метод***. *Основна роль відстеження максимальної потужності – примусити систему працювати в максимальній точці при кожній зміні метеорологічних умов. Класична техніка збурення та спостереження є більш привабливою завдяки своїй простоті та високій ефективності. Режим ковзання – це нелінійний метод керування; характеризується стійкістю до зміни параметрів або порушень, дає хорошу максимальну потужність роботи в різних умовах, таких як зміна сонячного випромінювання та температури фотоелектричних елементів.* ***Новизна***. *Використовується методика відстеження з використанням нечіткої логіки. Побудова нечітких правил базується на поведінці збурення та спостереження, коли виробляється відповідний крок збурення, щоб отримати швидку систему з прийнятною точністю. У цьому дослідженні використовується фотоелектрична панель потужністю 60 Вт, підключена до перетворювача, що підвищує, для постачання електроенергії до автономної системи.* ***Результати***. *Як показують результати, дані використовують нечітку максимальну точку потужності, яка відстежує покращені характеристики, особливо дуже низьку швидкість коливань (майже 0,6 Вт) і дуже прийнятний час відгуку 0,1 с.* Бібл. 20, табл. 1, рис. 19.
Ключові слова: **сонячна панель, відстеження точки максимальної потужності, збурення та спостереження, режим ковзання, нечітка логіка.**

Introduction. Renewable energies represent an attractive solution as replacement or complement of the conventional sources. Among renewable energies, are those resulting from the sun, wind, heat of the ground, water or of the biomass. With the difference in fossil energies, renewable energies are unlimited resource. Renewable energies are divided in a certain number of technological fields according to the developed energy source and useful energy obtained. The field studied in this paper is photovoltaic (PV) solar.

In direct couplings of the loads to PV system, the PV panels are often oversized to ensure a sufficient power to provide the load; this led to an excessively expensive system.

It very is easy to calculate the operating power of the PV panels. But, the determination of the reference power is more delicate view that it is function of meteorological parameters (temperature and illumination).

This variable reference, characterized by a non-linear function, makes the operation at maximum power more difficult to achieve. Then, maximum power point tracking (MPPT) is necessary. Generally it is based on the adjustment of the duty cycle controlling the static converter until it is placed on the PPM. Different MPPT methods have been published in the literature for optimal functioning, such as short-circuit current, incremental conductance algorithms, modified hill climbing MPPT method [1].

Perturb and observe (P&O) method is largely widespread approach in the research of the MPPT because it is simple and requires only measurements of voltage and current of the photovoltaic panel (V_{PV} and I_{PV} respectively, two sensors necessary), it should be known that this type of control imposes a permanent oscillation around the maximum power point (MPP) [2].

The sliding mode control technique is generally used to control the power electronics converters that constitute systems with variable structure [3, 4]. Recently sliding mode is used to control a grid connected PV system [5, 6] supplying stand alone PV system such as the pumping system.

In order to ameliorate the respond time and eliminate the oscillation around the MPP, a fuzzy control based on P&O idea is applied with different membership and fuzzy rules at both sides of MPP. Under this method, the perturbation step is adjusted according to controller inputs and working point.

The **aim** of this paper is the amelioration of maximum power point tracking using fuzzy logic methods for photovoltaic system supplying a standalone system.

Electric model of PV cell. To predict the PV system performance, it is better to make an equivalent model and analyze its behavior under variable conditions.

The simplified equivalent circuit of the PV cell with junction *p-n* (Fig. 1) includes a current source I_{PV}, who gives the photoelectric current model, associated with a diode in parallel which gives the junction *p-n* model, whose polarization determines voltage.

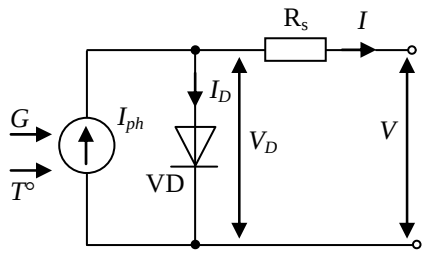

Fig. 1. Equivalent model of the simplified PV cell

And also a series resistance which is the internal resistance of the cell, it depends mainly on the resistance of the semiconductor used, it is also affected by temperature influence [7]

$$I = I_{ph} + I_D; \tag{1}$$

$$I_{ph} = I_{ph}(T_1)\cdot\left[1 + K_0\cdot(T - T_1)\right]; \tag{2}$$

$$I_{ph}(T_1) = I_{cc}(T_1)\cdot\left(\frac{G}{G_0}\right), \tag{3}$$

where I is the current produced by the PV cell; I_{ph} is the photonic current, proportional to the illumination G; I_D is the current flowing through the diode; T_1 is the reference temperature (T_1 = 25 °C = 298 °K); G_0 is the reference illumination (G_0 = 1000 W/m^2); K_0 is the coefficient of variation of the current as a function of the temperature T; I_{cc} is the short-circuit current (the current flowing through the junction under illumination when the cell is short-circuited).

And the relationship between current and voltage of a solar cell is:

$$I = I_{ph} - I_s\left(e^{\left(\frac{q(V+R_s\cdot I)}{nk_bT}\right)} - 1\right), \tag{4}$$

where I_s is the saturation current; k_b is Boltzmann constant; V is the voltage at the cell terminals; R_s is the resistance series; n is the diode ideality factor, where $1 < n < 2$; q is the electron charge (q = 1.602·10^{-19} C).

Boost converter modeling. Boost converter (Fig. 2) is composed of a boost inductance L, a controlled switch K, a diode VD and filtering capacitors C. When the switch K is on, the boost inductance current increases linearly, the diode VD being blocked. When switch K is off, the energy stored in the inductor, pass through the diode to the output circuit [8].

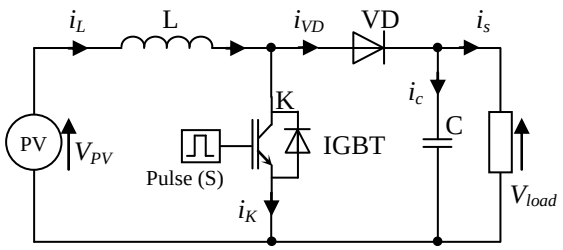

Fig. 2. DC-DC boost chopper scheme

The modeling of this converter passes by the analysis of the different operation sequences that we will suppose durations fixed by the command S. There appear two operation sequences according to the state of the switch K.

When K is closed so VD is opened:

$$\begin{aligned} V_{PV} &= L\frac{di_L}{dt}; \\ 0 &= C\frac{dV_{load}}{dt} + i_s. \end{aligned} \tag{5}$$

When K is opened:

$$\begin{aligned} V_{PV} &= L\frac{di_L}{dt} + V_{load}; \\ i_L &= C\frac{dV_{load}}{dt} + i_s. \end{aligned} \tag{6}$$

By putting (S = 1) when the switch K is closed and (S = 0) for open K, we can represent the converter according to the switch state S by the following equations:

$$V_{PV} = L\frac{di_L}{dt} + V_{load}\cdot(1 - S); \tag{7}$$

$$(1 - S)\cdot i_L = C\frac{dV_{load}}{dt} + i_s. \tag{8}$$

Perturb and observe algorithm. The principle of P&O MPPT control is to disturb the voltage V_{PV} with a low amplitude around its initial value and analyze the behaviour of the power variation P_{PV} resulting. So, as shown in Fig. 3, we can deduce if a positive increment of the voltage V_{PV} generates increased power P_{PV} that means that the operating point is left of MPP. If not the system has exceeded the MPP. Similar reasoning can be made when the voltage decreases [9, 10].

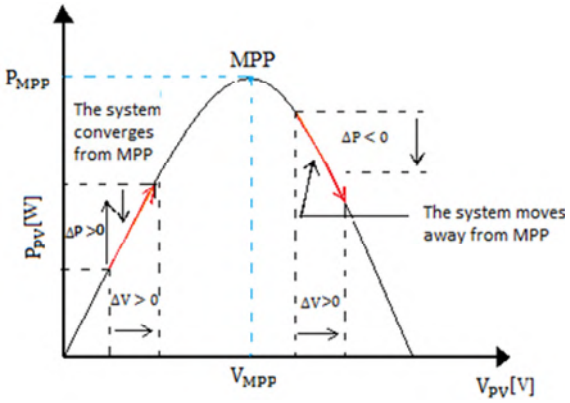

Fig. 3. P&O principle

At each cycle, V_{PV} and I_{PV} are measured to calculate $P_{PV}(k)$, where k indicate the present cycle. This value $P_{PV}(k)$ is compared with the value $P_{PV}(k-1)$ calculated in the previous cycle.

The disadvantage of this type of control is that if quick change of the illumination such as a mobile cloud, this command has more losses, generated by the long response time of the control to reach the new MPP.

P&O MPPT simulation. We apply two fast change of illumination, the first at time t = 0.4 s, from 1000 W/m^2 to 700 W/m^2 and the second at time t = 0.8 s from 700 W/m^2 to 900 W/m^2.

In Fig.4–6 which represent the evolution of the current, power and voltage, these curves contain fluctuations, especially in transient periods, due to the oscillation of P&O around MPP with fixed step.

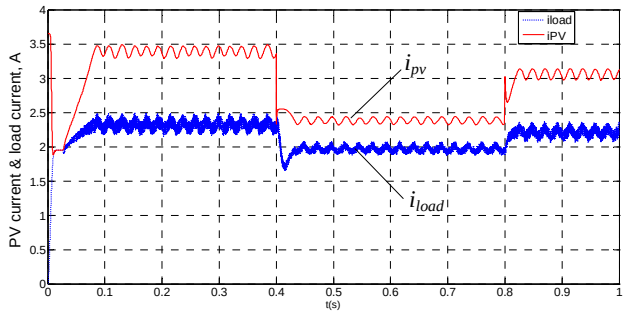

Fig. 4. Load and PV panel current for P&O MPPT

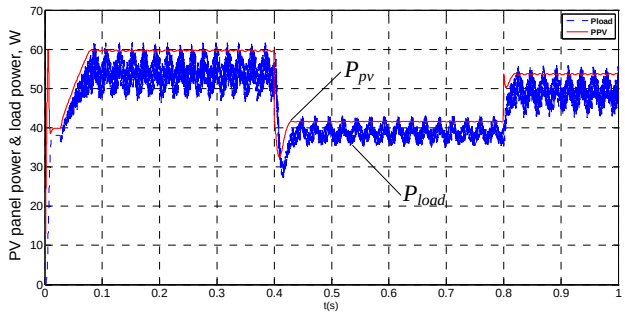

Fig. 5. Load and PV panel power for P&O MPPT

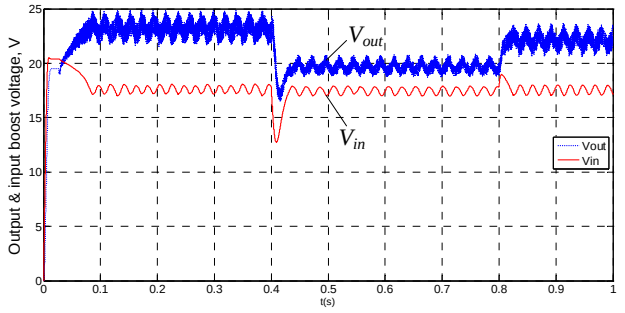

Fig. 6. Load and PV panel voltage for P&O MPPT

But in other side we observe that the output power follow the power generated by the PV panel, we keep the operating point on the MPP, which confirm the effectiveness of this method. The difference in power is due to the converter losses.

P&O technique is based on applying a disturbance to the voltage (positive or negative) to reach the maximum power point.

The problem with this technique is that the disturbance is fixed. In order to reach the point max quickly, we must apply a large disturbance, but this causes ripples, unlike that, if we apply a small perturbation, we will have a good precision but a very long response time.

Sliding mode MPPT. Sliding mode control is a nonlinear control type. It was originally introduced for the control of Variable Structure Systems (VSS).

In the control of the VSSs with sliding mode, the state trajectory is brought to a surface and then, by the switching law, it is obliged to remain in the vicinity of this sliding surface.

The sliding mode controller is based on the assumption of zero hysteresis on the sliding surface $S(x, t) = 0$, and thus on a variable switching frequency.

The idea is to divide the state space by a decision boundary called «sliding surface».

Stabilization on the sliding surface is achieved by switching at each crossing of the decision boundary [11-13]. When PV panel is operating in its maximum power, we can write

$$\frac{\partial P_{PV}}{\partial V_{PV}} = 0; \tag{9}$$

$$\frac{\partial P_{PV}}{\partial V_{PV}} = \left(\frac{\partial\left(V_{PV}\cdot I_{pv}\right)}{\partial V_{PV}}\right) = \left[\left(\frac{\partial I_{PV}}{\partial V_{PV}}\right)\cdot V_{PV} + I_{PV}\right]; \tag{10}$$

$$\frac{\partial P_{PV}}{\partial V_{PV}} = \frac{\partial I_{PV}}{\partial V_{PV}}\cdot V_{PV} + I_{PV}. \tag{11}$$

The switching surface adopted is the derivative of the power with respect to the voltage, and from equation (11) the sliding surface can be obtained by the following relation:

$$S = \frac{\partial P_{PV}}{\partial V_{PV}} = \frac{\partial I_{PV}}{\partial V_{PV}}\cdot V_{PV} + I_{PV}. \tag{12}$$

The switch control can be selected as:

$$u = \begin{cases} 0, & S > 0; \\ 1, & S < 0. \end{cases} \tag{13}$$

There are two operating zones separated by the MPP ($S(x) = 0$) as shown in Fig. 7, zone 1 for which the slope is positive ($S(x) > 0$), and zone 2 for which the slope is negative ($S(x) < 0$).

We can write also [14]:

$$u = \frac{1}{2}\left(1 - sign(S)\right). \tag{14}$$

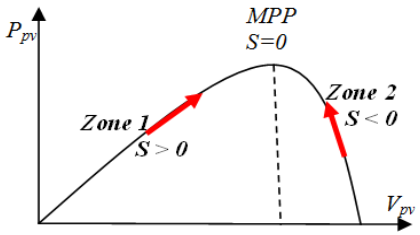

Fig. 7. Operating zones of PV system

Simulation of sliding mode MPPT. For the same conditions applied with P&O we obtain the following results. In Fig. 8–10 we observe amelioration of performances, with a ripple and disturbance less than the P&O technique.

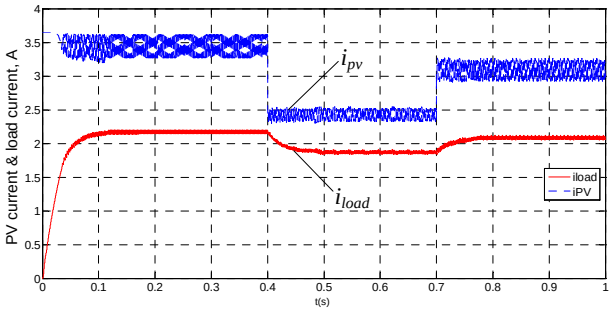

Fig. 8. Load and PV panel current for sliding mode MPPT

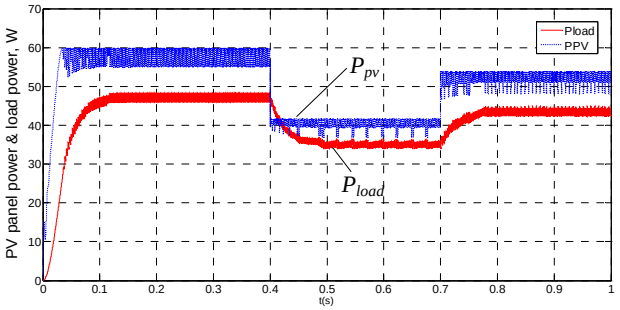

Fig. 9. Load and PV panel power for sliding mode MPPT

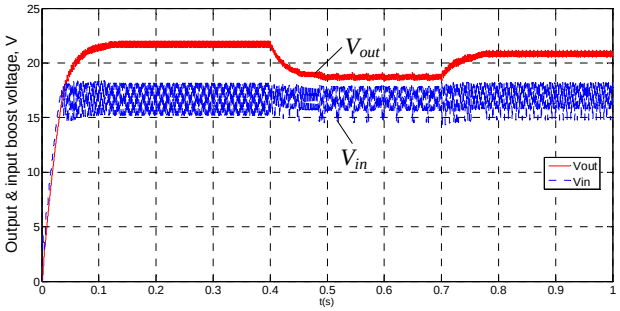

Fig. 10. Load and PV panel voltage for sliding mode MPPT

Ameliorate sliding mode MPPT. In sliding mode technique, the study is focused on the derivation of the power with respect to the voltage, thus it is appeared two zones depends on the sign of the sliding surface.

The ameliorate sliding mode is based on P&O principle, each switching control take into consideration the direction of the power variation (ΔP), and also the direction of the voltage variation (ΔV).

We can define four cases as shown in Fig. 11:

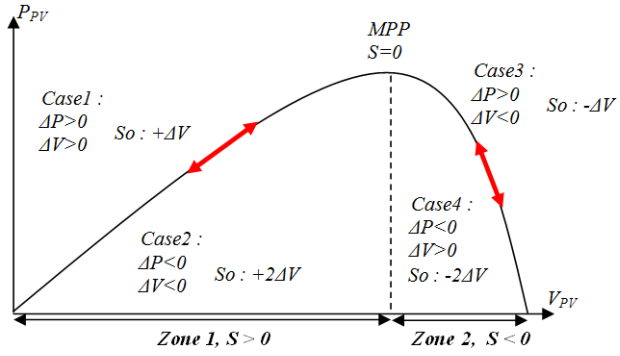

Fig. 11. The four situations of the operation point

Zone 1, case 1:

When operating point moves in zone 1, from point $(k-1)$ to (k) we notice that it approaches more the MPP, then, it should continue in the same direction.

$$V_{PV}(k+1) = V_{PV}(k) + \Delta V. \quad (15)$$

Zone 1, case 2:

When operating point always moves in zone 1, from the point $(k-1)$ to (k), we note that it moves away from the MPP. In this case, it must change direction; we apply a positive double step (disturbance)

$$V_{PV}(k+1) = V_{PV}(k) + 2\Delta V. \quad (16)$$

Zone 2, case 3:

When the operating point moves in zone 2, from the point $(k-1)$ to (k), we notice that it is closer to the MPP, so that it will continue in the same direction

$$V_{PV}(k+1) = V_{PV}(k) - \Delta V. \quad (17)$$

Zone 2, case 4:

When operating point always moves in zone 2, from the point $(k-1)$ to (k), we note that it moves away from the MPP, then, in this case we must change the direction; we apply a negative double step (disturbance)

$$V_{PV}(k+1) = V_{PV}(k) - 2\Delta V. \quad (18)$$

We conclude that the step of disturbance must be doubled when $\Delta P < 0$

$$P_{PV}(k) < P_{PV}(k-1), \quad (19)$$

where $V_{PV}(k)$, $P_{PV}(k)$ are, respectively, the voltage and the power of the PV panel, at the iteration (k); ΔV is the step of disturbance of the voltage; ΔP is the resulting power variation due to the voltage disturbance.

Simulation of ameliorate sliding mode MPPT. For the same conditions applied with P&O we obtain the following results (Fig. 12–14).

This technique is simple and easily realized, because it is based on classic P&O MPPT. By using the ameliorate sliding mode, the clear optimization of the performances but it needs more calculation time because of the existence of four cases, which means more precision but more iterations.

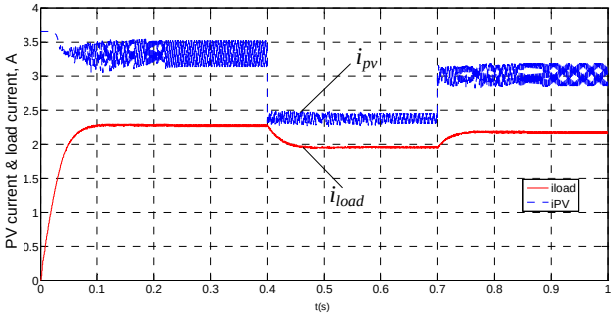

Fig. 12. Load and PV panel current for ameliorate sliding mode MPPT

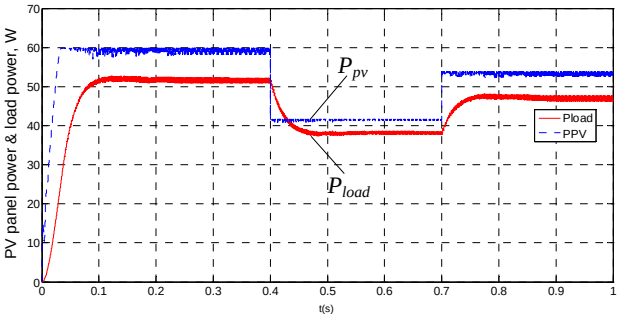

Fig. 13. Load and PV panel power for ameliorate sliding mode MPPT

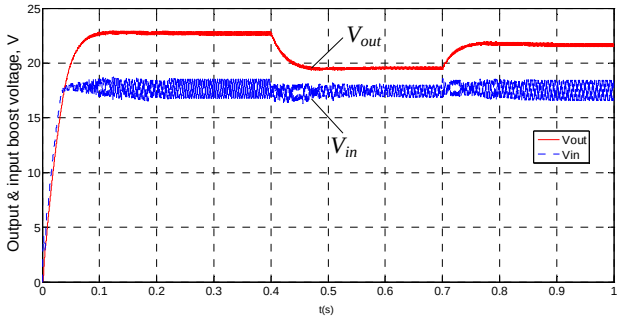

Fig. 14. Load and PV panel voltage for ameliorate sliding mode MPPT

Fuzzy logic MPPT. The theory of fuzzy logic was developed in by Prof. Lotfi A. Zadeh. The text «Fuzzy Sets» appeared in 1965 in the review «Information and Control» [15].

The majority of the developed controllers use the simple diagram suggested by I. Mamdani for the single-input/single-output system [16-18]. This diagram is shown in Fig. 15 (where SE, SCE – inputs gains; SdD – output gain).

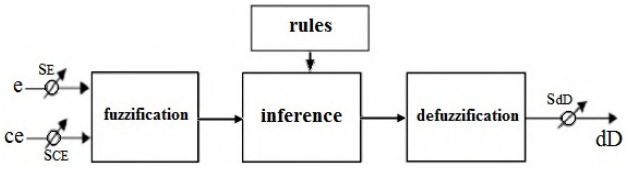

Fig. 15. General structure of a fuzzy controller

According to this diagram fuzzy system includes:

- the fuzzification corresponds to the process of determining the degree of member ship to each fuzzy partition;
- fuzzy rules (inference) indicate the use of the rules started by the various fuzzified input;
- defuzzification block corresponds to the transformation of outputs fuzzy values (linguistic form) to real values (ΔV).

These methods allow formulating a set of decisions in linguistic terms, using fuzzy sets to describe the error amplitudes, its variation and the appropriate control. By combining these rules, we can trace decision tables to give the values of controller output corresponding to situations of interest [19, 20].

The scale factors should be selected based on the study of the system such that, when the small transitory phenomenon, the permissible range for the error and its variation are not exceeded.

Description of the fuzzy system.

Error E. The error E is defined as the error between dP/dV and the seeking values $dP/dV = 0$. The latter value corresponds to the unique extreme value of the curve $P(V)$. This extreme point is a maximum. More E is positive; more the value of P increase .Conversely, more E is negative, more the value of P decreases. Finally when E tends to 0, the value of P tends towards its maximum, the MPP.

Variation of the error ΔE. The change in the error ΔE indicates in which direction and in what proportion the error changes in proportion as the algorithm is running. So when ΔE tends to 0, the system stabilizes (but not necessarily MPP).

Output criteria (disturbance). The disturbance or increment corresponds to the adjustment value added to the voltage in each iteration of the algorithm. The fuzzy rules allow determining and connecting the output of the controller to input signals by linguistic terms taking into account the experience acquired by a human operator.

Rules table. After having done some tests by varying the number of output classes and rules allocation, we get the following rules table [10] (Table 1).

Table 1

Fuzzy rules

ΔE \ E	NG	NM	NP	Z	PP	PM	PG
NG	NG	NG	NG	NG	NM	NP	Z
NM	NG	NG	NG	NM	NP	Z	PP
NP	NG	NG	NM	NP	Z	PP	PM
Z	NG	NM	NP	Z	PP	PM	PG
PP	NM	NP	Z	PP	PM	PG	PG
PM	NP	Z	PP	PM	PG	PG	PG
PG	Z	PP	PM	PG	PG	PG	PG

Simulation of fuzzy MPPT. For the same conditions applied with P&O we obtain the following results (Fig. 17–19).

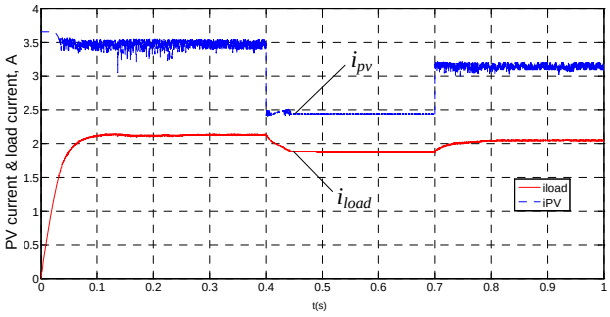

Fig. 17. Load current and PV current for fuzzy MPPT

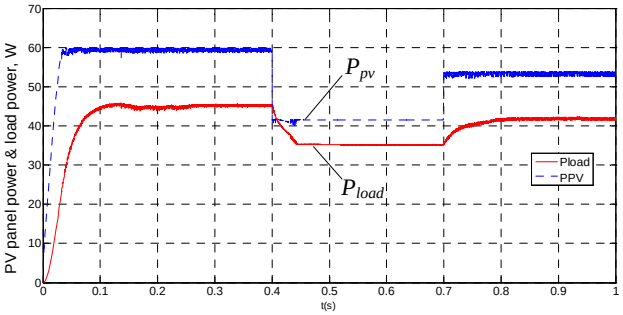

Fig. 18. Load power and PV power for fuzzy MPPT

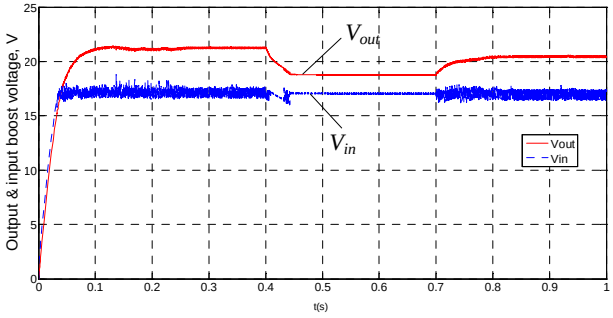

Fig. 19. Load voltage and PV voltage for fuzzy MPPT

We observe the amelioration in the evolutions of the various curves comparing to the classic P&O MPPT and also comparing to the other techniques. Very low fluctuation in voltage, in power or in current evolution, this confirms the effectiveness and the superiority of the fuzzy system applied.

The advantage of this technique is that the step of disturbance is adapted by the fuzzy system according to the variation of inputs, thus a transient period is shorter

without any overshooting compared to sliding mode MPPT and the ameliorated sliding mode MPPT.

Conclusions.

In order to supply an isolated site using photovoltaic system, it is very easy to connect directly the load to the supplying system. In this situation the photovoltaic panels are often oversized to ensure a sufficient power to provide the load; this led to an excessively expensive system.

The operation point system is obtained by the intersection between the curve of current depending to the voltage and the load curve.

It is necessary to integrate a power point tracking system, which has a role of detecting this point, and forces the system to works precisely on it via an electrostatic converter. For this aim a boost converter is used; its role is the adaptation of the supplying power and the augmentation of the output voltage.

As a comparative study, the converter is controlled by two techniques, sliding mode and fuzzy maximum power point tracking.

In the first part a classic perturb and observe method is treated and simulated in order to validate the studied model.

In sliding-mode method we define the sliding surface which is based on a hysteresis method, using the slope of the derivative of the power with respect to the voltage in order to reach the maximum power point. This method presents the advantage that it is independent on the system parameters. The simulation result shows the remarkable amelioration compared to the classic perturb and observe. The oscillations on the power response are the major disadvantage of this method.

The tracking behavior shows that Fuzzy maximum power point tracking system successfully and perfectly tracked the maximum power point with better performance than sliding-mode technique.

This controller guarantees high dynamic system performances, and eliminate the ripples in the power, the current and the voltage responses.

Conflict of interests. The authors declare no conflicts of interest.

REFERENCES

1. Weidong Xiao, Dunford W.G. A modified adaptive hill climbing MPPT method for photovoltaic power systems. *2004 IEEE 35th Annual Power Electronics Specialists Conference* (IEEE Cat. No.04CH37551), Aachen, Germany, 2004, vol. 3, pp. 1957-1963. doi: https://doi.org/10.1109/pesc.2004.1355417.

2. Ben Salah C., Ouali M. Comparison of fuzzy logic and neural network in maximum power point tracker for PV systems. *Electric Power Systems Research*, 2011, vol. 81, no. 1, pp. 43-50. doi: https://doi.org/10.1016/j.epsr.2010.07.005.

3. Guldemir H. Sliding Mode Control of Dc-Dc Boost Converter. *Journal of Applied Sciences*, 2005, vol. 5, no. 3, pp. 588-592. doi: https://doi.org/10.3923/jas.2005.588.592.

4. Komurcugil H. Adaptive terminal sliding-mode control strategy for DC–DC buck converters. *ISA Transactions*, 2012, vol. 51, no. 6, pp. 673-681. doi: https://doi.org/10.1016/j.isatra.2012.07.005.

5. Bianconi E., Calvente J., Giral R., Mamarelis E., Petrone G., Ramos-Paja C.A., Spagnuolo G., Vitelli M. Perturb and Observe MPPT algorithm with a current controller based on the sliding mode. *International Journal of Electrical Power & Energy Systems*, 2013, vol. 44, no. 1, pp. 346-356. doi: https://doi.org/10.1016/j.ijepes.2012.07.046.

6. Chu C.-C., Chen C.-L. Robust maximum power point tracking method for photovoltaic cells: A sliding mode control approach. *Solar Energy*, 2009, vol. 83, no. 8, pp. 1370-1378. doi: https://doi.org/10.1016/j.solener.2009.03.005.

7. Meekhun D., Boitier V., Dilhac J., Blin G. An automated and economic system for measuring of the current-voltage characteristics of photovoltaic cells and modules. *2008 IEEE International Conference on Sustainable Energy Technologies*, Singapore, 2008, pp. 144-148. doi: https://doi.org/10.1109/icset.2008.4746989.

8. Sholapur S., Mohan K.R., Narsimhegowda T.R. Boost Converter Topology for PV System with Perturb And Observe MPPT Algorithm. *IOSR Journal of Electrical and Electronics Engineering*, 2014, vol. 9, no. 4, pp. 50-56. doi: https://doi.org/10.9790/1676-09425056.

9. Youssef E.B., Stephane P., Bruno E., Corinne A. New P&O MPPT algorithm for FPGA implementation. *IECON 2010 - 36th Annual Conference on IEEE Industrial Electronics Society*, Glendale, AZ, 2010, pp. 2868-2873. doi: https://doi.org/10.1109/iecon.2010.5675079.

10. Nebti K., Debbabi F. Amelioration of MPPT P&O Using Fuzzy-Logic Technique for PV Pumping. *Renewable Energy for Smart and Sustainable Cities. ICAIRES 2018. Lecture Notes in Networks and Systems*, 2019, vol. 62. Springer, Cham. doi: https://doi.org/10.1007/978-3-030-04789-4_43.

11. Ghazanfari J., Farsangi M.M. Maximum power point tracking using sliding mode control for photovoltaic array. *Iranian Journal of Electrical and Electronic Engineering*, 2013, vol. 9, no. 3, pp. 189-196. Available at: http://ijeee.iust.ac.ir/article-1-523-en.pdf. (accessed on 20 May 2020).

12. Chatrenour N., Razmi H., Doagou-Mojarrad H. Improved double integral sliding mode MPPT controller based parameter estimation for a stand-alone photovoltaic system. *Energy Conversion and Management*, 2017, vol. 139, pp. 97-109. doi: https://doi.org/10.1016/j.enconman.2017.02.055.

13. Vázquez N., Azaf Y., Cervantes I., Vázquez E., Hernández C. Maximum power point tracking based on sliding mode control. *International Journal of Photoenergy*, 2015, vol. 2015, pp. 1-8. doi: https://doi.org/10.1155/2015/380684.

14. Farhat M., Barambones O., Ramos J.A., Gonzalez de Durana J.M. Maximum power point tracking controller based on sliding mode approach. *Conference Actas de las XXXV Jornadas de Automática*, 3-5 September, 2014, Valencia. Available at: http://www.ja2014.upv.es/wp-content/uploads/papers/paper_7.pdf (accessed on 15 June 2020).

15. Wu X., Shen J., Li Y., Lee K.Y. Fuzzy modeling and stable model predictive tracking control of large-scale power plants. *Journal of Process Control*, 2014, vol. 24, no. 10, pp. 1609-1626. doi: https://doi.org/10.1016/j.jprocont.2014.08.007.

16. Lacrose V., Titli A. Fusion and hierarchy can help fuzzy logic controller designers. *Proceedings of the Sixth IEEE International Conference on Fuzzy Systems*, Barcelona, Spain, 1997. doi: https://doi.org/10.1109/fuzzy.1997.616335.

17. Chouder A, Guijoan F, Silvestre S. Simulation of fuzzy-based MPP tracker and performance comparison with perturb & observe method. *Revue des Energies Renouvelables*. 2008, vol. 11, no. 4, pp.

577-586. Available at: https://www.asjp.cerist.dz/en/article/119627 (accessed on 25 July 2020).
18. Azzouzi M. Comparison between MPPT P&O and MPPT fuzzy controls in optimizing the photovoltaic generator. *International Journal of Advanced Computer Science and Applications (IJACSA)*, 2012, vol. 3, no. 12, pp 57-62. doi: https://doi.org/10.14569/ijacsa.2012.031208.
19. Zhang C., Zhao D. MPPT with asymmetric fuzzy control for photovoltaic system. *2009 4th IEEE Conference on Industrial Electronics and Applications*, Xi'an, 2009, pp. 2180-2183. doi: https://doi.org/10.1109/iciea.2009.5138584.
20. Noman A.M., Addoweesh K.E., Mashaly H.M. DSPACE Real-Time Implementation of MPPT-Based FLC Method. *International Journal of Photoenergy*, 2013, vol. 2013, pp. 1-11. doi: https://doi.org/10.1155/2013/549273.

Received 08.11.2020
Accepted 11.12.2020
Published 25.02.2021

Khalil Nebti[1], *Doctor of Electrotechnical,*
Ryma Lebied [2], *Ph.D.,*
[1] Electrical Engineering Laboratory of Constantine, LEC,
Department of Electrical Engineering,
University of Constantine 1, 25000 Constantine, Algeria.
e-mail: idor2003@yahoo.fr
[2] Electrotechnical Laboratory Skikda (LES),
Department of Electrical Engineering,
University 20 August 1955,
26 Road El Hadaiek 21000, Skikda, Algeria,
e-mail: r.lebied@univ-skikda.dz

How to cite this article:
Nebti K., Lebied R. Fuzzy maximum power point tracking compared to sliding mode technique for photovoltaic systems based on DC-DC boost converter. *Electrical Engineering & Electromechanics*, 2021, no. 1, pp. 67-73. **doi: 10.20998/2074-272X.2021.1.10.**

Матеріали приймаються за адресою:
Кафедра "Електричні апарати", НТУ "ХПИ", вул. Кирпичова, 21, м. Харків, 61002, Україна
Електронні варіанти матеріалів по e-mail: a.m.grechko@gmail.com

Довідки за телефонами: +38 050 653 49 82 Клименко Борис Володимирович
+38 067 359 46 96 Гречко Олександр Михайлович

Передплатний індекс: 01216